

FUNCTIONAL COMPLEX PLASMONICS
UNDERSTANDING AND REALIZING
CHIRAL AND ACTIVE PLASMONIC SYSTEMS

Von der Fakultät Mathematik und Physik
der Universität Stuttgart zur Erlangung der Würde
eines Doktors der Naturwissenschaften (Dr. rer. nat.)
genehmigte Abhandlung

vorgelegt von

Xinghui Yin

aus Harbin

Hauptberichter: Prof. Dr. Harald Giessen
Mitberichter: Prof. Dr. Thomas Zentgraf
Tag der Einreichung: 23.08.2016
Tag der mündlichen Prüfung: 26.09.2016

4. Physikalisches Institut der Universität Stuttgart

2016

Xinghui Yin: *Functional Complex Plasmonics Understanding and Realizing Chiral and Active Plasmonic Systems*, 2016

To my parents.

How would you like to live in Looking-Glass house, Kitty?
I wonder if they'd give you milk in there?
Perhaps Looking-Glass milk isn't good to drink -

— *Lewis Carroll, 'Through the Looking Glass', 1871*

Eine Theorie hat nur die Alternative des Seins recht oder falsch.
Ein Modell hat eine dritte Möglichkeit:
Es kann recht, aber irrelevant sein.

— *Manfred Eigen, 1973*

ABSTRACT

The present thesis concerns itself with the theoretical study and experimental realization of complex plasmonic systems for highly integrated nanophotonic devices and enhanced chiroptical spectroscopy. In particular, the two broad topics of *active metasurfaces* and *chiral plasmonic systems* are investigated to this end.

In this context, the chalcogenide phase change material GeSbTe is utilized to demonstrate, for the first time, metasurface based beam steering and varifocal lensing devices.

The versatility of this approach to lending active functionality to plasmonic systems is further evidenced through our realization of a chiral plasmonic system that both exhibits a wavelength tunable and handedness switchable chiroptical response.

Furthermore, in order to enable a systematic study of plasmon-enhanced chiroptical spectroscopy, we first establish and analyze canonical chiral plasmonic building blocks, in particular, the loop-wire and chiral dimer structure. The results from this undertaking lead to fundamental insights for understanding complex chiral plasmonic systems.

Finally, we implement chiral media in the commercial electromagnetic full-field solver Comsol Multiphysics to carry out rigorous numerical studies of the macroscopic electrodynamic processes involved in plasmon-enhanced circular dichroism spectroscopy revealing both substantial enhancement due to near-field effects as well as upper boundaries to the magnitude of such enhancements.

ZUSAMMENFASSUNG

Die vorliegende Arbeit beschäftigt sich mit dem theoretischen Studium und der experimentellen Realisierung von komplexen plasmonischen Systemen für die Nutzung in hochintegrierten nanophotonischen Bauteilen und in der verstärkten chiraloptischen Spektroskopie.

Insbesondere, wendet sie sich den zwei großen Themen der *aktiven Metaoberflächen* und der *chiralen Plasmonik* zu.

In diesem Zusammenhang wird das chalcogenide Phasenwechselmaterial GeSbTe eingesetzt, um zum ersten Mal eine Metaoberflächenbasierte Strahlsteuerung und varifokale Fokussierung zu erzeugen.

Die Vielseitigkeit dieser Methode, plasmonischen Systemen aktive Funktionalität zu verleihen, wird weiterhin durch die Realisierung eines chiralen plasmonischen Systems erwiesen, das sowohl Wellenlängen abstimmbare sowie Händigkeit schaltbare chiraloptische Antwort aufweist.

Weiterhin begründen und analysieren wir die kanonischen chiralen Basiskomponenten, wie die Draht-Schlaufen-Struktur und das chirale Dimer, um das systematische Studium von Plasmonen-verstärkter chiraloptischer Spektroskopie zu unterstützen. In diesem Zuge ist es uns gelungen, wichtige Einsichten zur Generierung von plasmonischer Chiralität zu gewinnen und somit auch komplexe chirale plasmonische Systeme zu erklären.

Schließlich implementieren wir chirale Medien im kommerziell verfügbaren elektromagnetischen Feldsimulator Comsol Multiphysics, um gründliche Untersuchungen der makroskopischen elektrodynamischen Prozesse durchzuführen, die in Plasmonen-verstärkter chiraloptischer Spektroskopie zu tragen kommen. Hierbei weisen wir einerseits die wichtige Rolle der Nahfeldverstärkung nach und setzen andererseits gleichzeitig ein theoretisches Limit für die zu erwartende Größe der Verstärkung.

SCIENTIFIC CONTRIBUTIONS

ARTICLES IN PEER-REVIEWED SCIENTIFIC JOURNALS

Articles within the scope of this thesis:

- [A1] B. Frank, **X. Yin**, M. Schäferling, J. Zhao, S. M. Hein, P. V. Braun, and H. Giessen: *Large-area 3D chiral plasmonic structures*. ACS Nano **7**, 6321–6329 (2013).
DOI 10.1021/nn402370x, cit. on p. 3.
- [A2] **X. Yin**, M. Schäferling, B. Metzger, and H. Giessen: *Interpreting Chiral Nanophotonic Spectra: The Plasmonic Born-Kuhn Model*. Nano Lett. **13**, 6238–6243 (2013).
DOI 10.1021/nl403705k, cit. on pp. 3, 110, 111, 117, 134.
- [A3] **X. Yin**, M. Schäferling, A.-K. U. Michel, A. Tittl, M. Wuttig, T. Taubner, and H. Giessen: *Active Chiral Plasmonics*. Nano Lett. **15**, 4255–4260 (2015).
DOI 10.1021/nl5042325, cit. on pp. 3, 38.
- [A4] M. L. Nesterov*, **X. Yin***, M. Schäferling, H. Giessen, and T. Weiss: *The Role of Plasmon-Generated Near Fields for Enhanced Circular Dichroism Spectroscopy*. ACS Photonics **3**, 578–583 (2016).
*These authors have contributed equally.
DOI 10.1021/acsp Photonics.5b00637, cit. on p. 3.
- [A5] M. Schäferling, **X. Yin**, and H. Giessen: *Formation of chiral fields in a symmetric environment*. Opt. Express **20**, 26326–26336 (2012).
DOI 10.1364/OE.20.026326, cit. on pp. 56, 126, 149.
- [A6] M. Schäferling, **X. Yin**, N. Engheta, and H. Giessen: *Helical Plasmonic Nanostructures as Prototypical Chiral Near-Field Sources*. ACS Photonics **1**, 530–537 (2014).
This article has been highlighted on the cover.
DOI 10.1021/ph5000743, cit. on p. 126.

- [A7] I. Sakellari, **X. Yin**, M. Nesterov, K. T. Aggelos Xomalis, M. Farsari, and H. Giessen: *The Omega Structure as Plasmonic Realization of the Condon Theory* (2016). in preparation.
- [A8] **X. Yin**, T. Steinle, L. Huang, M. Wuttig, T. Taubner, T. Zentgraf, and H. Giessen: *Realizing Beam Steering and Varifocal Zoom Lensing using Active Plasmonic Metasurfaces*. submitted (2016).

Further articles beyond the scope of this thesis:

- [O1] A. Tittl, A.-K. U. Michel, M. Schäferling, **X. Yin**, B. Gholipour, L. Cui, M. Wuttig, T. Taubner, F. Neubrech, and H. Giessen: *Switchable mid-infrared plasmonic perfect absorber with multispectral thermal imaging capability*. *Adv. Mater.* **27**, 4597–4603 (2015).
This article has been highlighted on the front inside cover.
DOI 10.1002/adma.201502023, cit. on p. 38.
- [O2] A. Tittl, M. G. Harats, R. Walter, **X. Yin**, M. Schäferling, N. Liu, R. Rapaport, and H. Giessen: *Quantitative Angle-Resolved Small-Spot Reflectance Measurements on Plasmonic Perfect Absorbers: Impedance Matching and Disorder Effects*. *ACS Nano* **8**, 10885–10892 (2014).
DOI 10.1021/nn504708t, cit. on p. 112.
- [O3] T. Steinle, F. Neubrech, A. Steinmann, **X. Yin**, and H. Giessen: *Mid-infrared Fourier-transform spectroscopy with a high-brilliance tunable laser source: investigating sample areas down to 5 μm diameter*. *Optics Express* **23**, 11105–11113 (2015).
- [O4] D. E. Gómez, **X. Yin**, F. Neubrech, D. Dregely, K. Lindfors, T. Davis, and Giesse: *Microcavity plexcitons: Far-field Coupling of Plasmons and Excitons*. submitted (2014).
- [O5] J. M. Hoffmann, **X. Yin**, J. Richter, A. Hartung, T. W. W. Maß, and T. Taubner: *Low-Cost Infrared Resonant Structures for Surface-Enhanced Infrared Absorption Spectroscopy in the Fingerprint Region from 3 to 13 μm* . *The Journal of Physical Chemistry C* **117**, 11311–11316 (2013).

- [O6] A. Tittl, **X. Yin**, H. Giessen, X.-D. Tian, Z.-Q. Tian, C. Kremers, D. N. Chigrin, and N. Liu: *Plasmonic Smart Dust for Probing Local Chemical Reactions*. Nano Letters **13**, 1816–1821 (2013).
- [O7] J. Vogt, C. Huck, B. Frank, **X. Yin**, H. Giessen, A. Pucci, and F. Neubrech: *Surface-Enhanced Infrared Spectroscopy Benefits From Monocrystalline Gold Antennas*. submitted (2016).

PATENTS

- [Pa1] **X. Yin** and H. Giessen: *Chiral Nanoplasmonic Switch* (2015). pending.
- [Pa2] **X. Yin** and H. Giessen: *Multi-Functional Metasurfaces* (2016). pending.

CONTRIBUTIONS TO INTERNATIONAL CONFERENCES AND WORKSHOPS

Contributed talks (presenting author):

- [T1] **X. Yin** and H. Giessen: *Chiraloptische Spektroskopie im Nanofokus*, Zeiss Stipendiatentreffen, 2013.
- [T2] **X. Yin**, A.-K. U. Michel, M. Schäferling, A. Tittl, T. Taubner, and H. Giessen: *Chiral Plasmonic Fano Resonance*, DPG Frühjahrstagung der Sektion Kondensierte Materie (SKM), Dresden (Germany), 2014.
- [T3] **X. Yin**, M. Schäferling, S. M. Hein, and H. Giessen: *Plasmonic Analog of the Born-Kuhn Model*, 4th International Topical Meeting on Nanophotonics and Metamaterials (Nanometa), Seefeld (Austria), 2013.
- [T4] **X. Yin**, M. Schäferling, A.-K. U. Michel, A. Tittl, M. Wuttig, T. Taubner, and H. Giessen: *Active mid-IR plasmonic metasurfaces: Tunable and switchable chirality and flat-surface beam steering*, DPG Frühjahrstagung der Sektion Kondensierte Materie (SKM), Berlin (Germany), 2015.

- [T5] **X. Yin**, A. Tittl, A.-K. U. Michel, M. Wuttig, T. Taubner, and H. Giessen: *Active mid-IR metadevices*, IHT Kolloquium, 2015.
- [T6] **X. Yin**, A. Tittl, M. Schäferling, A.-K. U. Michel, B. Gholipour, L. Cui, M. Wuttig, T. Taubner, F. Neubrech, and H. Giessen: *Active mid-infrared plasmonic metadevices*, 5th International Topical Meeting on Nanophotonics and Metamaterials (Nanometa), Seefeld (Austria), 2015.
- [T7] **X. Yin**, A. Tittl, M. Schäferling, A.-K. U. Michel, M. Wuttig, F. Neubrech, T. Taubner, and H. Giessen: *Active mid-IR plasmonic metadevices*, 6th International Conference on Metamaterials, Photonic Crystals and Plasmonics (META), New York (USA), 2015.

Poster contributions (presenting author):

- [P1] M. Mesch, B. Frank, M. Hentschel, M. Schäferling, **X. Yin**, C. Zhang, P. V. Braun, and H. Giessen: *Non-invasive Glucose Sensing*, Forschungstag BW Stiftung, Stuttgart (Germany), 2013.
- [P2] **X. Yin** and H. Giessen: *Active Chiral Plasmonics*, Zeiss Stipendiatentreffen, 2014.
- [P3] **X. Yin**, M. Schäferling, and H. Giessen: *Chiral Plasmonic Realization of the Born-Kuhn Model*, 6th International Conference on Surface Plasmon Photonics (SPP), Ottawa (Canada), 2013.
- [P4] **X. Yin**, M. Schäferling, A.-K. U. Michel, A. Tittl, M. Wuttig, T. Taubner, and H. Giessen: *Tunable and Switchable Mid-IR Chiral Metamaterial*. Poster, Chirality, Prague (Czech Republic), 2014.
- [P5] **X. Yin**, M. Schäferling, A.-K. U. Michel, A. Tittl, M. Wuttig, T. Taubner, and H. Giessen: *Tunable and Switchable Mid-IR Chiral Metamaterial*, Gordon Research Conference on Plasmonics, Newry (USA), 2014.

Contributions as co-author:

- [C1] F. Neubrech, T. Steinle, A. Steinmann, **X. Yin**, and H. W. Giessen: *High-Brilliance Mid-Infrared Femtosecond Light Source for Surface-Enhanced Infrared Spectroscopy*. talk, CLEO: QELS_Fundamental Science, Optical Society of America, 2015.
- [C2] B. Frank, **X. Yin**, M. Schäferling, J. Zhao, S. M. Hein, and H. Giessen: *Large-area 3D chiral plasmonic nanostructures fabricated by colloidal hole mask nanolithography*. Talk, DPG Frühjahrstagung der Sektion Kondensierte Materie (SKM), Regensburg (Germany), 2013.
- [C3] B. Frank, **X. Yin**, M. Schäferling, J. Zhao, S. M. Hein, P. V. Braun, and H. Giessen: *Large-area 3D chiral plasmonic structures*. Poster, Advanced Study Institute NATO Nanomaterials and Nanoarchitectures, Cork (Ireland), 2013.
- [C4] B. Frank, J. Zhao, M. Schäferling, **X. Yin**, S. M. Hein, and H. Giessen: *Low-cost large-area fabrication and chiral optical properties of 3D chiral plasmonic nanoantennas*. Poster, 12th International Conference on Near-field Optics and Related Techniques (NFO), San Sebastian (Spain), 2012.
- [C5] M. L. Nesterov, T. Weiss, J. Chin, **X. Yin**, M. Schäferling, B. Metzger, and H. Giessen: *Symmetry-breaking plasmonics: chirality, nonreciprocity, nonlinearity and tunability*. poster, Humboldt Networking Meeting, 2014.
- [C6] M. Nesterov, **X. Yin**, M. Schäferling, T. Weiss, and H. Giessen: *Plasmonic chirality and chiral sensing: effects and limitations*. Talk, DPG Frühjahrstagung der Sektion Kondensierte Materie (SKM), Berlin (Germany), 2015.
- [C7] M. Nesterov, **X. Yin**, M. Schäferling, T. Weiss, and H. Giessen: *Rigorous Numerical Analysis of Plasmonically Enhanced Chiroptical Spectroscopy*. Talk, Conference on Lasers and Electro-Optics (CLEO), München (Germany), 2015.

- [C8] R. Semenyshyn, M. Neubrech F and Hentschel, J. Yin X and Vogt, C. Huck, F. W. and C Stanglmair and C Pacholski, and H. Giessen: *Surface-Enhanced Infrared Spectroscopy for Poly-Peptide Sensing on single Nanostructures*. talk, DPG Frühjahrstagung der Sektion Kondensierte Materie (SKM), 2016.
- [C9] X. R Semenyshyn and Neubrech F and Yin, F. Weiher, C. Stanglmair, C. Pacholski, and H. Giessen: *Poly-Peptide Sensing with nanoantenna-assisted Surface-Enhanced Infrared Spectroscopy*. talk, DPG Frühjahrstagung der Sektion Kondensierte Materie (SKM), 2015.
- [C10] M. Schäferling, D. Dregely, M. Hentschel, **X. Yin**, J. Dorfmueller, and H. Giessen: *Local enhancement of optical chirality in plasmonic nanostructures*. Poster, 12th International Conference on Near-field Optics and Related Techniques (NFO), San Sebastian (Spain), 2012.
- [C11] M. Schäferling, M. Hentschel, D. Dregely, **X. Yin**, and H. Giessen: *Design of Plasmonic Nanostructures for Chiral Sensing*. Talk, Fifth International Workshop on Theoretical and Computational Nano-Photonics (TaCoNa), Bad Honnef (Germany), 2012.
- [C12] M. Schäferling, **X. Yin**, N. Engheta, and H. Giessen: *Helical Plasmonic Nanostructures as Prototypical Chiral Near-Field Sources*. Talk, 8th International Congress on Advanced Electromagnetic Materials in Microwaves and Optics (Metamaterials), Copenhagen (Denmark), 2014.
- [C13] M. Schäferling, **X. Yin**, N. Engheta, and H. Giessen: *Helical Plasmonic Nanostructures as Prototypical Chiral Near-Field Sources*. poster, Chirality, Prague (Czech Republic), 2014.
- [C14] M. Schäferling, **X. Yin**, N. Engheta, and H. Giessen: *Helical Plasmonic Nanostructures for Strong Chiral Near-Fields*. Talk, DPG Frühjahrstagung der Sektion Kondensierte Materie (SKM), Dresden (Germany), 2014.
- [C15] M. Schäferling, **X. Yin**, and H. Giessen: *Chiral Fields in Achiral Systems: Towards Enantiomer Sensing with Linearly Polarized Light*. Talk, 14th International Conference on Chiroptical Spectroscopy, Nashville (USA), 2013.

- [C16] M. Schäferling, **X. Yin**, and H. Giessen: *Chiral Fields in Achiral Systems: Towards Enantiomer Sensing with Linearly Polarized Light*. Talk, 6th International Conference on Surface Plasmon Photonics (SPP), Ottawa (Canada), 2013.
- [C17] M. Schäferling, **X. Yin**, and H. Giessen: *Symmetric Structures Produce Chiral Near Fields: Towards Enantiomer Sensing with Linearly Polarized Light*. poster, 4th International Topical Meeting on Nanophotonics and Metamaterials (Nanometa), Seefeld (Austria), 2013.
- [C18] M. Schäferling, **X. Yin**, and H. Giessen: *Chiral Fields in Achiral Systems*. Talk, 9th Workshop on Numerical Methods for Optical Nano Structures, Zurich (Switzerland), 2013.
- [C19] M. Schäferling, **X. Yin**, and H. Giessen: *Chiral Fields in Achiral Systems*. Talk, DPG Frühjahrstagung der Sektion Kondensierte Materie (SKM), Regensburg (Germany), 2013.
- [C20] M. Schäferling, **X. Yin**, M. L. Nesterov, H. Giessen, and T. Weiss: *Enantiomorphic chiral near-fields in locally chiral plasmonic lattices*. Talk, DPG Frühjahrstagung der Sektion Kondensierte Materie (SKM), Regensburg (Germany), 2016.
- [C21] T. Weiss, M. Nesterov, **X. Yin**, M. Schäferling, and H. Giessen: *Rigorous numerical analysis of plasmonically enhanced chiroptical response*. Poster, 5th International Topical Meeting on Nanophotonics and Metamaterials (Nanometa), Seefeld (Austria), 2015.

CONTENTS

1	INTRODUCTION	1
2	GENERAL THEORETICAL BACKGROUND	5
2.1	Macroscopic Electrodynamics	5
2.1.1	Constitutive Equations	6
2.1.2	Linear Isotropic Media	7
2.1.3	Kramers-Kronig Relations	8
2.1.4	Wave Propagation in Linear Isotropic Media	9
2.1.5	Electromagnetic (EM) Waves at Interfaces	10
2.2	Plasmonics	12
2.2.1	Optical Properties of Metals	12
2.2.2	Surface Plasmons and Grating Modes	17
2.2.3	Optical Antennas	19
2.2.4	Plasmon Hybridization	24
2.3	Phase Change Materials	27
2.4	General Methods	29
2.4.1	Experimental Methods	29
2.4.2	Simulation Methods	31
i	ACTIVE METASURFACES	35
3	ACTIVE NANOPHOTONIC COMPONENTS	37
3.1	Beam-Steering	40
3.2	Varifocal Lensing	47
ii	CHIRAL PLASMONICS	53
4	A BRIEF ACCOUNT OF OPTICAL ACTIVITY AND CHIRALITY	55
5	CHIRAL THEORETICAL BACKGROUND	59
5.1	Chiroptical Spectroscopy	59
5.1.1	Rotational Strength in Circular Dichroism	65
5.1.2	Chiral Plasmonic Split-Ring Resonator	66
5.2	Chiral Electrodynamics	67
5.2.1	Constitutive Equations for Chiral Media	67
5.2.2	Wave Propagation in Chiral Media	68

6	ELECTRON THEORIES OF CHIRALITY AND THEIR PLASMONIC ANALOGS	69
6.1	The Omega Structure as Plasmonic Analog of the Condon Model	71
6.2	The Chiral Dimer as Plasmonic Analog of the Born-Kuhn Model	79
6.2.1	The Born-Kuhn Oscillator Model	81
6.2.2	The Hybridization View for the Plasmonic Case	84
6.3	Spiral-Ramp Structures re-interpreted	95
6.3.1	Understanding the Chiral Mode Structure . .	102
7	ACTIVE CHIRAL PLASMONICS	109
7.1	Tunable Chirality	110
7.2	Switchable Chirality	115
8	STUDYING ENHANCED CHIROPTICAL SPECTROSCOPY	121
8.1	Implementation of Chiral Media in COMSOL	122
8.1.1	Transmission through a Bi-isotropic Slab . . .	122
8.1.2	Metal-Core Chiral-Shell Particle	125
8.2	Rigorous Numerical Study of Plasmon-Enhanced CD	126
8.2.1	Standard PECD Setup with Nanorods	129
8.2.2	Gap Antenna Enhancement Factors	132
8.2.3	Chiral Dimer Enhancement Factors	134
8.2.4	The Role of Field Vector Alignment	135
9	CONCLUSION AND OUTLOOK	139
A	DETAILS OF THE NUMERICAL STUDY OF HYBRID PLASMON-CHIRAL MEDIA SYSTEMS	145
A.O.1	Determining realistic Simulation Parameters .	145
A.O.2	Baseline Corrected CD-Enhancement Factors	146
A.1	Loss Decomposition	148
	BIBLIOGRAPHY	153

CONSTANTS

c	speed of light in vacuum, $c = 299\,792\,458\text{ m s}^{-1}$
e	elementary charge, $e = 1.602 \times 10^{-19}\text{ C}$
ϵ_0	vacuum permittivity, $\epsilon_0 = 8.854 \times 10^{-12}\text{ F m}^{-1}$
μ_0	vacuum permeability, $\mu_0 = 4\pi \times 10^{-7}\text{ N A}^{-2}$

SYMBOLS

A	absorbance
α	electric dipole polarizability
B	magnetic field
χ	magnetic dipole polarizability
C	optical chirality (see Eq. (A.4))
D	electric displacement field
D	propagation distance
d	distance between oscillators in the Born-Kuhn model
E	electric field
ε	electric permittivity
γ	damping in oscillator models
Γ	chirality parameter of the Drude-Born-Fedorov chiral constitutive equations (see Eq. (6.3b))
H	magnetic field strength
J	Jones vector
j	free current
k	wave number
κ	chirality parameter of the standard chiral constitutive equations (see Eq. (5.12))
m	magnetic dipole moment
μ	magnetic permeability
N	number of particles described by a oscillator model
n	refractive index
ω	angular frequency
ω_0	resonance frequency
ω_p	plasma frequency (see Eq. (2.44))

\mathbf{P}	macroscopic polarization
\mathbf{p}	electric dipole moment
ϕ	phase
φ	polarization angle
R	reflectance
T	transmittance

Vectors are printed **bold**. A circumflex denotes quantities that have been normalized (e. g., $\hat{x} \equiv x/x_{\text{normto}}$). Differential responses are described by Δ . Partial differentiation with respect to the variable x is denoted by ∂_x . The real and imaginary part of a variable x are denoted $\Re(x)$ and $\Im(x)$, respectively.

ACRONYMS

ACS	absorption cross section
BI	bi-isotropic
CD	circular dichroism
CP	circularly polarized light
CPL	circularly polarized light
CST MWS	CST Microwave Studio
DLW	direct laser writing
DNA	desoxyribonucleic acid
EBL	electron beam lithography
ECS	extinction cross section
EELS	electron energy loss spectroscopy
EM	electromagnetic
FDTD	finite-difference frequency-domain
FEM	finite element method
FMM	fourier modal method
FTIR	Fourier transform infrared
FWHM	full width at half maximum
GST	Ge-Sb-Te
IMI	insulator-metal-insulator
IR	infrared
LCP	left-handed circularly polarized
LP	linearly polarized light
LSPR	localized surface plasmon polariton resonance
MCT	mercury cadmium telluride
MIR	mid-infrared
NIR	near infrared

OC	optical chirality
ORD	optical rotatory dispersion
PCM	phase-change material
PEC	perfect electric conductor
PECD	plasmon-enhanced circular dichroism
PML	perfectly matched layer
PMMA	poly(methyl methacrylate)
RCP	right-handed circularly polarized
RF	radio frequency
SEIRA	surface-enhanced infrared spectroscopy
SEM	scanning electron microscope
SERS	surface-enhanced Raman spectroscopy
SHG	second harmonic generation
SPP	surface plasmon polariton
SRR	split-ring resonator
THG	third harmonic generation
UV	ultraviolet
VCD	vibrational circular dichroism
VIS	visible

LIST OF FIGURES

Figure 2.1	Dielectric data for gold with Drude model fits.	14
Figure 2.2	Reflectivity R of an undamped free electron plasma.	16
Figure 2.3	Field amplitudes and field lines of surface plasmon polariton (SPP)s.	18
Figure 2.4	Dispersion relation for bulk and surface plasmons.	19
Figure 2.5	Optical and RF antennas.	20
Figure 2.6	Real and imaginary parts of the polarizability of a small metallic sphere.	21
Figure 2.7	Field enhancement at rod antenna.	23
Figure 2.8	Dimer Hybridization	26
Figure 2.9	Coupled mechanical oscillators.	27
Figure 2.10	Schematic of phase-change material (PCM) switching behavior.	28
Figure 2.11	Ge-Sb-Te (GST) alloys and GST-326 refractive index.	29
Figure 2.12	Single layer electron beam lithography.	30
Figure 2.13	Yee-Cell.	33
Figure 2.14	Different mesh geometries.	34
Figure 3.1	Active plasmonic metasurface for beam steering.	39
Figure 3.2	Working principle for active beam steering metasurface.	41
Figure 3.3	Experimental realization of beam steering metasurface.	43
Figure 3.4	Working principle of cylindrical varifocal zoom lens.	46
Figure 3.5	Experimental realization of the cylindrical varifocal lens.	48
Figure 3.6	Infrared camera images at different planes.	49
Figure 4.1	Enantiomorphs of tartaric acid crystals.	56

Figure 5.1	Chiroptical spectroscopy measurement methods.	62
Figure 5.2	Ellipticity.	63
Figure 5.3	Typical circular dichroism (CD) and optical rotatory dispersion (ORD) spectra.	64
Figure 5.4	Linear and circular currents involved in optically active transitions.	66
Figure 5.5	Linear and circular currents involved in optically active transitions.	67
Figure 6.1	Chiral plasmonic omega structure.	72
Figure 6.2	Schematic of fabrication of omega structures.	73
Figure 6.3	Omegas before plating I.	73
Figure 6.4	Omegas before plating II.	74
Figure 6.5	Omegas after plating.	75
Figure 6.6	Optical spectra of omegas from experiment and simulation.	76
Figure 6.7	Evaluation of cross-converted polarization from omega structures.	77
Figure 6.8	Born-Kuhn model and associated calculated CD and ORD spectra.	81
Figure 6.9	BINOL.	83
Figure 6.10	Chiral hybridization model.	85
Figure 6.11	Simulated and measured CD and ORD spectra for chiral dimer with 120 nm interparticle separation.	88
Figure 6.12	Time-reversal symmetry of chiral dimer.	89
Figure 6.13	Simulated and measured CD and ORD spectra for chiral dimer with 60 nm interparticle separation.	91
Figure 6.14	Analytic fits to measured ORD and CD spectra.	92
Figure 6.15	Hole-mask lithography and tilted angle rotation evaporation.	96
Figure 6.16	AFM image of spiral ramp structure.	98
Figure 6.17	Simulated and measured transmittance spectra of spiral ramp for linearly polarized light.	99
Figure 6.18	Simulated current distributions of spiral ramp structure.	101

Figure 6.19	Mechanism of mode formation for spiral ramp structure under circularly polarized light (CPL) illumination.	105
Figure 7.1	Tunable chirality concept.	111
Figure 7.2	Fabrication flow chart	112
Figure 7.3	Tunable chirality experiment and simulation.	113
Figure 7.4	Switchable chirality concept.	115
Figure 7.5	Switchable chirality: measurement and simulation	117
Figure 8.1	Transmission through a bi-isotropic slab in air.	123
Figure 8.2	Spherical gold nanoparticle surrounded by chiral shell	125
Figure 8.3	Schematic of plasmon-enhanced circular dichroism (PECD) detection scheme.	128
Figure 8.4	Optical responses of chiral medium patches located at the hot spots of a plasmonic rod-antenna array.	130
Figure 8.5	Gap antenna and rod antenna enhancement factors.	132
Figure 8.6	Chiral plasmonic dimers with chiral medium patches placed in their hot-spot region.	134
Figure 8.7	Enhancement factors for different dimer configurations (geometries are schematically shown on the left).	135
Figure 9.1	PCM enabled tunable plasmon peaks.	139
Figure 9.2	Various realized active plasmonic systems.	140
Figure 9.3	Various realized chiral plasmonic systems.	143
Figure 9.4	Plasmon-enhanced CD.	144
Figure A.1	Dispersion curves of chiral medium material parameters.	147
Figure A.2	Derivation of the baseline corrected CD signal enhancement factor.	150
Figure A.3	Loss Decomposition.	151

INTRODUCTION

Plasmonics is the commonly used portmanteau for the study of surface *plasmon* polariton *photonics* and relies on the two main effects that arise when light interacts with the free electrons of a metal: the surface plasmon polariton (SPP) and the localized surface plasmon polariton resonance (LSPR). Both are accompanied by enhanced electromagnetic (EM) fields in the vicinity of the metal surface and allow for the concentration of light into sub-wavelength volumes.

Historically, the first theoretical accounts of SPPs were in the context of surface bound radio waves. These were given by Arnold Sommerfeld and Jonathan Zenneck who described the propagation along a finite-thickness conducting wire and the surface of an extended conductor, e. g. the earth's surface, respectively [1, 2]. Around the same time, Robert W. Wood observed anomalous dark lines in the diffraction spectrum from a metallic grating [3], which Ugo Fano later connected to the earlier theoretical work. Fano also introduced the concept of the *polariton* – coupled oscillations of bound electrons and photons inside media [4, 5]. Finally, Rufus Ritchie linked the anomalies to the excitation of surface-plasmons [6]. In the same year, Andreas Otto, Erich Kretschmann and Heinz Raether presented methods to optically excite SPPs on metal surfaces [7, 8].

LSPRs on the contrary, have been employed in the form of colloidal gold by artists since Roman times to stain glass yielding, notably, vibrant reds. The first scientific experimental study was carried out by Michael Faraday who examined the interaction of light with gold solutions and described the various colors that can be observed [9]. Henry Siedentopf and Richard Szigmondy later on produced gold-stained glasses in the lab [10], which formed the basis for J. C. Maxwell Garnett's theoretical investigations in light of the recently developed Drude model and Rayleigh scattering [11]. A full theoretical framework for the interaction of small metal particles with light was worked out by Gustav Mie in 1908 [12].

In the last decade, plasmonics has gained tremendous interest due to its ability to concentrate light into sub-wavelength volumes making it the prime enabling factor in the ongoing quest for ever smaller photonic components. Its promise to revolutionize the field extends to applications as varied as optical interconnects, modulators, image forming systems, sensing and detection [13]. In particular, LSPRs in the form of metal nanoparticles can serve as artificial atoms. Their collective response to incident light allows for the creation of novel optical materials, so called *metamaterials*, with entirely tailorable optical responses that cannot be found in nature. Such properties include negative refraction [14–16], perfect absorption [17], chirality [18], and non-linear effects [19, 20]. However, this requires structure sizes that are smaller than the involved wavelengths. With rapid advances both in top-down (electron beam lithography [21], direct laser writing [22], focused ion beam lithography [23]) and bottom-up (self-assembly [24], chemical synthesis [25]) fabrication techniques, a whole host of structures have been realized down to the visible (VIS) spectral range.

In this thesis, we focus in the two main parts on two aspects of current research in the field of plasmonics: active metasurfaces and chiral plasmonics for enhanced circular dichroism spectroscopy. To this end, we utilize a variety of fabrication and simulation methods to study and realize various complex plasmonic geometries. Additionally, we incorporate the chalcogenide phase-change material GeSbTe in metasurface and chiral structures, to achieve hybrid plasmonic systems with post-fabrication tunable properties. The individual topics are presented with more specific introductions at the beginning of each chapter.

Chapter 2 presents the general theoretical background of macroscopic electrodynamics and plasmonics that will be needed for both metasurfaces and chiral plasmonics. Furthermore, the phase-change material GeSbTe is introduced as well as various simulation and fabrication techniques.

Chapter 3 deals with the design and realization of active metasurfaces for beam steering and varifocal lensing. The concept of geometrical phase based metasurfaces is explained.

Chapter 4 gives a brief historical overview over the development of chirality as a field of scientific study to set the background for the following chapters.

Chapter 5 introduces the theoretical concepts that are specific to chiral plasmonics and plasmon-enhanced circular dichroism spectroscopy. The measurable quantities as well as chiral constitutive equations and the chiral wave equation is introduced.

Chapter 6 discusses plasmonic analogs of electronic models of optical activity. In particular the one-electron (Condon) and two-electron (Born-Kuhn) models are reframed in the context of plasmonic systems. Additionally, we establish an alternative view on the two-electron theory in light of a plasmon hybridization model. Finally, we use the insights from the two-electron model to assess the chiral optical modes of a spiral-ramp structure. The results presented here have been published in [A1, A2].

Chapter 7 uses the chiral dimer structure developed as the plasmonic analog of the two-electron system as the building block for active chiral plasmonic devices. As in Chapter 3 we incorporate GeSbTe into our static plasmonic structure to achieve tunable optical response. We realize a chiral device exhibiting wavelength tunable circular dichroism and a second one that flips the sign of its circular dichroism response when actuated. The results presented here have been published in [A3].

Chapter 8 finally presents the integration of chiral constitutive equations introduced in Chapter 5 into a commercial finite element method (FEM) solver to numerically study the strength of plasmon-enhanced circular dichroism. To this end, we study the circular dichroism response of achiral and chiral plasmonic structures in conjunction with chiral media patches and compare these results to signals obtained from the chiral media by themselves. The results presented here have been published in [A4].

Chapter 9 summarizes the main results of this thesis and gives an outlook on where further work building on the concepts developed here may lead.

2.1 MACROSCOPIC ELECTRODYNAMICS

At the core of this thesis lies the study of the interaction of electromagnetic (EM) waves with metal particles. Therefore, this chapter supplies the basic theoretical framework for adequately describing such interactions. It is a brief summary of the two main parts comprised in the study of matter via EM waves. Firstly, a phenomenological model of media permeated by EM fields is given through the macroscopic *Maxwell's equations*. Secondly, the response of electrons in matter to external stimuli encompassed in the concept of the *complex permittivity* for linear, isotropic and nonmagnetic media is discussed.

The propagation of light as an EM wave is governed by *Maxwell's equations*, a set of four partial differential equations. These equations linking the electric field \mathbf{E} , the magnetic field \mathbf{H} , the electric displacement \mathbf{D} and the magnetic induction \mathbf{B} , in SI units, take the form

$$\nabla \times \mathbf{E}(\mathbf{r}, t) = -\frac{\partial \mathbf{B}(\mathbf{r}, t)}{\partial t}, \quad (2.1)$$

$$\nabla \times \mathbf{H}(\mathbf{r}, t) = -\frac{\partial \mathbf{D}(\mathbf{r}, t)}{\partial t} + \mathbf{j}_{\text{ext}}(\mathbf{r}, t), \quad (2.2)$$

$$\nabla \cdot \mathbf{D}(\mathbf{r}, t) = \rho_{\text{ext}}(\mathbf{r}, t), \quad (2.3)$$

$$\nabla \cdot \mathbf{B}(\mathbf{r}, t) = 0, \quad (2.4)$$

where ρ_{ext} denotes the external charge density and \mathbf{j}_{ext} the external current density [26]. This is known as the *macroscopic* version of Maxwell's equations, which can be understood as a phenomenological treatment of the behavior of EM waves in media. Instead of explicitly dealing with microscopic charges on an atomistic scale, in this coarse grained version, charge and current densities are considered as averaged continuous functions[27, 28].

It is often more practical to use Maxwell's Equations in the integral form, which can be obtained from the differential form through the use of Gauss' and Stokes' theorems [26]

$$\oint_S \mathbf{D} \cdot d\mathbf{n} = \int_V \rho_{\text{ext}} dV \quad (2.5)$$

$$\oint_S \mathbf{B} \cdot d\mathbf{n} = 0 \quad (2.6)$$

$$\oint_C \mathbf{H} \cdot d\mathbf{l} = \int_{S'} \left(\mathbf{J} + \frac{\partial \mathbf{D}}{\partial t} \right) \cdot d\mathbf{n} \quad (2.7)$$

$$\oint_C \mathbf{E} \cdot d\mathbf{l} = \int_{S'} \frac{\partial \mathbf{B}}{\partial t} \cdot d\mathbf{n}, \quad (2.8)$$

where V is the volume enclosed by the surface S with outward normal vector \mathbf{n} , and the surface S' is bounded by the contour C with tangential vector \mathbf{l} .

2.1.1 Constitutive Equations

In order to obtain self-consistent solutions for the fields, Maxwell's equations need to be complemented by relations that account for the response of matter immersed in EM fields. This is achieved through material equations known as *constitutive equations*, which in their generally valid form are

$$\mathbf{D} = \varepsilon_0 \mathbf{E} + \mathbf{P}, \quad (2.9)$$

$$\mathbf{H} = \frac{1}{\mu_0} \mathbf{B} - \mathbf{M}, \quad (2.10)$$

with polarization \mathbf{P} and magnetization \mathbf{M} . The polarization is defined as the net internal dipole moment per unit volume

$$\mathbf{P} = \frac{\Delta \mathbf{p}}{V} \quad (2.11)$$

and is connected to the internal current density via

$$\partial_t \mathbf{P} = \mathbf{j}_{\text{int}}. \quad (2.12)$$

2.1.2 Linear Isotropic Media

For the first part of this thesis, we will limit ourselves to linear, isotropic and homogeneous media for which the general constitutive relations Eqs. (2.9) and (2.10) can be simplified to

$$\mathbf{D} = \varepsilon_0 \varepsilon \mathbf{E}, \quad (2.13)$$

$$\mathbf{H} = \frac{1}{\mu_0 \mu} \mathbf{B}, \quad (2.14)$$

with the dielectric constant or relative permittivity ε and the magnetic permeability μ , which equals unity for nonmagnetic ($\mathbf{M} = 0$) materials. When an external field \mathbf{E} is applied to a linear, isotropic medium, the microscopic dipoles tend to align along the field lines such that the polarization \mathbf{P} will be parallel to \mathbf{E} , which is expressed as

$$\mathbf{P} = \varepsilon_0 \chi \mathbf{E}. \quad (2.15)$$

where the *electric susceptibility* of the medium is defined as

$$\chi = 1 - \varepsilon. \quad (2.16)$$

This material property further manifests itself in *Ohm's law*

$$\mathbf{j}_{\text{int}} = \sigma \mathbf{E}, \quad (2.17)$$

connecting the electric field \mathbf{E} and the internal current density \mathbf{j}_{int} via the conductivity σ holds. Using Eq. (2.11) and Eqs. (2.9) and (2.10) in their frequency domain versions and noting that for time harmonic fields with angular frequency ω $\partial_t \rightarrow -i\omega$, we obtain an important relationship between the dielectric constant ε and the conductivity σ

$$\varepsilon = 1 + \frac{i\sigma}{\varepsilon_0 \omega}, \quad (2.18)$$

which in general are complex functions. In the optical regime, experimental dielectric constants can be measured through *ellipsometry* from which the complex refractive index $\tilde{n} = n + i\kappa = \sqrt{\varepsilon}$ governing

refraction and absorption of light waves in media can be obtained. We then develop the following relations:

$$\varepsilon_1 = n^2 - \kappa^2, \quad (2.19)$$

$$\varepsilon_2 = 2n\kappa, \quad (2.20)$$

$$n = \sqrt{\frac{\varepsilon_1}{2} + \frac{1}{2}\sqrt{\varepsilon_1^2 + \varepsilon_2^2}}, \quad (2.21)$$

$$\kappa = \sqrt{-\frac{\varepsilon_1}{2} + \frac{1}{2}\sqrt{\varepsilon_1^2 + \varepsilon_2^2}}, \quad (2.22)$$

with ε_1 and ε_2 as real and imaginary parts of the dielectric function respectively.

2.1.3 Kramers-Kronig Relations

The response of the internal dipole moments to external electric fields is in general not instantaneous and temporally dispersive such that Eq. (2.13) in time domain, more appropriately, takes the form

$$\mathbf{D}(\mathbf{r}, t) = \varepsilon_0 \int_{-\infty}^{\infty} dt' \varepsilon(t - t') \mathbf{E}(t'), \quad (2.23)$$

where the permittivity ε serves as a *linear response function*. In order to preserve causality, $\varepsilon(t) = 0$ for $t < 0$, i. e., the electric displacement \mathbf{D} can not be influenced by future external fields \mathbf{E} . Using results from complex analysis, the requirement of causality directly leads to relations between real and imaginary parts of the permittivity in frequency space, the *Kramers-Kronig relations*[26]

$$\Re[\varepsilon(\omega)] = \mathcal{P} \int_{-\infty}^{\infty} \frac{d\omega'}{\pi} \frac{\Im[\varepsilon(\omega')]}{\omega' - \omega}, \quad (2.24)$$

$$\Im[\varepsilon(\omega)] = -\mathcal{P} \int_{-\infty}^{\infty} \frac{d\omega'}{\pi} \frac{\Re[\varepsilon(\omega')]}{\omega' - \omega}, \quad (2.25)$$

where \mathcal{P} denotes the principal value of the integral. In particular,

$$\varepsilon(\omega) = \int_{-\infty}^{\infty} \frac{d\omega'}{\pi} \frac{\Im[\varepsilon(\omega')]}{\omega' - \omega - i\delta}, \quad (2.26)$$

where δ is a small real number and indicates that the integration is carried out just below the real axis. Therefore, knowing the imaginary part of ε , which for weakly absorbing materials is directly related to the absorption coefficient κ (Eq. (2.22)), let's us reconstruct the full response function.

2.1.4 Wave Propagation in Linear Isotropic Media

In the absence of charges and currents, substituting Eqs. (2.9) and (2.10) into Eqs. (2.1) and (2.2) and taking the curl of the resulting equations yields

$$\nabla^2 \mathbf{E} = \mu_0 \mu \varepsilon_0 \varepsilon \frac{\partial^2 \mathbf{E}}{\partial t^2}. \quad (2.27)$$

Comparing this to the standard wave equation

$$\frac{\partial^2 y}{\partial x^2} = \frac{1}{v^2} \frac{\partial^2 y}{\partial t^2}, \quad (2.28)$$

where v is the velocity at which the wave travels, leads to

$$\frac{1}{v^2} = \mu_0 \mu \varepsilon_0 \varepsilon. \quad (2.29)$$

In vacuum, $\varepsilon = \mu = 1$ and the wave velocity is equal to the speed of light c ; in a medium, this becomes

$$v = \frac{1}{\varepsilon_0 \varepsilon} c. \quad (2.30)$$

This defines the *refractive index* n as the ratio of the velocity of light in vacuum and in a medium

$$n = \frac{c}{v}. \quad (2.31)$$

The solutions to Eq. (2.27) are of the plain wave form

$$\mathbf{E}(z, t) = E_0 \mathbf{J} e^{i(kz - \omega t)}, \quad (2.32)$$

where z is the direction of travel, $k = \frac{2\pi}{\lambda}$ the magnitude of the wave vector, E_0 the amplitude of the wave and \mathbf{J} the *Jones vector* that encodes the *polarization*. Linearly polarized light (LP) EM waves can then be represented by

$$\mathbf{J}_{LP} = \begin{pmatrix} \cos \phi \\ \sin \phi \\ 0 \end{pmatrix}, \quad (2.33)$$

and circularly polarized light (CP) light as

$$\mathbf{J}_{CP} = \frac{1}{\sqrt{2}} \begin{pmatrix} 1 \\ \pm i \\ 0 \end{pmatrix}, \quad (2.34)$$

where '+' should be taken for right-handed circularly polarized (RCP) and '-' for left-handed circularly polarized (LCP) light.

2.1.5 EM Waves at Interfaces

In order to obtain the boundary conditions for interfaces between media, we integrate Eqs. (2.5) and (2.6) for a Gaussian pill box of infinitesimal thickness yielding [29]

$$(\mathbf{D}_2 - \mathbf{D}_1) \cdot \mathbf{n} = \sigma \quad (2.35)$$

$$(\mathbf{B}_2 - \mathbf{B}_1) \cdot \mathbf{n} = 0. \quad (2.36)$$

Therefore, the normal component of \mathbf{B} is continuous across the boundary, while the normal component of \mathbf{D} is discontinuous by the amount of a surface charge σ .

To carry out the path integrals Eqs. (2.7) and (2.8), we choose a rectangular loop with side length l around an infinitely small area. Orienting the loop such that its area is perpendicular to the boundary and integrating along it leads to

$$\mathbf{n} \times (\mathbf{E}_2 - \mathbf{E}_1) = 0 \quad (2.37)$$

$$\mathbf{n} \times (\mathbf{H}_2 - \mathbf{H}_1) = \mathbf{K}. \quad (2.38)$$

indicating that the tangential component of E is continuous across the boundary, while the tangential component of H differs by the amount of a surface current K .

Applying the boundary conditions for a time-harmonic plane wave incident on an interface results in the *Fresnel equations* for transmission and reflection amplitudes [30]:

$$r^s = \frac{n_1 \cos \alpha - n_2 \cos \beta}{n_1 \cos \alpha + n_2 \cos \beta}$$

$$t^s = \frac{2n_1 \cos \alpha}{n_1 \cos \alpha + n_2 \cos \beta}$$

$$r^p = \frac{n_2 \cos \alpha - n_1 \cos \beta}{n_2 \cos \alpha + n_1 \cos \beta}$$

$$t^p = \frac{2n_1 \cos \alpha}{n_2 \cos \alpha + n_1 \cos \beta}.$$

The superscripts s (perpendicular) and p (parallel) indicate that the coefficients are polarization dependent; α and β are the incident and refracted angles of the plane wave respectively.

2.2 PLASMONICS

Here, we briefly summarize the main concepts needed to describe the localized surface plasmon polariton resonance (LSPR) and grating resonances that couple to surface plasmon polariton (SPP)s in periodic arrangements of metal nanoparticles. In particular, we stress the theoretical similarity of a LSPR to a damped harmonic oscillator. A more detailed account can be found in [31–33].

2.2.1 Optical Properties of Metals

When light impinges on matter, it excites charge oscillations within the medium. Therefore, the essence of the interaction can be captured by combining the concept of a harmonic oscillator from classical mechanics with results from electrodynamics. In the case of metals, the main characteristically contributing component arises due to the presence of a large amount of free electrons that act as a plasma. This part can be described by the optical Drude model, which is a special case of the Lorentz oscillator model when the restoring force is zero [34]

$$m\ddot{\mathbf{x}} + m\gamma\dot{\mathbf{x}} = -e\mathbf{E}, \quad (2.39)$$

where e is the electron charge and γ the collision frequency of electrons with the lattice. Using the ansatz of a time-harmonic field $\mathbf{E}(t) = E_0 e^{-i\omega t}$, the solution

$$\mathbf{x}(t) = \frac{e}{m(\omega^2 + i\gamma\omega)} \mathbf{E}(t) \quad (2.40)$$

can be obtained. Since the macroscopic polarization can be written as

$$\mathbf{P} = -Nex, \quad (2.41)$$

where N is the electron charge density, we obtain

$$\mathbf{P} = -\frac{Ne^2}{m\omega^2 + i\gamma\omega} \mathbf{E}. \quad (2.42)$$

Substituting this into Eq. (2.9) and comparing coefficients yields the dielectric function of the free electron gas

$$\varepsilon(\omega) = 1 - \frac{\omega_p^2}{\omega^2 + i\gamma\omega}. \quad (2.43)$$

with the *plasma frequency*

$$\omega_p^2 = \frac{Ne^2}{\epsilon_0 m}. \quad (2.44)$$

Writing out the real and imaginary parts explicitly leads to

$$\epsilon_1(\omega) = 1 - \frac{\omega_p^2}{\omega^2 + \gamma^2} \quad (2.45)$$

$$\epsilon_2(\omega) = \frac{\omega_p^2 \gamma}{(\omega^2 + \gamma^2) \omega}. \quad (2.46)$$

The simple Drude model describes the permittivity of gold, which is the primary plasmonic material used in this thesis, very well in the near infrared (NIR) to mid-infrared (MIR) region of 1 - 6 μm . All experiments in this thesis were carried out in this spectral region. Figure 2.1 shows interpolated tabulated data taken from [35] with a fitted Drude model function. The fit parameters are $\omega_p = 1823$ THz and $\gamma = 0$ for ϵ_1 and $\omega_p = 1823$ THz and $\gamma = 16$ THz for ϵ_2 .

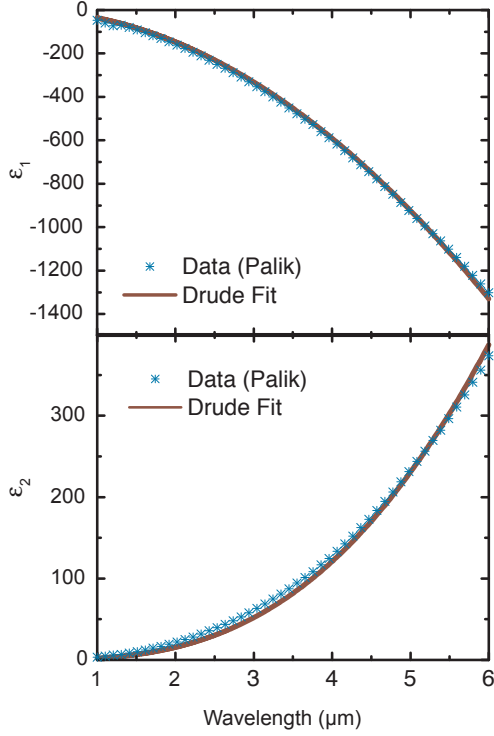


FIGURE 2.1. Dielectric data for gold [35] with Drude model fits.

Considering the case of a lightly damped system ($\gamma = 0$), Eq. (2.43) reveals the main characteristic of metals, namely that they possess high reflectivity in the optical regime. The dielectric function in this case is

$$\varepsilon_1(\omega) = 1 - \frac{\omega_P^2}{\omega^2}, \quad (2.47)$$

which can be substituted into the formula for reflectivity R

$$R = \left| \frac{\tilde{n} - 1}{\tilde{n} + 1} \right|^2. \quad (2.48)$$

Plotting this, we see that R is unity for frequencies ω below the plasma frequency ω_p , then starts to decrease for $\omega > \omega_p$ and finally falls to zero for $\omega \rightarrow \infty$. This dependency is shown in Fig. 2.2. Since typical plasma frequencies correspond to ultraviolet (UV) wavelengths, metals are to first approximation highly reflective for incident light frequencies up to ω_p . For higher frequencies, metals become transparent.

Note that for real noble metals such as gold, silver and copper, the permittivity and, therefore, reflectivity deviate significantly from this idealized behavior at shorter wavelengths. This is due to *interband transitions* that in principle can be modeled through a bound electron Lorentz oscillator following the equation of motion

$$m\ddot{x} + m\gamma\dot{x} + m\omega_0^2x = -eE, \quad (2.49)$$

where ω_0 is the resonance frequency of the bound electron. Compared to Eq. (2.43) this leads to an additional term of the form

$$\epsilon_{\text{inter}} = \frac{f_i}{\omega_p^2 - \omega^2 - i\gamma\omega}, \quad (2.50)$$

which would be added to Eq. (2.43).

Bulk Plasmons

Equation (2.47) indicates that ω_p plays a prominent role since the permittivity becomes zero for $\omega = \omega_p$. Indeed, this 'instability' of the dielectric constant can be associated with harmonic plasma oscillations commonly referred to as *bulk* or *volume plasmons*. These are longitudinal oscillations that can typically only be excited upon bombardment with charged particles as is the case in electron energy loss spectroscopy (EELS) [36].

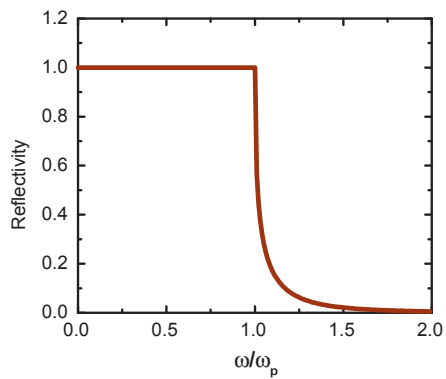


FIGURE 2.2. Reflectivity R of an undamped free electron plasma. R is unity for frequencies $\omega \leq \omega_p$ up until the *plasma edge*, then decreases for $\omega > \omega_p$ and finally falls to zero for $\omega \rightarrow \infty$.

2.2.2 Surface Plasmons and Grating Modes

Collective oscillations of the electron density at the surface of a metal Fig. 2.3 (c) are naturally associated with EM waves. Thus, they are *polaritons*. Assuming the electric field of an EM wave that is propagating along the z -direction to be Fig. 2.3 (a)

$$E = E_0 e^{i(k_{\text{spp}}x + k_z - \omega t)}, \quad (2.51)$$

we can solve Maxwell's equations at the interface between two materials with dielectric constants ϵ_m and ϵ_d by employing the continuity relations (Eqs. (2.35) to (2.38)).

This results in the boundary conditions.

$$\frac{k_{z,d}}{\epsilon_d} + \frac{k_{z,m}}{\epsilon_m} = 0, \quad (2.52)$$

$$k_x^2 + k_{zi}^2 = \epsilon_i \left(\frac{\omega}{c} \right)^2 \quad i = m, d \quad (2.53)$$

Solving this leads to the dispersion relation

$$k_x = k_0 \sqrt{\frac{\epsilon_m \epsilon_d}{\epsilon_m + \epsilon_d}}, \quad (2.54)$$

where k_x is the magnitude of the wavevector of the excited SPP, k_0 is the wavevector of the incident light and $\epsilon_{m,d}$ are the permittivity of the metal and the dielectric respectively.

In order to obtain a propagating wave in x -direction and a bound one in z -direction Fig. 2.3 (b), the conditions

$$\epsilon_m \cdot \epsilon_d < 0, \quad (2.55)$$

$$\epsilon_m + \epsilon_d < 0 \quad (2.56)$$

have to be fulfilled. Since noble metals have a very large negative real part of the dielectric function Fig. 2.1, such modes can form at the interface between dielectric and metals.

In order to excite SPPs, energy and momentum have to be matched to the incident light. From Fig. 2.4, one can see that additional momentum needs to be provided to free space light to couple to an SPP. Apart from the Kretschmann and Otto configurations [37], this can

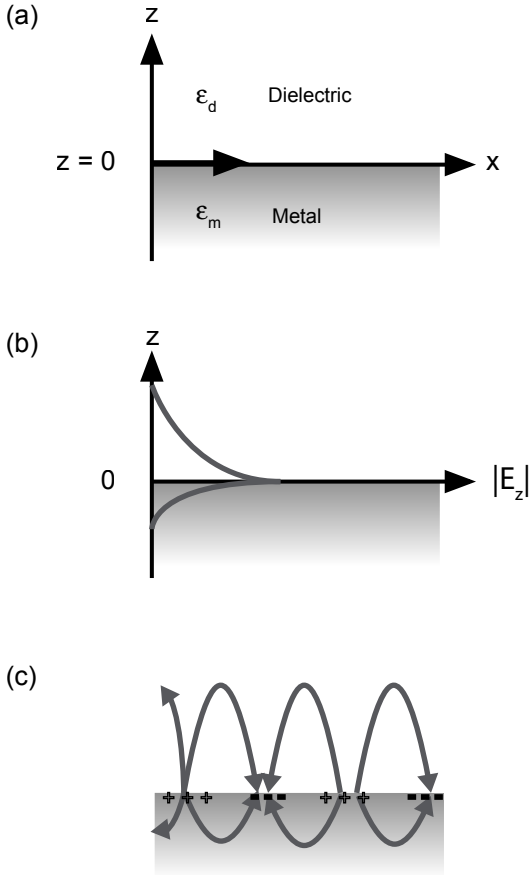


FIGURE 2.3. (a) Coordinate system used for SPP discussion. $z = 0$ is located at the interface between the metal and the dielectric, the surface plasmon propagates in $+x$ -direction. (b) Field amplitudes as a function of the distance from the interface. The z -component of the E-field decays exponentially on both sides of the interface with a shorter penetration depth into the metal.

be achieved through gratings that provide an additional momentum $k_G = 2\pi/\Lambda$, where Λ denotes the grating period. This is the physical phenomenon behind the observation of Wood's anomalies for the reflection from metallic gratings. In this thesis, we oftentimes use periodically arranged nanoparticles (discussed in the next section), which also exhibit propagating surface modes. These can be effectively suppressed by using a design where the particles are randomly distributed.

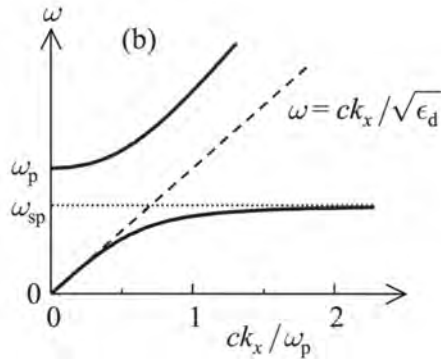


FIGURE 2.4. The dispersion relations for the bulk (upper branch) and surface plasmons (lower branch) [32]. The dashed line indicates the free space light dispersion.

Since the linewidth of SPPs is very narrow and its spectral position depends on ϵ_d , they are widely employed in sensor applications.

2.2.3 Optical Antennas

Spherical Particles

Apart from the volume and propagating plasmons, localized plasmon resonances are possible. The most instructive configuration to consider here is a metallic sphere onto which an incident electric field E_{inc} impinges (Fig. 2.5 (a)). The electric field induces a dipole moment

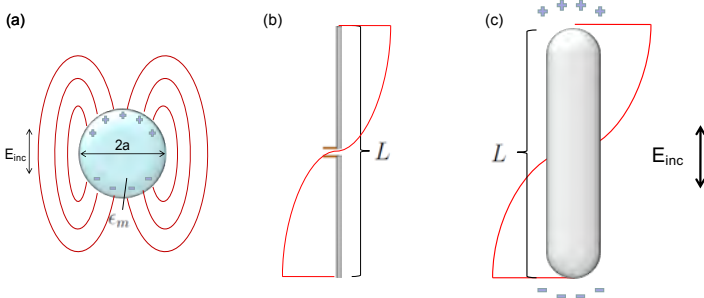


FIGURE 2.5. (a) An incident electric field E_{inc} displaces the charges inside a small metallic sphere and thus induces a dipole moment. (b) radio frequency (RF) antennas exhibit resonances that can be calculated from purely geometrical considerations. (c) For nanorods, this geometrical consideration needs to be modified such that it takes the short effective plasmon wavelength into account and the non-trivial phase shift upon reflection from the ends of the nanorod.

$$\mathbf{p} = \alpha \mathbf{E}_{\text{inc}} \quad (2.57)$$

where α is the polarizability of the particle. In the quasi-static limit, i. e., for $a \ll \lambda$, this can be evaluated using *Mie theory*. For a particle located in air with $n_{\text{air}} = 1$ the result is [38, 39].

$$\alpha = 4\pi\epsilon_0 a^3 \frac{\epsilon(\omega) - 1}{\epsilon(\omega) + 2}. \quad (2.58)$$

This expression diverges for the case

$$\epsilon(\omega) = -2, \quad (2.59)$$

which leads to a so-called *Fröhlich resonance*. When this condition is met, the conduction electrons are resonantly excited by the incident light field and strongly absorb and scatter. The absorbed and scattered intensities depend on the size of the particle. Inserting the Drude metal dielectric function Eq. (2.43), yields

$$\alpha = 4\pi\epsilon_0 a^3 \frac{\omega_0^2}{\omega - \omega_0^2 - i\gamma\omega}, \quad (2.60)$$

with the resonance frequency

$$\omega_0 = \frac{1}{\sqrt{3}}\omega_p, \quad (2.61)$$

where we assume that the sphere is located in air with $n_{\text{air}} = 1$. Fig. 2.6 shows the real and imaginary parts of the polarizability as a function of ω/ω_0 for $\gamma = \omega_0/2$. Note that these are Kramers-Kronig related as discussed in Section 2.1.3 and show an absorptive and dispersive behavior respectively.

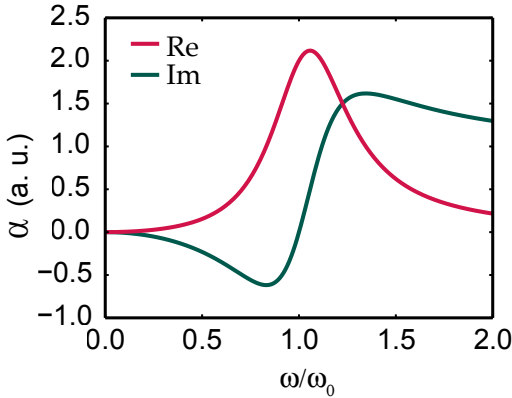


FIGURE 2.6. Real (red) and imaginary (green) parts of the polarizability α of a small metal sphere with $\gamma = \omega_0/2$.

For small particles, the scattering and absorption cross sections are given by [38]

$$C_{\text{scat}} = k^4 |\alpha|^2, \quad (2.62)$$

$$C_{\text{abs}} = k \Im [\alpha], \quad (2.63)$$

where $k = 2\pi/\lambda$. Therefore, for small particles absorption dominates, which only scales with a^3 . For large particles, scattering dominates as it scales rapidly with a^6 .

Rod-shaped Particles

In this thesis, we mostly encounter rod-shaped particles. They exhibit a pronounced dipolar character even for sizes that do not fall into the quasi-static limit. To qualitatively predict their spectral resonance positions, we can look to RF antennas as depicted in Fig. 2.5 (b). These can be considered to be made of a perfect electric conductor (PEC) since, in this spectral region, metals approximately have an infinitely negative real dielectric constant with negligible losses, i. e., imaginary part of the permittivity. The resonance condition can be easily obtained through geometrical considerations: the RF antenna is resonantly excited for integer multiples of half a wavelength [40]

$$L = n \frac{\lambda}{2}, \quad (2.64)$$

where L is the length of the RF antenna. Therefore, the antenna exhibits multiple resonances that are equidistant in frequency space.

Nanorod antennas have sizes from roughly 100 nm to several microns. Technically, the latter would not qualify for the prefix *nano*, however, this is a frequently used blanket term when dealing with lithographically defined metallic rod particles. Qualitatively, they share with their bigger counterparts the occurrence of fundamental and higher order modes. However, the precise spectral location is strongly dependent on the material, size and aspect ratio [41]. One can describe the physical phenomenon involved in the formation of these modes as a Fabry-Pérot resonance of a waveguide plasmon where an effective wavelength of a insulator-metal-insulator (IMI) waveguide mode is used [42–44]. Additionally, this Fabry-Pérot resonance is modified such that the reflection coefficient is complex, which leads to a non-trivial phase pick-up when the waveguide plasmon reflects from the ends of the nanorod. The qualitative similarity between nanorods and RF antennas lead to the coining of the term *optical antenna* in 2003 [45]. This term is particularly suited to the description of MIR rod-shaped metallic particles, which are used throughout this thesis.

Field-Enhancement

Both spherical and rod-shaped particles exhibit field-enhancement at the antipodes that are aligned with the E -field direction when they are

resonantly excited. In the case of the rod-shaped metallic nanoparticle, the field-enhancement is additionally aided by the so-called *lightning-rod effect* (Fig. 2.7 (a)). The higher the curvature of the tip of an antenna, the denser the field lines. Therefore, it is desirable to produce very sharp tips when field-enhancement is the effect one is after. Fig. 2.7 (b) shows a full field simulation of the field intensity of a 150 nm long gold nanorod excited with incident light of 550 nm.

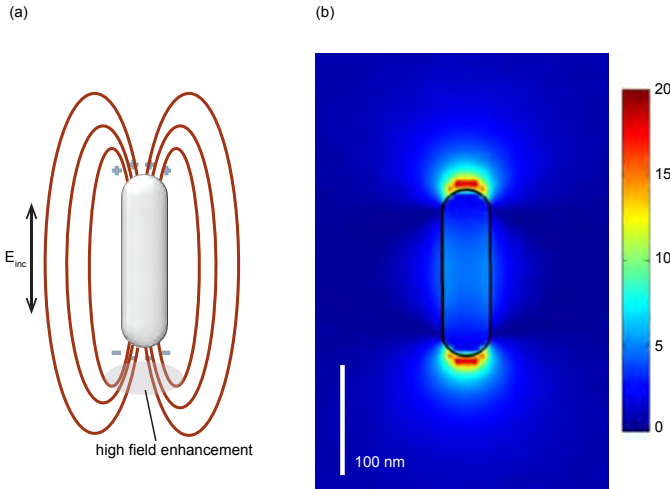


FIGURE 2.7. (a) Lightning rod effect: due to high curvature of the ends of the rod-shaped metallic particle, the field line density is higher than at other locations leading to field-enhancement. (b) Field intensity of a gold nanorod with 150 nm length excited along its axis with an incident light wavelength of 550 nm.

Finally, it should be stressed that plasmonic nanoparticles can be very well modeled as mechanical *Lorentz oscillators*. For the spherical particle this can be directly seen from Eq. (2.60), which yields a Lorentzian lineshape. However, also particles with more complicated shapes that cannot be treated analytically exhibit this lineshape; in particular, in their fundamental mode. This is due to the primarily dipolar nature of the excited nanoparticle modes.

2.2.4 Plasmon Hybridization

While Mie Theory can go far in correctly modeling isolated geometries as complex as, e. g., spherical particles with a dielectric core and a metal shell, it does not clearly reveal the underlying physical mechanisms. In the case of the core-shell particle, it is instructive to think of it in terms of molecular orbital *hybridization* between a metal sphere and a hollow metal cavity [46–48]. Other assemblies such as dimers [49–61], trimers [62–70], quadrumers [71–74], oligomers [21, 24, 74–79] and more complex structures [55, 80] can also be readily analyzed from the point of view of hybridized modes.

In this thesis, the hybridization of two nanorods (Fig. 2.8 (a)) is of particular importance as we will discuss the chiral version in Section 6.2 in detail. The equation of motion can be derived from a *coupled harmonic oscillator model*, where the coupled oscillating quantities are dipoles with interaction energy [26]:

$$W_{12} = \frac{\mathbf{p}_1 \cdot \mathbf{p}_2 - 3(\mathbf{n} \cdot \mathbf{p}_1)(\mathbf{n} \cdot \mathbf{p}_2)}{4\pi\epsilon_0|\mathbf{x}_1 - \mathbf{x}_2|^3}, \quad (2.65)$$

where \mathbf{x}_1 and \mathbf{x}_2 are the locations of the dipoles \mathbf{p}_1 and \mathbf{p}_2 respectively and \mathbf{n} is the unit vector in the direction $|\mathbf{x}_1 - \mathbf{x}_2|$. For collinear dipoles, this reduces to

$$W_{12} = -\frac{p_1 p_2}{2\pi\epsilon_0 d^3}, \quad (2.66)$$

with $d = |\mathbf{x}_1 - \mathbf{x}_2|$.

The force on dipoles $\mathbf{p}_{1,2}$ due to the other dipole respectively is given by

$$F_1 = -\frac{\partial W_{12}}{\partial p_1} = \kappa p_2 \quad (2.67)$$

$$F_2 = -\frac{\partial W_{12}}{\partial p_2} = \kappa p_1, \quad (2.68)$$

where all prefactors are incorporated into κ , which can be interpreted as a coupling constant.

This leads to the equation of motion of the coupled dipole system as

$$\ddot{p}_1 + \gamma_1 \dot{p}_1 + \omega_1^2 p_1 + \kappa p_2 = 0 \quad (2.69)$$

$$\ddot{p}_2 + \gamma_2 \dot{p}_2 - \omega_2^2 p_2 + \kappa p_1 = 0, \quad (2.70)$$

where $\gamma_{1,2}$ is the damping and $\omega_{1,2}$ the resonance frequencies of the uncoupled dipoles. Making the ansatz $p_{1,2} = A_{1,2} e^{-i\omega t}$ and assuming $\gamma = 0$, the eigenfrequencies of the coupled oscillators can be obtained from the quartic equation

$$\left(\omega_1^2 - \omega^2\right) \left(\omega_2^2 - \omega^2\right) - \kappa^2 = 0. \quad (2.71)$$

For weakly coupled oscillators $\kappa \ll \omega_2^2 - \omega_1^2$ this leads to

$$\tilde{\omega}_1^2 \approx \omega_1^2 - \frac{\kappa^2}{\omega_2^2 - \omega_1^2}, \quad (2.72)$$

$$\tilde{\omega}_2^2 \approx \omega_2^2 + \frac{\kappa^2}{\omega_2^2 - \omega_1^2}. \quad (2.73)$$

Therefore, the new energy levels are only slightly modified from the original uncoupled ones (Fig. 2.8 (b)).

For strongly coupled oscillators, the eigenfrequencies are

$$\tilde{\omega}_{1,2}^2 \approx \bar{\omega}^2 \pm \kappa, \quad (2.74)$$

where $\bar{\omega}^2 = (\omega_1^2 + \omega_2^2) / 2$. In this case, two new distinct modes form (Fig. 2.8 (c)) that are energetically separated by twice the interaction energy W_{12} .

Determining the associated eigenmodes reveals that the lower energy mode is symmetric, i. e., that the two dipoles oscillate in phase. On the contrary, the higher energy mode is anti-symmetric with the two dipoles oscillating 180° out of phase [81]. The two modes are thus also referred to as bonding (symmetric) and anti-bonding (anti-symmetric) modes analogous to the case of molecular orbital hybridization for the H_2^+ molecule ion [82]. As indicated by Eq. (2.66), the

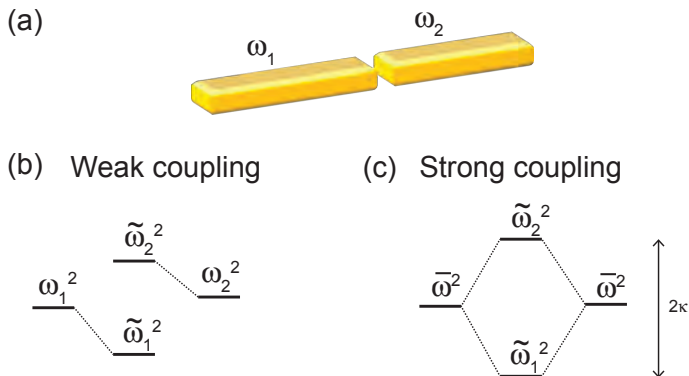


FIGURE 2.8. (a) Nanorod dimer with individual resonance energies proportional to ω_1^2 and ω_2^2 . (b) Energy diagram for weakly coupled dimers. (c) Energy diagram for strongly coupled dimers. The energy difference between the newly formed states is equal to twice the interaction energy between the two coupled dipoles.

coupling is distance dependent; an in-depth treatment of this can be found in [83].

Oftentimes, the picture of two coupled mechanical oscillators is invoked when discussing coupled dipole systems (Fig. 2.9). While the mechanical system also exhibits symmetric and anti-symmetric modes, the energy splitting is different [84, 85]. In the mechanical system, the symmetric mode behaves like the uncoupled oscillator since there is no tension on the coupling spring. Hence, whenever mechanical oscillators are pictured in the context of plasmonic hybridization, it should be kept in mind that it only serves as an analogy where the springs graphically depict the restoring force that for dipoles is really mediated by the Coulomb force.

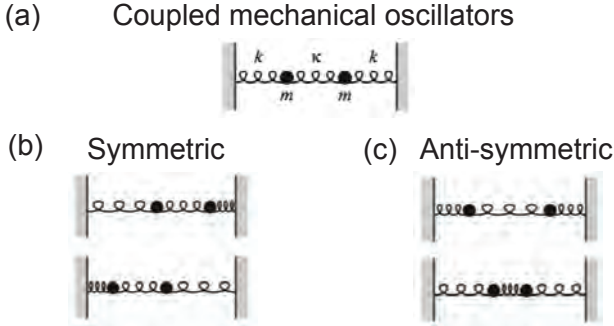


FIGURE 2.9. (a) Coupled mechanical oscillators. [85] (b) Symmetric mode: there is no tension on the coupling spring, therefore, the frequency and hence the energy is the same as in the uncoupled system. (c) Anti-symmetric mode.

2.3 PHASE CHANGE MATERIALS

The first metamaterials comprising of plasmonic structures were fully static, i.e., their geometry, material, dielectric environment and hence optical properties were fixed by design. However, introducing handles for post-fabrication control over plasmonic optical mode behavior is crucial for pushing metamaterials into the domain of reconfigurable devices [86] for applications as varied as all-optical nanophotonic circuits, imaging, sensors, data storage and displays. To this end, mechanical means that effect a deformation of the artificial material [87, 88], graphene [89–92] injection of free carriers in semiconductors [93–97], and materials such as VO_2 [98–100], gallium [101, 102], yttrium-hydride [103] and magnesium [104] have been successfully employed.

In this thesis, we utilize a phase-change material (PCM), i. e., a material with different optical and electrical properties in its amorphous and crystalline phases (Fig. 2.10), to realize active plasmonic devices Chapters 3 and 7. PCMs are amorphous semiconductors as-deposited that, when heated, form a crystalline phase above a certain crystallization temperature T_{cryst} but below their melting temperature T_{melt} .

The amorphous phase is associated with a low dielectric constant and, therefore, low reflectivity R but high resistivity Ω , which reverses for the crystalline phase. The phase change can be induced by both optical [105] and electrical [106] means on very short timescales. A typical (electrical) switching cycle is depicted in Fig. 2.10 (b). A pulse of ca. 100 ns duration is used to heat up a ca. 50 nm thick layer of Ge-Sb-Te (GST) above T_{cryst} to crystallize it. On the contrary, a very short but intense pulse is employed to briefly heat up the GST above its melting temperature T_{melt} . The material is then immediately melt-quenched to its amorphous state by dissipating the heat. PCMs have already

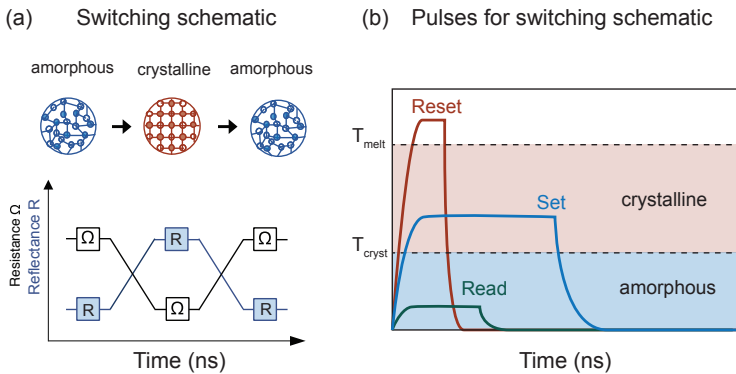


FIGURE 2.10. (a) Schematic PCM switching behavior: GST possesses low reflectivity and high resistivity in the amorphous state and high reflectivity and low resistivity in the crystalline state. (b) Typical pulse forms and timescales used in the electrical switching of GST.

been commercialized with great success in the form of rewritable optical storage media (DVD-RW, CD-RW), which attests to their robustness and cyclability of the switching process. Furthermore, they are promising candidates for the realization of a new type of solid state random access memory [107], neuron-type systems [108] and displays[109].

For MIR active plasmonic applications, the GST stoichiometry with element ratio 3:2:6 (GST-326) (Fig. 2.10), which is located along the

GeTe-Sb₂Te₃ tie-line, is particularly well-suited because of its low optical losses in the MIR spectral region [110] due to the negligibly small imaginary part of the refractive index (Fig. 2.11).

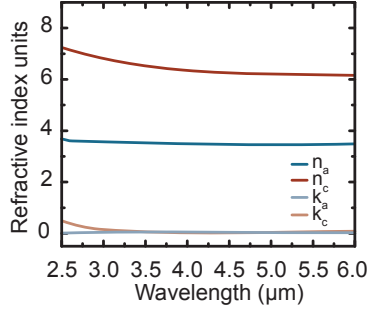


FIGURE 2.11. (a) GST chalcogenide alloy family. (Adapted from [111] with permission.) (b) Real and imaginary parts of the refractive index for GST-326 in the spectral region from 2.5 μm - 6 μm. (Replotted with data from [112])

2.4 GENERAL METHODS

2.4.1 *Experimental Methods*

The experiments presented in this thesis use a variety of methods that are each described in the relevant sections where they are needed. Here, methods that are common to most experiments are described.

Electron Beam Lithography

We use a standard electron beam lithography procedure to define arbitrarily shaped planar metallic structures. For this, we employ a Raith eLine system at 20 kV acceleration voltage and 20 μm aperture size. As resist, we spin-coat a polymethyl methacrylate (PMMA) double layer with the first layer having 200K (3.5%) and the second 950K (1.5%) chain length. This produces an undercut since the first layer dissolves more quickly during development. Furthermore, we apply

a conducting polymer (Espacer 300Z) on top of the resist in order to avoid charging effects during writing. After exposure and development with MIBK:isopropyl alcohol, Cr and Au are thermally evaporated onto the samples. Finally, a lift-off is carried out in N-Ethyl-2-pyrrolidon for 2 hours at 65°C. Figure 2.12 shows the result of a fabricated structure where the lift-off was incomplete.

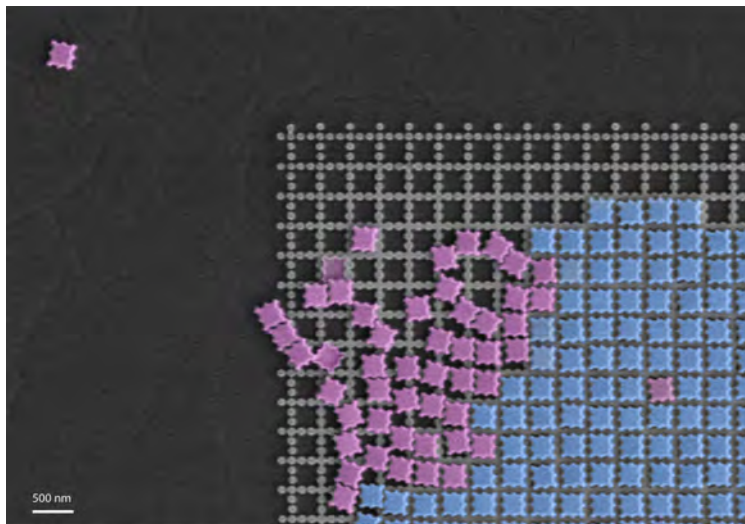


FIGURE 2.12. Single layer electron beam lithography (false colors): the grid type structure presents the originally defined geometry; however, due to incomplete lift-off, the rigged patches did not wash away fully.

Thin Film deposition

The plasmonic material used in this thesis is gold, which is always applied with a chromium adhesion layer. Both materials are deposited using thermal evaporation using a Univex 350 system by Oerlikon. The metals are evaporated from tungsten boats and impinge on a rotating sample holder in order to achieve maximum isotropy in conjunction with the double layer poly(methyl methacrylate) (PMMA) masks generated using standard electron beam lithography (EBL) that

exhibit an undercut. The bell jar type vacuum chamber is pumped down to a pressure of ca. 1×10^{-6} mbar. For a typical fabrication, 2 nm of chromium is evaporated at a rate of 0.5 \AA s^{-1} and 40 nm of gold at a rate of 2 \AA s^{-1} . The exact values are given for the specific cases in the methods sections of the presented experiments.

Optical Characterization

The samples are all optically characterized using a Fourier transform infrared (FTIR) spectrometer by BRUKER coupled to a Vertex 80 microscope. For the spectral range relevant to this thesis ($1 \mu\text{m}$ to $5 \mu\text{m}$), the CaF_2 beam splitter together with a liquid nitrogen cooled mercury cadmium telluride (MCT) detector is used. The spectral resolution is set to 4 cm^{-1} and the background and sample spectra are taken with 64 and 32 scans respectively. The aperture size is kept at around $70 \mu\text{m} \times 70 \mu\text{m}$ for all samples. For linearly polarized light, a CaF_2 holographic polarizer from Thorlabs, Inc. is used in the beam path, which is additionally combined with a B. Halle broadband quarter waveplate to generate circularly polarized light (CPL).

2.4.2 *Simulation Methods*

While the interaction of light with simple plasmonic geometries such as spheres and ellipsoids can be analytically described, more complex structures require numerically solving Maxwell's equations Eqs. (2.1) to (2.4). To this end, different approaches exist of which finite-difference frequency-domain (FDTD), finite element method (FEM) and fourier modal method (FMM) are used in this thesis.

2.4.2.1 *FDTD*

The FDTD method is based on the discretization of time and space allowing for the treatment of partial differential equations employing central-differences of the form

$$\Delta_{\text{central}} [f(x)] = f\left(x + \frac{1}{2}h\right) - f\left(x - \frac{1}{2}h\right), \quad (2.75)$$

where h is called the spacing or step-size. In particular, the Cartesian discretization of space used in FDTD is carried out via so-called *Yee-Cells* (Fig. 2.13) where H- and E-field components are calculated at defined points (i, j, k) ; $i, j, k \in \mathbb{N}$ associated with the three spatial dimensions x , y and z for each time step $n\Delta t$, where n is an integer. The first partial derivatives in space and time can thus be expressed as [113]

$$\frac{\partial u}{\partial x}(i\Delta x, j\Delta y, k\Delta z, n\Delta t) = \frac{u_{i+1/2,j,k}^n - u_{i-1/2,j,k}^n}{\Delta x} + O(\Delta x^2), \quad (2.76)$$

$$\frac{\partial u}{\partial t}(i\Delta x, j\Delta y, k\Delta z, n\Delta t) = \frac{u_{i,j,k}^{n+1/2} - u_{i,j,k}^{n-1/2}}{\Delta t} + O(\Delta t^2). \quad (2.77)$$

Note, that the definition of the Yee-Cell and the notation of the derivatives including $1/2$ step sizes allows for the interleaving of H - and E - fields allowing for alternate updating of the fields, which results in a so-called *leapfrog algorithm* [114]. Each Yee-Cell can be assigned its own permittivity, therefore, allowing for modelling complicated geometries with multiple materials. Furthermore, commercial implementations, as used in this thesis, of the FDTD method such as *FDTD Solutions* by Lumerical Inc. include more sophisticated meshing methods that allow for sub-cell accuracy by employing conformal meshes.

The advantage of the FDTD method is that one simulation run yields a broadband frequency result since it is a time-domain method that uses finite excitation pulses. It can be used both for periodically arranged geometries as well as single structures when placing perfectly matched layer (PML)s [115] around the simulation domain. Furthermore, it is highly scalable when using shared and distributed memory parallel implementations.

2.4.2.2 FMM

In the FMM, a three-dimensional system is separated into several layers in order to find eigenmodes and eigenvalues of Maxwell's equations in each layer in a truncated Fourier space. This requires periodicity in one or both lateral directions. The solutions from the individual layers are combined by considering the boundary conditions between adjacent layers in a scattering matrix approach. Problems arise due

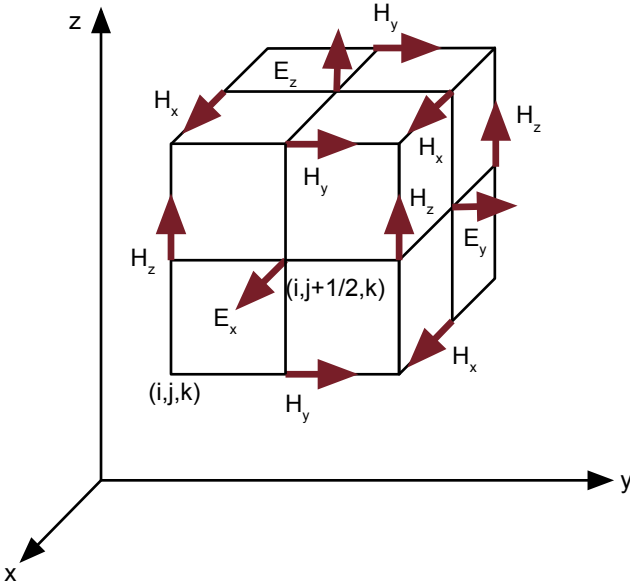


FIGURE 2.13. (a) Yee-Cell used for discretizing space in the FDTD method.

to the Fourier transform of piecewise constant functions. Some approaches have been developed in order to significantly increase the numerical accuracy of the Fourier modal method. The so-called factorization rules [116] improve the description of products of discontinuous functions as convolutions in Fourier space. Adaptive spatial resolutions [117] is a coordinate transformation technique to reduce the effective jump height of material discontinuities, and matched coordinates [118] are required for nontrivial lateral geometries. The advantage of the FMM method is that even large 3D geometries can be simulated at short calculation times while achieving good accuracy. However, only periodically arranged structures can be simulated. The FMM calculations in this thesis have been carried out using an in-house implementation.

2.4.2.3 FEM

As in the case of FDTD, the basic idea of FEM is the discretization of the simulation domain into small volume elements. Contrary to FDTD, tetrahedral meshes are used, which enables higher accuracies for curved geometries (Fig. 2.14). The solution to Maxwell's equations is approximated by a set of basis functions for each volume element that are determined using a variational calculus ansatz [119]. Subsequently, boundary conditions are applied between neighboring elements. This leads to a system of linear equations that can be solved by numerically inverting large sparse matrices, which however is very memory intensive. FEM is a frequency domain method and as such is able to directly use dielectric material data $\varepsilon(\omega)$. In this thesis, COM-SOL Multiphysics is used for carrying out FEM simulations.

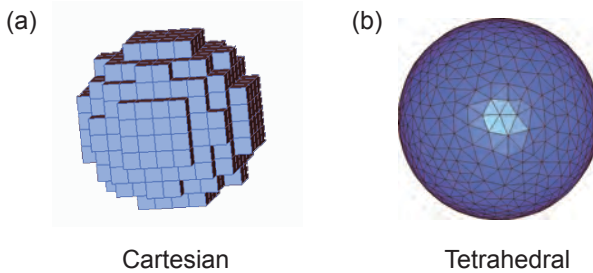


FIGURE 2.14. (a) Cartesian mesh used for discretizing space in the FDTD method. (b) Tetrahedral mesh used for discretizing space in the FEM method, which yields more accurate results for curved objects.

Part I

ACTIVE METASURFACES

Compact nanophotonic elements exhibiting adaptable properties are essential components for the miniaturization of powerful optical technologies such as adaptive optics and spatial light modulators. While the larger counterparts typically rely on mechanical actuation, this is undesirable on a microscopic scale due to inherent space restrictions. Here, we present a novel design concept for highly-integrated active optical components that employs a combination of resonant plasmonic metasurfaces and the phase-change material $\text{Ge}_3\text{Sb}_2\text{Te}_6$. In particular, we demonstrate beam steering and varifocal zoom lensing, thus, paving the way for a plethora of active optical elements employing plasmonic metasurfaces, which follow the same design principles.

INTRODUCTION

Form follows function [120] - this principle heeded by generations of modernist architects is not only a guideline, but rather the unyielding maxim dictated by Snell's law of refraction [30] when it comes to lens design [121]. The curvatures of material interfaces used to craft wave fronts closely follow from the intended function the optical element is to perform. Active optical elements, then, naturally carry out their task by reshaping themselves according to the changing requirements they have to fulfill in different situations. The lens of the human eye, e.g., increases its curvature when adapting from looking at a distant object to one close by. Similarly, deformable mirrors used in astronomy reconfigure their surface to compensate for wave front distortions stemming from atmospheric disturbances. However, with the advent of metasurfaces - artificial subwavelength thickness materials- and moreover the formulation of a generalized Snell's law [122, 123], form has detached from function. A metasurface lens [124-130] can be completely flat, yet impart a spatially varying phase profile through abrupt phase jumps and thus shape the wave

front of a transmitted light wave. Therefore, optical elements utilizing active metasurfaces can accomplish varying functions exploring entirely different approaches that are geometrically static. This is a key advantage of metasurface based optical components [131, 132], since it is undesirable to utilize mechanical actuation in highly-integrated nanophotonic components. A field closely linked to metasurfaces is plasmonics, the study of light interaction with free electrons in a metal, which has already realized active designs that do not rely on mechanical deformation. Moreover, various material systems ranging from graphene to magnesium hydride (Section 2.3) as well as the phase change material GeSbTe (GST) [A3, 110, O1, 133] have been successfully employed to achieve active plasmonics. In particular, GST has also been used on its own to demonstrate reconfigurable amplitude masks for compact optical components [134].

In this chapter, we present a novel approach for the design of active plasmonic nanophotonic components that combines metasurfaces with the low-loss phase-change material (PCM) $\text{Ge}_3\text{Sb}_2\text{Te}_6$ (GST-326) introduced in Section 2.3. In particular, we make use of the large contrast of the optical dielectric constant when switching from the amorphous ($n_a 3.5 + 0.001i$) to the crystalline phase ($n_c 6.5 + 0.06i$) at $3.1 \mu\text{m}$. In our proof-of-concept demonstration, two different sets of plasmonic antenna elements A and B provide distinct functionalities, e.g., beam refraction to opposite directions, but are spatially staggered within one light interaction area on top of a GST layer (Fig. 3.1a).

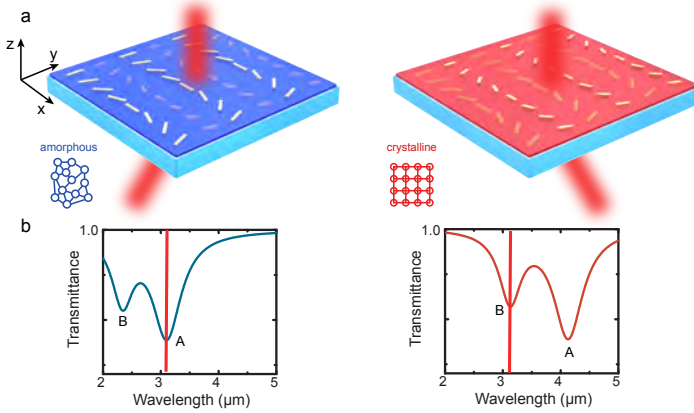


FIGURE 3.1. Active plasmonic metasurface for beam steering. The active metasurface consists of a 50 nm thick GST-326 layer underneath a geometric phase metasurface for beam steering. Two types of nano-antennas A and B with different plasmon resonances are alternated line-wise. a) When the active layer is in the amorphous phase, only type A rods interact with the incident light at 3.1 μm wavelength and deviate the beam (left). When the active layer is in the crystalline phase, only type B rods interact with the incident light and deviate the beam into the opposite direction due to their relative orientation (right). b) Schematic depiction of transmittance of active metasurface in the amorphous (left) and crystalline (right) state.

Depending on the state of the phase-change material, one can select which set of plasmonic antennas strongly interacts with the incident light at a certain operating wavelength. This is achieved by choosing appropriate lengths for A and B type antennas such that their respective plasmon resonance wavelengths match the operating wavelength either in the amorphous or crystalline PCM state (Fig. 3.1b). Therefore, switching the PCM selectively “activates” a subset of metasurface elements. The concept of staggering different designs into one layout crucially hinges on the inherent local surface plasmon resonance property of exhibiting extinction cross-sections at resonance that are much larger than the geometrical footprints of the individual antenna elements. This allows for elements to be spaced relatively far apart from one another while retaining an effectively continuously

covered surface from a light interaction view point. The only limiting factor in designing staggered metasurfaces lies in avoiding propagating surface modes such as Rayleigh anomalies stemming from a periodic arrangement of plasmonic antenna elements with certain periodicities that might introduce undesired loss channels.

3.1 BEAM-STEERING

First, we demonstrate the principle for constructing bi-functional active plasmonic devices employing a plasmonic beam-steering metasurface that refracts an incident beam in opposite directions depending on the phase of the active PCM layer. We utilize a dispersionless geometric phase approach [135] to design abrupt phase jumps Φ at the metasurface where the relative rotation angle of a nanorod antenna is directly related to the phase that is picked up by the cross-converted fraction of incident circularly polarized light (CPL). The cross-converted field scattered by the antennas arises from the dipole moment p that is induced by an incident electric field, which impinges on a dipole that forms an angle with the x -axis in the x - y plane as follows:

$$p_{L(R)} = \frac{1}{\sqrt{2}}\alpha \left(e_{L(R)} \pm e^{\pm i2\phi} e_{L(R)} \right) \quad (3.1)$$

where α is the electronic polarizability, the subscripts R and L denote right- and left-handed circularly polarized light, respectively, and $e_{L(R)}$ are the unit vectors for left- and right-handed circularly polarized light. The sign in the exponent depends on the combination incidence/transmission and is + for LCP/RCP and - for RCP/LCP. Thus, a continuously full 0 to 2π range of abrupt phase jumps $\Phi = 2\phi$ can be realized by rotating the electric dipole, i.e., a plasmonic nanorod antenna, in the x - y plane from 0 to π [135]. Therefore, arranging m nanorods equally spaced over a superperiod Λ with relative rotation angles of π/m in between adjacent elements yields a constant phase gradient $d\Phi/dx$. The generalized Snell's law for the converted circularly polarized light is then [122]

$$n_t \sin \theta_t - n_i \sin \theta_i = \pm \frac{\lambda_0}{\pi} \frac{d\phi}{dx} = \pm \frac{\lambda_0}{\Lambda} \quad (3.2)$$

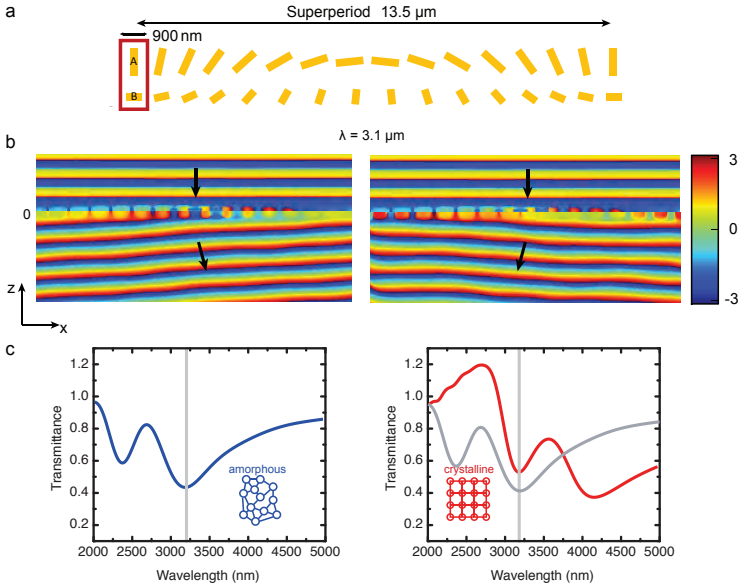


FIGURE 3.2. Working principle for active beam steering metasurface. a) The fundamental building block consists of two rows of differently sized nano-antenna elements A and B. Antennas A are longer and resonant at $3.1 \mu\text{m}$ for an amorphous GST substrate. The antennas are arranged such that each consecutive antenna, going from the left to the right, is clock-wise rotated by 12° with respect to the previous antenna. Antennas B are shorter and resonant at $3.1 \mu\text{m}$ for a crystalline GST substrate. They are arranged in counter-clockwise rotation. b) Phase plots of the cross-converted scattered field (LCP) from full-field simulations with RCP light impinging. Depending on the state of the GST substrate, the beam is deviated into different directions. c) Simulated transmittance of beam steering metasurface for a-GST and c-GST.

Using this principle, we construct the unit cell of the beam-steering active plasmonic metasurface to consist of two rows of $m = 15$ antennas A and B with lengths $l_A = 600 \text{ nm}$ and $l_B = 370 \text{ nm}$, thicknesses $t_A = t_B = 40 \text{ nm}$, and widths $w_A = w_B = 50 \text{ nm}$. The antennas are made of gold and are equally spaced in x-direction with periodicity $p = 900 \text{ nm}$, and distance between rows A and B as $d = 550 \text{ nm}$

(Fig. 3.2a). This results in plasmon resonances at $\lambda_0 = 3.1 \mu\text{m}$ for antennas A on an a-GST layer and antennas B on a c-GST layer. The superperiod Λ is $13.5 \mu\text{m}$, which yields a refraction angle of $\theta_t = 13.28^\circ$, depending on the helicity of the incident light. The nanorods in the upper row are rotated clockwise going from left to right whereas those in the lower row are rotated anti-clockwise leading to opposite refraction angles for the same helicity of incident circularly polarized light. Full-field finite-difference time-domain simulations were carried out for the unit cell with periodic boundary conditions in x - and y -directions. The metasurface is located at $z = 0$ and illuminated from the top at normal incidence with RCP light. The resulting phase profile of a cut through the $x - z$ -plane demonstrates the refraction to opposite angles for cross-converted light (LCP) a-GST and c-GST (Fig. 3.2b). The normalized transmittance spectra reveal that antennas A are resonant around $3.1 \mu\text{m}$ in the a-GST case, whereas antennas B's resonance shifts to this spectral position in the c-GST case. Note, that the transmittance values above a value of 1 are due to the excitation of grating modes, which leads to more light being funnelled through the same interaction area with respect to the background area used for normalization. The state of the phase change material thus selects whether antenna set A or B interacts with the incident light.

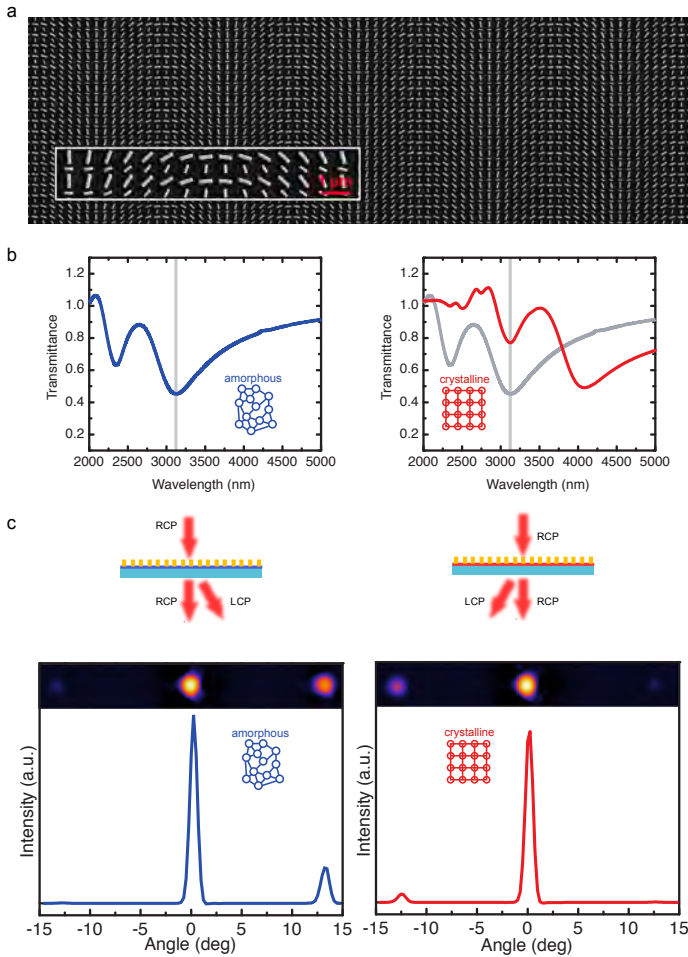


FIGURE 3.3. Experimental realization of beam steering metasurface. a) SEM micrograph of the beam steering metasurface fabricated by electron-beam lithography. b) Transmittance for the fabricated metasurface in amorphous (left) and crystalline (right) state. c) Infrared camera images and intensity plots of the beam transmitted by the active metasurface in the amorphous (left) and crystalline (right) state. As designed, the deviated beam switches to the opposite side of the main beam when switching the phase change material.

We fabricated the design using electron beam lithography over an area of $600\ \mu\text{m} \times 600\ \mu\text{m}$ to define the plasmonic gold nanorods. As substrate, we used CaF_2 with a 50 nm thick layer of GST-326 followed by a 15 nm thick $\text{ZnS} : \text{SiO}_2$ capping layer to prevent oxidation. A scanning electron micrograph of the resulting metasurface is shown in Fig. 3.3a. To verify the switching behaviour of the active metasurface fabricated, we carried out Fourier transform infrared (FTIR) spectroscopy measurements using a Bruker Vertex 80 coupled to a microscope (cf. Section 2.4.1). As designed, the plasmon resonance of the longer nanorods A lies at $3.15\ \mu\text{m}$ for a-GST whereas the shorter nanorods B exhibit a resonance at $2.28\ \mu\text{m}$. After inducing crystallization by heating the sample on a hot plate for 2 min at 180° , the plasmon resonance associated with nanorod set B is shifted to $3.15\ \mu\text{m}$, which excellently coincides with the resonance position of antenna set A in the a-GST case. Simultaneously, the plasmon resonance of antenna set A is shifted out of the region of interest to $4.1\ \mu\text{m}$. In both the amorphous and crystalline states, the sample was characterized at $3.15\ \mu\text{m}$ wavelength using an in-house optical parametric master oscillator power amplifier (MOPA) system [136] that outputs linearly polarized light (Details in the Supporting Information). We further inserted a quarter-waveplate before the sample to generate circularly polarized light and recorded the resulting far field image with a pyroelectric array camera (Pyrocam III, Ophir Photonics). The resulting images for RCP illumination are shown in Fig. 3.3c. When the GST is in its amorphous state, antenna set A interacts with the incident light and refracts the cross converted portion of the incoming beam (LCP) to the right side of the nonconverted RCP part, which is subjected to the conventional Snell's law and therefore does not change its propagation direction. The measured deviation angle is 13.23° , in good agreement with the theoretical value of 13.28° , which can be obtained using . For crystalline GST, the incident beam interacts with antenna set B, thus, the converted portion is refracted to the opposite direction. The relative intensity of the anomalously refracted beam in the c-GST case is lower than in the a-GST case because the scattering of the plasmon resonance of antenna set B is weaker as can be seen in Fig. 3.3b. This is due to the fact that the dipole strength of the shorter nanorods used for antenna set B is weaker, which is further reduced by the higher real and imaginary parts of the refractive index

of c-GST. One can partially counteract this decrease in plasmon resonance amplitude by using thicker and longer nanorods for antenna set B or using two rows for each single row of antenna set A or by developing even less lossy PCMs. The measured relative efficiency, given by the intensity ratio of the anomalously refracted beam to the incident beam, is approximately 5% in accordance with previously reported values [135].

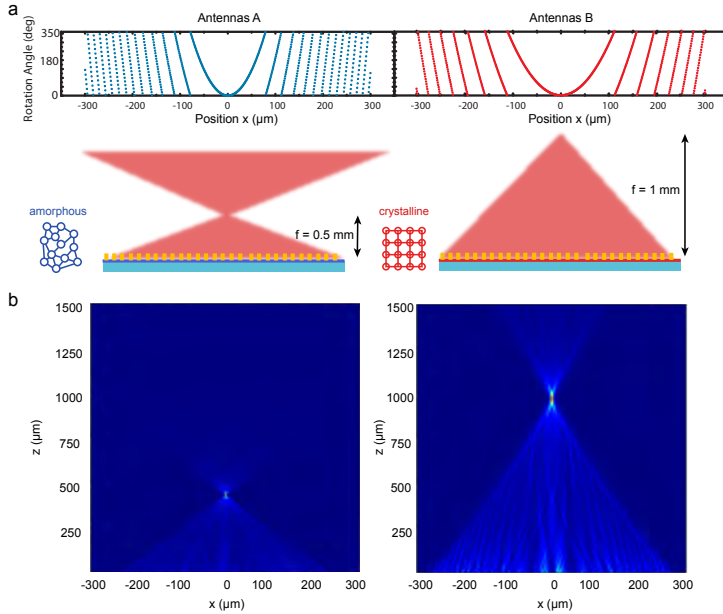


FIGURE 3.4. Working principle of cylindrical varifocal zoom lens. As for the beam-steering metasurface, antennas A and B are line-wise alternated on a GST substrate, which yields a cylindrical lens with varying focus depending on the type of antenna, which interacts with the incident light. a) Rotation angle versus x -position for antenna type A (left) and B (right). These distributions give rise to a focus at $z = 0.5$ mm for amorphous GST and $z = 1$ mm for crystalline GST. b) Full-field simulation of field intensities arising in the amorphous (left) and crystalline (right) cases. As designed, the focus lies at $z = 0.5$ mm in the amorphous case and $z = 1$ mm in the crystalline case.

3.2 VARIFOCAL LENSING

As a second practical example, we demonstrate a varifocal cylindrical plasmonic metasurface zoom lens. The required spatial phase profile with the corresponding rotation angles (Fig. 3.4a) for nanorods in antenna sets A and B are calculated over an area of $600\ \mu\text{m}$ using the formula for diffractive cylindrical lenses [129, 137]

$$\phi(x) = 0.5k_0 \left(\sqrt{(f^2 + x^2)} - |f| \right) \quad (3.3)$$

where ϕ denotes the rotation angle, f the focal length, k_0 the free space wavevector and x the associated x -position of the nanorod. In particular, we use focal lengths $f_A = 0.5\ \text{mm}$ for antenna set A and $f_B = 1\ \text{mm}$ for antenna set B, i.e., for amorphous GST, the focus will lie at $0.5\ \text{mm}$ and for crystalline GST at $1\ \text{mm}$. The incident polarization is RCP such that the metalens will operate as converging lens [129]. The periodicity is kept at $900\ \text{nm}$ in x -direction and $110\ \text{nm}$ in y -direction with a center-to-center distance between antenna sets A and B at $550\ \text{nm}$.

We carried out full-field simulations over a $650\ \mu\text{m}$ simulation domain with perfectly-matched layers as boundaries and incident RCP plane-wave illumination at $3.15\ \mu\text{m}$ to verify the performance of our design (Fig. 3.4b). The plots of the converted field intensities (LCP) reveal that indeed focusing occurs in both the amorphous and crystalline case at the chosen z -positions. We fabricated the design using the same procedure as before (see Methods, SEM micrograph in Fig. 3.5b) and characterized the sample at $3.15\ \mu\text{m}$ wavelength with our MOPA source. Using a quarter waveplate before the active metalens, we generate RCP from the linearly polarized MOPA output and subsequently filter with an identical quarter waveplate and a linear polarizer for converted LCP light. Using a microscope with $20\times$ magnification, we image different $z = \text{const.}$ planes, revealing the beam shape at different distances from the varifocal plasmonic zoom lens (Fig. 3.5). The resulting images for the sample plane and $z = 0.5$ and $1\ \text{mm}$ -distances are shown in Fig. 3.6. When the GST is in the amorphous state, as before, only antenna set A interacts with the incoming light, thus imprinting the phase profile that creates a focus at $z = 0.5\ \text{mm}$, which leads to a bright line focus at this distance. After

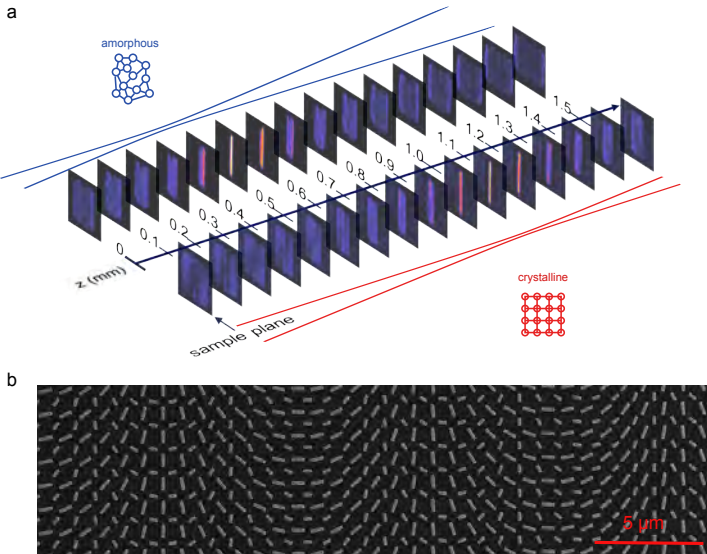


FIGURE 3.5. Experimental realization of the cylindrical varifocal lens. a) Camera pictures of the cylindrical varifocal zoom lens imaged at different distances z from the metasurface. Since the design is for a cylindrical lens, only the x -direction is focused. In the amorphous case, a bright line appears at $z = 0.5$ mm, whereas the image shows broad diffuse lightness at the same z position in the crystalline case. At $z = 1$ mm the bright line focus appears in the crystalline case whereas one can only observe a light patch in the amorphous case. This is in very good agreement with the theory. b) SEM micrograph of a portion of the fabricated cylindrical metasurface lens.

inducing a phase change to the crystalline state, as designed, antenna set B defines the functionality of the metalens. This manifests as a focal line that becomes visible at $z = 1$ mm.

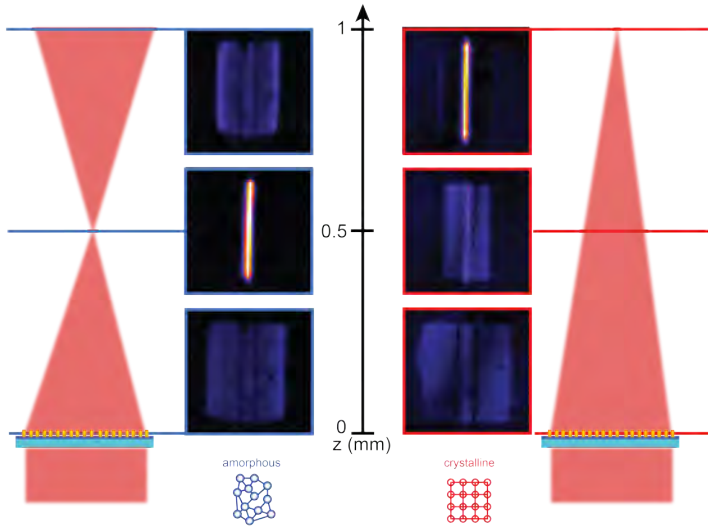


FIGURE 3.6. Infrared camera images at $z = 0, 0.5$ and 1 mm. It can be clearly seen that the focus shifts from 0.5 mm in the amorphous case to 1 mm in the crystalline case.

CONCLUSION

In conclusion, we have presented a novel approach for designing active compact nanophotonic devices and experimentally demonstrated the feasibility at the example of an active plasmonic beam steering metasurface and a varifocal zoom metalens. The method proposed has the benefit that it is highly-integrated in a layered fashion without relying on any mechanical motion or reconfiguration. While we chose to restrict ourselves to interweaving only two functionalities per sample, it is also possible to utilize more sets of nanorods with distinct resonances. The GST layer can be partly switched to generate intermediate refractive indices that select for the different antenna sets whereby each of these states would be metastable by themselves [138]. The limiting factor lies therein that more antenna sets would equal less area

coverage per antenna set and therefore a weaker individual performance. However, since the functionality is only imprinted on the converted part of the beam, one can easily filter out any light that passes through the metasurface without interacting. Furthermore, a whole range of PCMs exists that all have unique optical properties [112] such that an additional design parameter is readily available through the choice of a particular PCM. One is not restricted to combining similar functionalities into one active metasurface: one can easily “mix-and-match” entirely different optical components in one active metasurface and thus create highly-integrated multi-purpose nanophotonic components. Furthermore, while our demonstration relies on one-directional hot-plate induced phase change, it is well-known that GST can be reversibly electrically and optically switched on ultrafast time-scales [105, 106, 109]. Overall, the approach presented creates an exciting new design principle that can be explored in many directions ranging from on-demand nanophotonic components, such as novel scanners combining beam steering and lensing, to dynamic phased-array optics for aberration correction and active holography.

METHODS

Sample Preparation

A 50 nm GST-326 film was DC-magnetron sputter-deposited with a background pressure of 2×10^{-6} mbar and 20 sccm Ar flow followed by sputtering of 15 nm of ZnS : SiO₂. Subsequently, the metasurface was prepared using electron beam lithography employing a polymethylmethacrylate (PMMA) double layer resist, where the first layer is 100 nm 3.5% 200K PMMA and the second layer 100 nm 1.5% 950K PMMA. The resist was baked for 2 min. at 120°C after each layer. After development in 3:1 MIBK:isopropyl alcohol, 2 nm of chromium followed by 40 nm of gold were thermally evaporated and a lift-off was carried out.

Simulation

The simulations were carried out using FDTD Solutions by Lumerical Inc. with periodic boundary conditions and perfectly matched layers for the beam steering and varifocal zoom lens metasurfaces respectively. The metasurface was placed on a CaF_2 substrate with 1.47 refractive index followed by either 50 nm of a- or c-GST respectively (refractive index data from [110]) and 15 nm of $\text{ZnS} : \text{SiO}_2$ with refractive index 2. We used RCP plane wave excitation centered at $3.1 \mu\text{m}$ and evaluated the field intensity of LCP polarized light behind the metasurface.

Part II

CHIRAL PLASMONICS

A BRIEF ACCOUNT OF OPTICAL ACTIVITY AND CHIRALITY

The first observation of natural optical activity was made in 1811 by Arago who noticed changing colors in the image of the sun that formed after having passed through quartz placed between crossed polarizers when the analyzer was rotated [139]. A more detailed description of the phenomenon was later given in a series of mémoires by Biot who could separate the observed effect into the two individually contributing phenomena of optical rotation (rotation of the plane of polarization of linearly polarized light) and optical rotatory dispersion (wavelength dependence of optical rotation)[140–144]. Having observed optical rotation from organic liquids such as turpentine, which contrary to quartz does not exhibit a macroscopic crystal structure, lead Biot to speculate that it possibly originates from an inherent molecular property. In 1824, Fresnel discovered circularly polarized light [145], which subsequently lead to his explanation of optical rotation in terms of different refractive indices of optically active media for right-handed circularly polarized (RCP) and left-handed circularly polarized (LCP) light into which linearly polarized light (LP) light can be decomposed with equal amplitudes [146] (cf. Section 5.1). Following this, in 1848, Pasteur hypothesized that the two asymmetric crystal forms of tartaric acid (Fig. 4.1) are associated with dissymmetric molecules that when dissolved lead to opposite optical rotations. He manually sorted the crystals from a mixture containing both forms under a microscope and redissolved them separately. Indeed, the such obtained solutions exhibited optical rotation of equal magnitude but opposite directions. This firmly established an intimate link between optical rotation and *molecular dissymmetry*, in particular, *chirality*.

Chirality, by Lord Kelvin's definition [147], is the geometrical property of an object that is not superimposable onto its own mirror image (Fig. 4.1). Therefore, it is a binary property; an object is either chiral or it is not. The two symmetry forms are called *enantiomorphs* and in the case of molecules *enantiomers*.

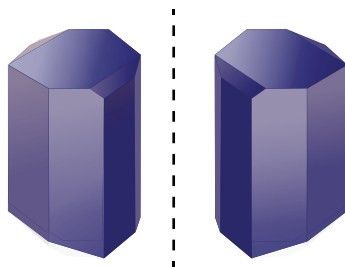


FIGURE 4.1. The two enantiomorphs of tartaric acid crystals.

Uncovering the connection between optical activity and chirality sparked the development of stereochemistry since it inevitably implied three-dimensional molecular structures. In 1874 van 't Hoff and Le Bel explained optical activity as the result of an asymmetric tetrahedral arrangement of atoms about a carbon center, a so-called *chiral center*. In this way, optical activity both stimulated the genesis of this new field and provided one of its best analysis tools. For more than a century, its manifestation as circular dichroism (CD), i. e. differential absorption of LCP and RCP light, and optical rotatory dispersion (ORD) in the optical spectra of chiral molecules has been used in applications ranging from the determination of sugar concentration in wine to quality control in pharmaceutically relevant processes [148].

CD-spectroscopy is well-suited for conformational and structural analysis in complex biomolecules such as proteins [149], thereby having revealed secondary and tertiary structures. However, these chiroptical spectroscopy methods only work well for high concentrations of chiral analytes.

Recently, it has been suggested to use plasmonic nanostructures to boost the sensitivity of this method by generating superchiral electromagnetic near-fields [A5, 150–157] or exploiting their acute response to their immediate environment [158–162]. These efforts ultimately hope to boost the limit of detection of chiroptical spectroscopy to the single molecule level as has already been demonstrated for plasmonically-enhanced absorption spectroscopy [163–166]. In Section 8.2, we numerically study the interaction of plasmonic structures

with chiral analytes in detail. However, to this end, it is instructive to also consider the optical modes of chiral plasmonic structures by themselves as we will do in Sections 6.2 and 6.3.

A lot of work has already been done in the field of chiral plasmonics, demonstrating that, indeed, artificially engineered systems can give rise to natural optical activity [22, 167–172]. Furthermore, the associated calculated and measured effects are orders of magnitude larger than in naturally occurring substances, thereby also paving the way for a range of applications such as ultra-thin wave-plates [18, 173] and negative index metamaterials [174–176]. While chiral structures were initially largely fabricated using top-down methods such as electron beam lithography, progress in bottom-up fabrication techniques has enabled DNA-self-assembled chiral plasmonic structures [177–181].

5.1 CHIROPTICAL SPECTROSCOPY

Chiroptical spectroscopy relies on the different interaction of natural or artificial chiral molecules with circularly polarized light (CPL) to gain structural as well as quantitative information. There are a variety of methods that employ microwaves [182], femtosecond pulses [183], photoionization [184], Raman optical activity (ROA) [185], vibrational optical activity (VOA) [186], circular intensity differential scattering [187], circularly polarized luminescence [188] and chiral cavity ring-down spectroscopy [189]. However, ORD and CD are the most widely used ones.

We mathematically describe CPL as introduced in Eq. (2.34). The sign convention employed conforms with the so-called *observer view*, where the tip of the electric field vector rotates clockwise for RCP light when viewed from the observer toward the source.

ORD is the rotation of the polarization plane of linearly polarized light when it passes through a chiral medium (Fig. 5.1 (a)) The rotation angle is proportional to the travelled length and the concentration of chiral molecules. To explain this effect, one can think of LP light as the superposition of equal parts of RCP and LCP light and assume different refractive indices for them, i. e. assume *circular birefringence*. Therefore, one can define a difference in refractive index Δn between RCP and LCP light

$$\Delta n = n_{\text{RCP}} - n_{\text{LCP}}. \quad (5.1)$$

Due to this, a phase difference δ is acquired between the RCP and LCP components, which leads to a polarization plane rotation of

$$\varphi = \frac{\pi d}{\lambda} \Delta n, \quad (5.2)$$

where d is the distance travelled through the chiral medium and λ the wavelength.

CD on the other hand utilizes the differential absorption of CPL (Fig. 5.1 (b)) and is therefore defined as

$$\Delta A = A_{\text{LCP}} - A_{\text{RCP}}, \quad (5.3)$$

where

$$\Delta A = \log_{10} \frac{I_0}{I}, \quad (5.4)$$

with I_0 the input intensity and I the output intensity after the light has passed through the medium.

Since differential absorption results in elliptically polarized light for incident LP light, CD is often reported as *ellipticity*, i. e., the angle of which the tangent is the ratio of the minor to the major axis of an ellipse (Fig. 5.2). The quantity from Eq. (5.3) can be converted to ellipticity via

$$\theta(\text{rad}) = 32.98\Delta A. \quad (5.5)$$

ORD is as a dispersive and CD an absorptive manifestation of the interaction of chiral molecules with light, with typical lineshapes that are shown in Fig. 5.3. As such they are Kramers-Kronig related similarly to how the refractive index is related to the absorption coefficient (cf. Section 2.1.3) [190]:

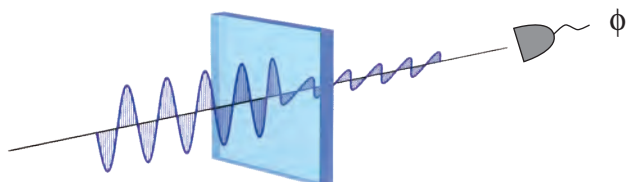
$$\varphi \propto \mathcal{P} \int_0^\infty d\lambda' \frac{\Delta A(\lambda') \lambda'}{\lambda^2 - \lambda'^2}, \quad (5.6)$$

$$\Delta A \propto \mathcal{P} \int_0^\infty d\lambda' \frac{\varphi(\lambda') \lambda'^2}{\lambda^2 - \lambda'^2}. \quad (5.7)$$

Therefore, the information content when measuring either CD or ORD over all spectral features is identical. In practice, this results in the preference for carrying out CD measurements since the absorptive features associated with an electronic transition at wavelength

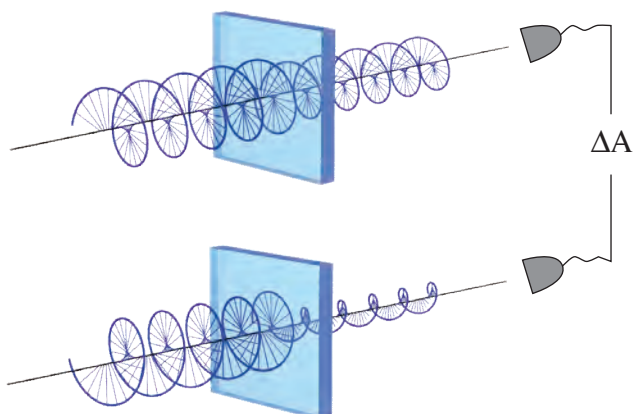
λ_{\max} is more spectrally localized than is the case for ORD, which exhibits a wavelength dependence of $1/(\lambda^2 - \lambda_{\max}^2)$. Note, that λ_{\max} is generally located in the ultraviolet (UV) since this is where optically active electronic transitions occur.

(a)



Optical rotatory dispersion

(b)



Circular dichroism

FIGURE 5.1. (a) Optical rotatory dispersion: linearly polarized light that impinges on a chiral substance rotates its polarization plane proportional to the rotational strength of the substance and the distance travelled. (b) Circular dichroism: the differential absorption of RCP and LCP incident light is recorded.

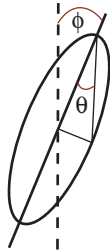


FIGURE 5.2. When linearly polarized light passes through a chiral medium, it both experiences CD, which results in elliptically polarized light for which the measure of deviation from a circle is given by θ , and ORD, which rotates the main axis of the ellipse by an angle ϕ .

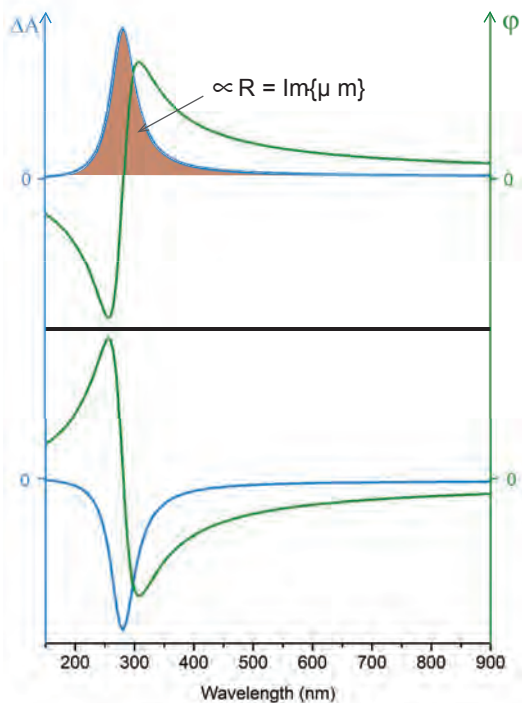


FIGURE 5.3. Typical CD (blue) and ORD (green) spectra. The lineshapes are related in a way that is typical for Kramers-Kronig related quantities. The shaded area is a measure for the rotational strength R , which is given by the Rosenfeld formula.

5.1.1 *Rotational Strength in Circular Dichroism*

Since CD is an absorptive effect, it only occurs where absorption due to electronic, vibrational or rotational transitions takes place. Absorption and CD bands can be readily quantified via their integrated intensities, which are proportional to their *dipole* or *rotational strengths* respectively. These are in turn related to transition dipole moments as follows [185]

$$D = \boldsymbol{\mu}_{ab} \cdot \boldsymbol{\mu}_{ab} \quad (5.8)$$

$$R = \Im m \left\{ \boldsymbol{\mu}_{ab} \cdot \mathbf{m}_{ba} \right\}, \quad (5.9)$$

where $\boldsymbol{\mu}_{ab}$ is the electric and \mathbf{m}_{ab} the magnetic dipole transition moment for electronic transitions between states a and b . The transition dipole moments are defined as [191]:

$$\boldsymbol{\mu}_{ab} = \langle \Psi_b | \hat{\boldsymbol{\mu}} | \Psi_a \rangle \quad (5.10)$$

$$\mathbf{m}_{ba} = \langle \Psi_a | \hat{\mathbf{m}} | \Psi_b \rangle. \quad (5.11)$$

using *Dirac notation* and the electric and magnetic dipole operators $\hat{\boldsymbol{\mu}}$ and $\hat{\mathbf{m}}$ respectively. Equation (5.9) is also known as the *Rosenfeld equation* [192] and can be obtained from a semi-classical second-order time-dependent perturbation theory treatment of the interaction of an incident light field with a molecule [193]. Equation (5.9) is particularly useful for gaining heuristic insight into optical activity. While a dipole transition can be thought of as *linear* displacement of current, a magnetic transition is associated with a *circular* current. Thus, an optically active transition needs to simultaneously exhibit a linear and circular component, which can be thought of as a *helical* charge displacement Fig. 5.4. The handedness of this helix depends on the relative orientations of the linear and circular charge motions. Therefore, it intuitively follows that the interaction of such a transition would interact differently with RCP and LCP incident light.

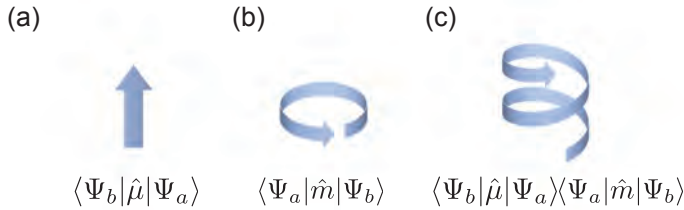


FIGURE 5.4. (a) An electronic dipole transition moment can be thought of as linear charge displacement. (b) Similarly, a magnetic dipole transition moment can be visualized as circular charge displacement. (c) The expression from the Rosenfeld formula differs from zero if a transition exhibits helical charge displacement.

5.1.2 Chiral Plasmonic Split-Ring Resonator

The Rosenfeld formula is very useful in supplying an intuitive understanding and predictive power in assessing which plasmonic structures exhibit optical activity. Figure 5.5 illustrates the chiral plasmonic split-ring resonator (SRR): the regular, flat SRR is well-known as a standard building block of metamaterials [16, 194, 195]. The fundamental mode of this structure can be understood in terms of an electric dipole moment $\boldsymbol{\mu}$ that lies in the plane of the SRR and a magnetic dipole moment \boldsymbol{m} that is induced by the circular current in the SRR loop and points out of plane. Therefore, according to Eq. (5.9), the regular SRR does not exhibit optical activity. However, when one end of the SRR is lifted upward such that we obtain a ramp, the electric and magnetic dipole change their relative orientation and acquire parallel components. This leads to the scalar product $\boldsymbol{\mu} \cdot \boldsymbol{m}$ evaluating to a nonzero value, which in turn is the prerequisite for observing a CD peak. In Section 6.3, we will discuss in detail the mechanism that give rise to the complex CD modes that can be observed for the chiral SRR.

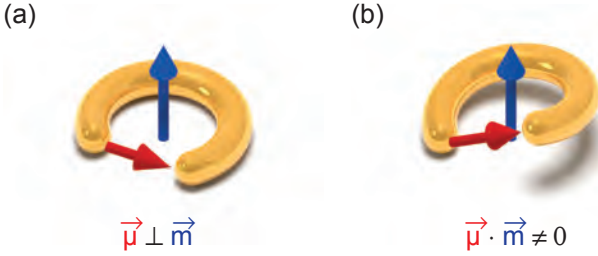


FIGURE 5.5. (a) An electronic dipole transition moment can be thought of as linear charge displacement. (b) Similarly, a magnetic dipole transition moment can be visualized as circular charge displacement. (c) The expression from the Rosenfeld formula differs from zero if a transition exhibits helical charge displacement.

5.2 CHIRAL ELECTRODYNAMICS

While we have discussed the experimental manifestation of chirality in the previous section, here, we give a brief overview of the mathematical framework for the theoretical treatment of chiral media.

5.2.1 Constitutive Equations for Chiral Media

The main difference between linear isotropic media described in Section 2.1 and chiral media lies in the constitutive equations, which for the latter take the form [196]:

$$\mathbf{D} = \epsilon_0 \epsilon \mathbf{E} - (\chi - i\kappa) \mathbf{H} / c, \quad (5.12)$$

$$\mathbf{B} = \mu_0 \mu \mathbf{H} + (\chi + i\kappa) \mathbf{E} / c, \quad (5.13)$$

where electric and magnetic fields are linked through the *Pasteur* or *chirality parameter* κ and the *Tellegen parameter* χ . The chirality parameter is a measure for how strong the associated chiroptical effects are with opposite enantiomers possessing κ values of different signs.

The parameter χ describes materials that exhibit magneto-optic effects. Purely chiral materials are reciprocal and therefore have $\chi = 0$.

5.2.2 Wave Propagation in Chiral Media

Linear isotropic chiral materials obey the homogeneous wave equation [197]:

$$\nabla^2 \mathbf{E} - 2\kappa \frac{i}{c} \partial_t \nabla \cdot \times \mathbf{E} - \frac{n^2 - \kappa^2}{c^2} \partial_t^2 \mathbf{E} = 0, \quad (5.14)$$

$$(5.15)$$

which can be derived from Maxwell's equations Eqs. (2.1) to (2.4) and the chiral constitutive Eqs. (5.12) and (5.13) by evaluating $\nabla \times \nabla \times \mathbf{E}$ and setting $\chi = 0$. This yields two eigenmodes of polarization, i. e., polarization states that are not altered by propagation through the medium. Specifically solving the respective Fresnel equation for propagation in z -direction results in RCP and LCP as eigenmodes with propagation wavenumbers [198]

$$k_{\pm}^2 = \frac{\omega^2}{c^2} (n_{\pm})^2, \quad (5.16)$$

with refractive indices for RCP and LCP

$$n_{\pm} = \bar{n} \pm \kappa. \quad (5.17)$$

The quantity \bar{n} can be thought of as the average refractive index since this is the refractive index that unpolarized light would be subjected to. Due to this birefringent property, chiral media are also referred to as *bi-isotropic* materials, which is a material class that also includes magneto-optical media.

ELECTRON THEORIES OF CHIRALITY AND THEIR
PLASMONIC ANALOGS

In this section, we discuss the mechanisms for the generation of optical activity in complex plasmonic systems. The Rosenfeld equation Eq. (5.9), derived from quantum chemical considerations, reveals the essence of any natural and artificial optically active molecule: oscillating electric and magnetic dipoles are stimulated by an external light wave and mutually interfere inside the molecule. However, quantum chemical calculations require knowledge of the involved wavefunctions, which are often cumbersome to obtain. Therefore, it is often more instructive to consider so-called classical *coupling models* instead, where one studies the interaction of one or more achiral electronic groups with its surrounding or one another [149]. Particularly, they allow for gaining greater physical insight in the case of chiral plasmonics.

Due to the fact that LSPRs can be modelled as harmonic electron oscillators (Section 2.2.3), chiral plasmonic systems are excellent playgrounds for creating and studying prototype structures for the different electronic coupling theories. Electronic theories of optical activity can be broadly divided into two categories: the *static coupling* or *one electron* theory by Condon, Altar and Eyring [199] and the *dynamic coupling* or *coupled electron* models proposed by Born [200] and Oseen [201], and further developed by Kuhn [202], Boys [0], and Kirkwood [203]. The static theory concerns itself with optical activity generated through the interaction of one electron that interacts with an asymmetric electrostatic field while the dynamic theory focuses on the interaction of different achiral components with the electrodynamic fields re-radiated by other groups when excited by an external light field. We start with a qualitative discussion of the omega particle, which is the canonical one-electron system, then discuss the so-called Born-Kuhn system of two vertically displaced orthogonal nanorods and continue with an in depth-analysis of the mode structure of the

chiral SRR introduced in Section 5.1.2 using the insight gained from the Born-Kuhn structure.

6.1 THE OMEGA STRUCTURE AS PLASMONIC ANALOG OF THE CONDON MODEL

Introduction

The first classical theory of optical activity was developed by Drude [204] who suggested helical electron movement as the cause of optical activity. However, it was shown by Born [205] and later Kuhn [206] that Drude's calculations were flawed and did in fact not produce optical activity. Later on, Condon, Altar and Eyring refined Drude's initial idea by considering electron movement in an asymmetric electrostatic potential. Despite the shortcomings of explicitly calculating helical electron oscillations in order to obtain equations for CD and ORD, subsequent works in both antenna theory [207, 208] and chiral plasmonics [18, 170, 209, 210] concerned themselves with helices of different lengths.

Here, we qualitatively discuss the metallic omega particle depicted in Fig. 6.1. The wire part of the omega structure provides good coupling to an external light field, which induces both an oscillating electric and magnetic dipole moment that is supported by the loop. Note, that electric and magnetic dipole moments are parallel to one another, thus, the omega particle should exhibit optical activity following heuristic considerations that result from the Rosenfeld equation Eq. (5.9). The interest of the omega structure lies in the fact that, here, we can isolate the fundamental optical mode contrary to what is the case for many-turn helices. Since we are dealing with a singly-connected structure and only focus on the fundamental mode, we can think of the omega particle as the prototypical example of an one-electron chiral system.

Experiment

We fabricated the omega structure using a commercially available direct laser writing (DLW) system (Nanoscribe) that uses two-photon polymerization to expose three-dimensional structures in a resist. The omegas were written using a 100 \times oil immersion objective lens (NA =

1.4, Zeiss) on top of quartz substrates. Subsequently, the exposed structures were developed in isopropyl alcohol and then chemically plated with silver as described in [211]. The final structure therefore exhibits a core-shell characteristic with the silver coated only on the surface of the omegas while the inside consists of hardened resist Fig. 6.2.

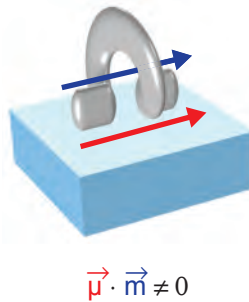


FIGURE 6.1. The chiral plasmonic omega structure consists of a cut-wire and a loop part. While the cut-wire enables good coupling to an external light field and can be thought of as an electric dipole, the loop part provides a circular current that results in a parallel magnetic dipole.

We fabricated periodically arranged right-handed omegas with period $p = 2 \mu\text{m}$ of different loop radii ranging from $r = 300 \text{ nm}$ to $r = 600 \text{ nm}$. As can be seen in Figs. 6.3 and 6.4, the used method reaches its limits for the omegas with radius $r = 300 \text{ nm}$. Figure 6.5 shows the smaller omegas after silver plating. Apart from the desired silver coverage on the particles themselves, the substrate exhibits metal coverage too, which diminishes the overall transmitted intensity in the optical measurements. This can be potentially overcome by selectively functionalizing the substrate before carrying out the writing procedure.

We measured the fabricated right-handed structures using an Fourier transform infrared (FTIR) spectrometer coupled to a microscope as described in Section 2.4.1. Indeed, we observe that at $5.25 \mu\text{m}$ RCP light interacts much more strongly with the omegas than LCP light (Fig. 6.6). Plotting the differential transmission $T_{\text{RCP}} - T_{\text{LCP}}$ reveals a maximum

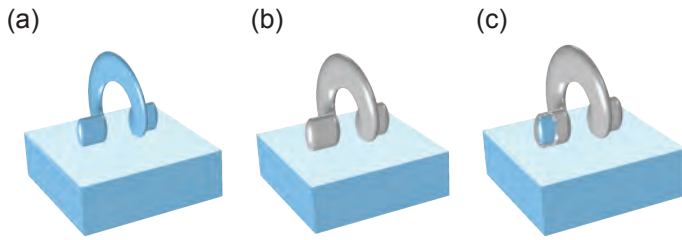


FIGURE 6.2. Schematic of fabrication of omega structures: (a) DLW is used to expose an omega into the resist, which is subsequently developed. (b) The resulting dielectric omega is chemically plated with silver. (c) The final structure is of a core-shell type with a dielectric core and a silver shell.

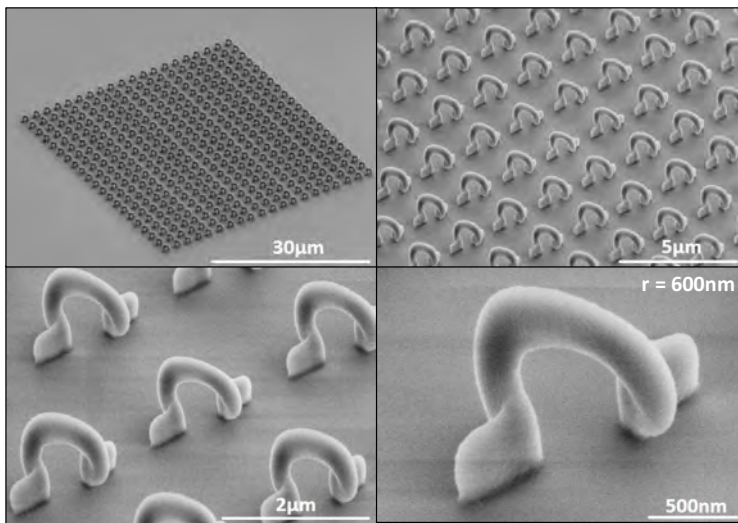


FIGURE 6.3. SEM micrographs of omegas with $r = 600\text{ nm}$ at different magnifications.

difference of 30%. In order to understand the underlying physics, we carried out full field simulations with COMSOL (Section 2.4.1) that

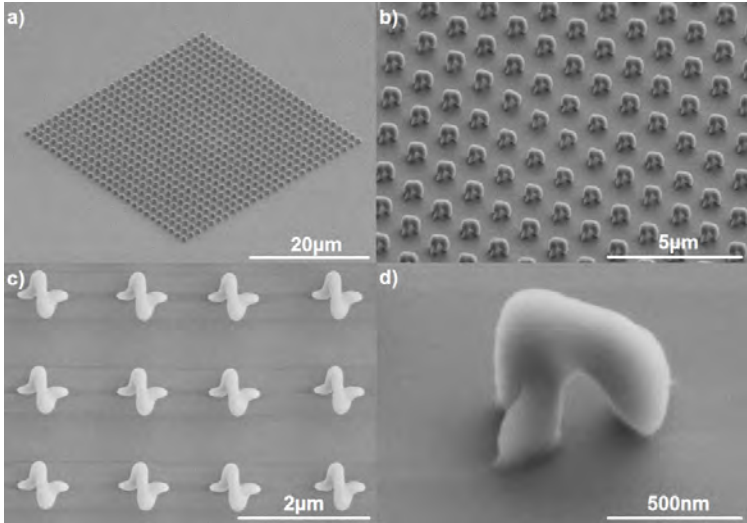


FIGURE 6.4. SEM micrographs of omegas with $r = 300$ nm at different magnifications. Note, that this is close to the fabrication limit of the used procedure, therefore, the loop becomes less well defined as for the $r = 600$ nm case.

agree well with the measured spectra. In particular, we could verify that we are observing the fundamental mode (Fig. 6.6 (Inset)). Interestingly, the curves for RCP and LCP transmission peak at the same wavelength and exhibit the same lineshape. They only differ in their amplitudes showing stronger interaction between the right-handed omega and RCP incident light.

Note, that typically CD spectra are measured from spatially isotropic samples while the omegas we produced are all aligned in the same direction. In order to estimate the contribution of cross-converted light due to elliptical birefringence, we carried out simulations of the cross-polarized transmissions (Fig. 6.7). It can be seen that the contribution of cross-polarized light is negligible, which confirms that our observed differences in RCP and LCP transmission are actually a signature of optical activity.

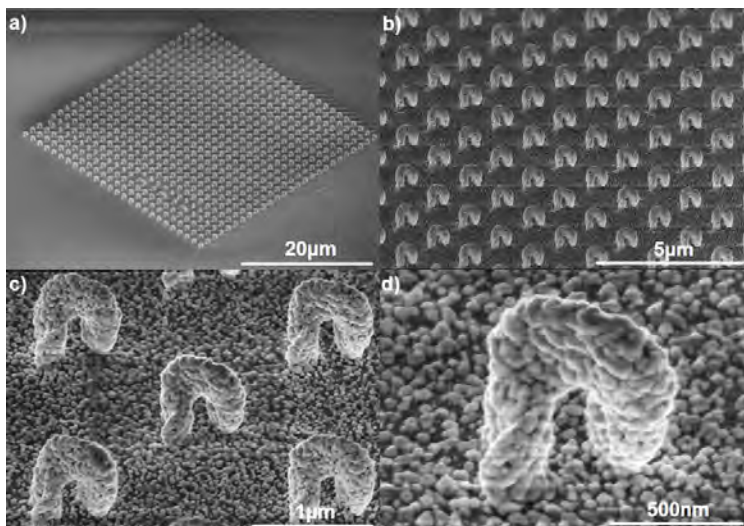


FIGURE 6.5. SEM micrograph of omegas with $r = 300$ nm after plating.

Conclusion

In summary, we were able to fabricate and optically characterize CD from silver-plated omega structures and obtained good agreement with simulated data. In particular, we were able to isolate the contribution of a single fundamental mode to the chiroptical spectrum of a chiral plasmonic structure demonstrating the clean plasmonic analog to the one-electron theory of optical activity.

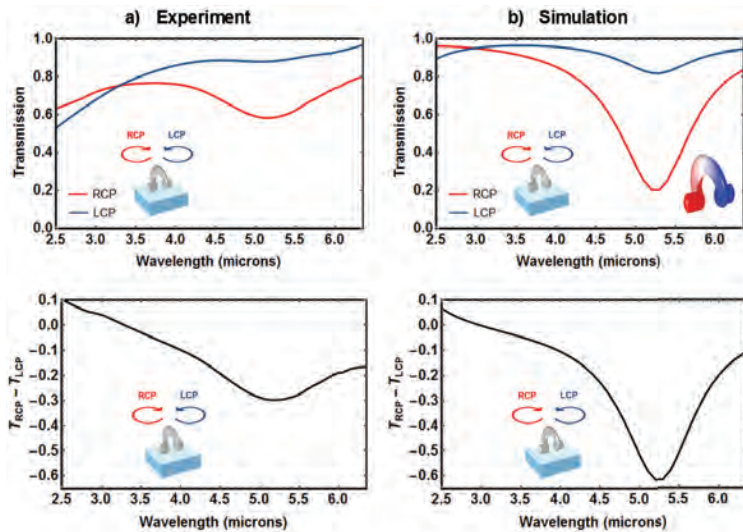


FIGURE 6.6. (a) upper plot: Experimentally measured transmission for LCP (blue) and RCP (red) incident light, lower plot: experimentally measured differential transmittance $T_{RCP} - T_{LCP}$. (b) Corresponding transmission plots obtained from simulation. Inset: Field distribution at 5.25 μm indicating that this is the fundamental mode.

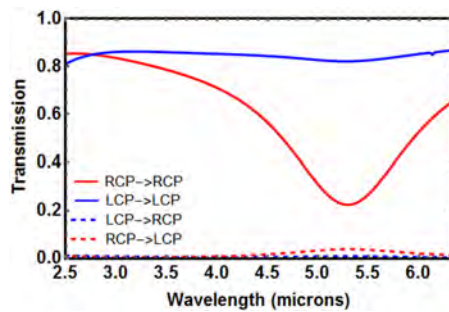


FIGURE 6.7. The transmittance measurements using a circular analyzer confirm that essentially no polarization conversion from RCP to glsLCP and vice versa takes place. Therefore, the transmittance difference measured between incident RCP and LCP light is a good measure for a true chiroptical effect, in this case CD.

6.2 THE CHIRAL DIMER AS PLASMONIC ANALOG OF THE BORN-KUHN MODEL

One of the most intuitive ways to classically understand the generation of natural optical activity in chiral media is provided by the coupled oscillator model of Born and Kuhn consisting of two identical, vertically-displaced, coupled oscillators. We experimentally realize and discuss its exact plasmonic analog in a system of corner-stacked gold nanorods. In particular, we analyze the arising circular dichroism and optical rotatory spectra in terms of hybridized electromagnetic modes and retardation. Specifically, we demonstrate how tuning the vertical distance between the nanorods can lead to a selective excitation of the occurring bonding and antibonding chiral plasmonic modes.

Introduction

In this section, we take a systematic look at the most fundamental chiral plasmonic structure to provide a tool to intuitively dissect, analyze and understand more complex situations. Drawing inspiration from the classical theories of optical activity, we investigate a plasmonic version of the simplest system exhibiting chiroptical responses: two coupled, vertically-displaced electrons of mass m that carry out orthogonal harmonic oscillations driven by an external light field (Fig. 6.8(a)) [200, 212]. The ansatz of using an oscillating charged particle is well-known from the derivation of optical properties of materials within the Drude-Lorentz model. The Born-Kuhn model differs in that it employs two instead of one charged particle and that these are coupled to each other. It is intuitively clear that such a system will lead to polarization rotation for incident linearly-polarized light: Let incident linearly polarized light that is polarized along the x -direction strike the upper oscillator, which is confined to movement in x -direction. The coupling between the two particles will set the second oscillator oriented along the y -direction into movement as well. The resulting direction of the net oscillation will, therefore, differ from the x -direction, thus leading to a polarization rotation. One can immediately see that this describes a chiral system by drawing out the right (D) - and left (L)-handed enantiomers.

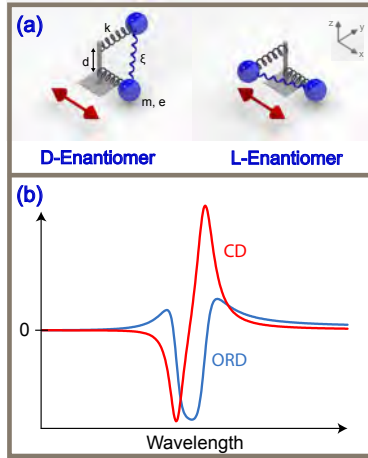


FIGURE 6.8. (a) Right (D)- and left (L)-handed classical coupled-oscillator models of optical activity. (b) Optical rotatory dispersion (ORD) and circular dichroism spectra (CD) calculated from the right-handed coupled-oscillator model.

6.2.1 The Born-Kuhn Oscillator Model

In order to study the value of the rotation and its associated circular dichroism, one needs to determine the resulting complex refractive indices of left- and right-handed circularly polarized light [149]. Consequently, one proceeds analogously to the derivation of permittivity within the Drude-Lorentz model by setting up and solving the equations of motion as treated in Svirko and Zheludev [213] :

$$\ddot{x}(t) + \gamma\dot{x} + \omega_0^2 x(t) + \xi y = -\frac{e}{m} E_x e^{-i\omega t + ik(z_0 + d/2)} + c.c. \quad (6.1a)$$

$$\ddot{y}(t) + \gamma\dot{y} + \omega_0^2 y(t) + \xi x = -\frac{e}{m} E_y e^{-i\omega t + ik(z_0 - d/2)} + c.c., \quad (6.1b)$$

where γ denotes the loss in the oscillators, ω_0 the eigenfrequencies of the uncoupled oscillators, ξ the coupling constant between the two oscillators, m their masses, e their charges, z_0 the position of their center, and d the distance between them. Note the different phase factors of Eq. (6.1a) and Eq. (6.1b) resulting from their different relative positions

on the z -axis. This results in a polarization density for isotropically oriented molecules of

$$\mathbf{P}(\omega, \mathbf{r}) = \varepsilon_0(\varepsilon - 1)\mathbf{E}(\omega, \mathbf{r}) + \varepsilon_0\Gamma\nabla \times \mathbf{E}(\omega, \mathbf{r}) \quad (6.2)$$

where

$$\varepsilon = 1 + \frac{2N_0e^2}{3m} \frac{\omega_0^2 - i\gamma\omega - \omega^2}{(\omega_0^2 - i\gamma\omega - \omega^2)^2 - \xi^2} \quad (6.3a)$$

$$\Gamma = \frac{dN_0e^2}{3m} \frac{\xi}{(\omega_0^2 - i\gamma\omega - \omega^2)^2 - \xi^2}. \quad (6.3b)$$

From Eq. (6.2) and using the relation $\mathbf{D} = \varepsilon_0\mathbf{E} + \mathbf{P}$, we obtain the constitutive equation

$$\mathbf{D}(\omega, \mathbf{r}) = \varepsilon_0\varepsilon\mathbf{E}(\omega, \mathbf{r}) + \varepsilon_0\Gamma\nabla \times \mathbf{E}(\omega, \mathbf{r}), \quad (6.4)$$

which is the Drude-Born-Fedorov form of the constitutive equation for isotropic reciprocal spatially dispersive media introduced in Eq. (5.12) with nonlocality parameter Γ .

In the case of weak chirality, where μ and ε are not modified because of the material chirality, the nonlocality parameter Γ and the Pasteur parameter κ are related through [214]

$$\kappa = \frac{\omega}{c}\Gamma \quad (6.5)$$

which leads to the refractive indices

$$n_{R,L} = \bar{n} \pm \frac{\omega}{c}\Gamma, \quad (6.6)$$

when we use Eq. (5.17).

The associated modes correspond to right-handed and left-handed circularly polarized light described by the ratios $E_x = \mp iE_y$ [215, 216]. The difference between the refractive indices $\Delta n = n_R - n_L$ for RCP and LCP light determines CD and ORD and can be obtained from Eq. (6.6) as

$$\Delta n = 2 \frac{\omega}{c} \Gamma. \quad (6.7)$$

Note that Γ and, therefore, Δn are complex quantities whose real parts are responsible for optical rotatory dispersion (per unit length) through the relation

$$\theta = \frac{k}{2} \Re e (\Delta n) = \frac{\omega^2}{c^2} \Re e (\Gamma). \quad (6.8)$$

Furthermore, the differential absorption of LCP and RCP light is governed by $\Im m (\Delta n)$. Employing Lambert-Beer's law of absorption (per unit length)

$$A_L - A_R = k \Im m (\Delta n) = 2 \frac{\omega^2}{c^2} \Im m (\Gamma), \quad (6.9)$$

yields a CD-spectrum with a typical bisignate shape (Fig. 6.8(b)). Note that CD and ORD are Kramers-Kronig-related as they are derived from the same expression.

The molecular analog of the Born-Kuhn model can be, *e.g.*, found in the two-chromophore coupling of optically active molecules, where each of the chromophores by itself is achiral. A chemical compound that can be described in such a way is 1,1'-bi-2-naphthol (BINOL, Fig. 6.9) [217], which exhibits the characteristic bisignate lineshape in the UV spectral range of its CD-spectrum.

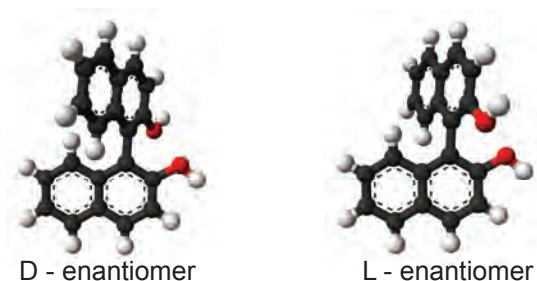


FIGURE 6.9. Left- and right-handed forms of BINOL.

6.2.2 *The Hybridization View for the Plasmonic Case*

The plasmonic version of the Born-Kuhn configuration can be realized as two identical corner-stacked, vertically-displaced nanorods that have a 90° angle between them because the collective excitation of the electron cloud in a nanorod can be well approximated by a harmonic oscillator [31, 80] (Fig. 6.10(a)). The coupling between the plasmonic resonators can be mediated conductively or inductively through near-field coupling. Similar configurations have been evaluated in the literature, however, without a full analysis and discussion of the chiral optical modes [218, 219]. In more complex plasmonic chiral systems, the Born-Kuhn system is oftentimes contained as a subsystem; sometimes even more than once [173, 220–223]. Therefore, understanding its chiral optical modes can help explain more complicated spectra.

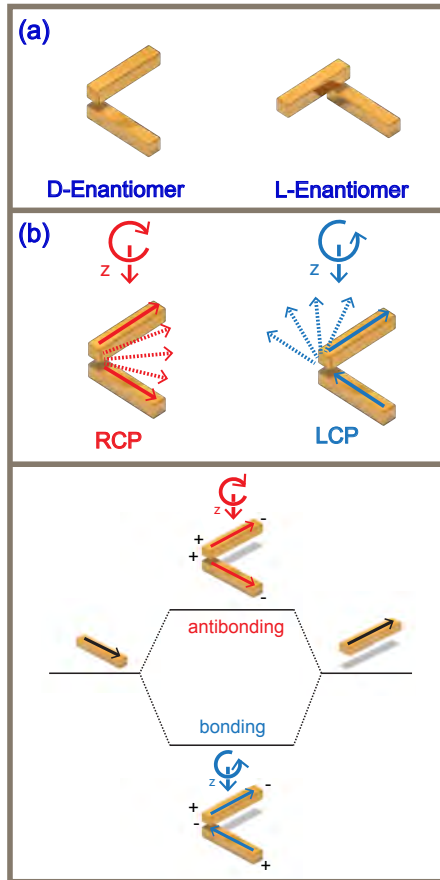


FIGURE 6.10. (a) Left- and right-handed plasmonic realizations of the Born-Kuhn model. (b) Modes excited by right- and left-handed circularly polarized light for the D-enantiomer with rods spaced at an effective quarter-wavelength. (c) Hybridization model for chiral plasmonic Born-Kuhn modes.

This corner-stacked orthogonal nanorods can be thought of as the chiral equivalent to the plasmonic dimer [48, 51, 224]. Therefore, one can easily understand the sign and spectral position of the arising optical modes in terms of a hybridization model. For a qualitative assessment, we assume a vertical spacing d that corresponds to an

effective phase difference of $\pi/2$ between the two nanorods. This stems from the retardation that occurs due to the finite velocity of the electromagnetic perturbation. Given the D-enantiomer, we can study its interaction with right- and left-handed circularly polarized light. Right-handed circularly polarized (RCP) incident light travelling in $-z$ - direction is assumed to have its polarization aligned with the upper nanorod when it strikes it. After having propagated a quarter wavelength, its field vector has rotated clockwise as viewed in $-z$ - direction and will be aligned when it hits the lower nanorod. Therefore, it will drive the electron oscillations in both nanorods in phase. Hence, the symmetry of the light implies the excitation of a mode that corresponds to the antisymmetric case in the coupled oscillator model. This can be thought of as an antibonding mode (Fig. 6.10(c)) as charges of the same sign will accumulate at the ends of the two nanorods. Similarly, left-handed circularly polarized (LCP) incident light first impinges on the upper nanorod, rotates counter-clockwise for a quarter wavelength and then anti-aligns with the lower nanorod. Therefore, due to its inherent symmetry, LCP excites a bonding mode with opposite charges located at the corner where the nanorods are stacked. The resulting energy level for the bonding mode is lower than that of the individual nanorod due to the favorable arrangement of charges whereas the anti-bonding mode lies at higher energies (Fig. 6.10 (c)). Note that due to the choice of the vertical displacement, one obtains a selective excitation of bonding and anti-bonding modes. The reasoning for the L-enantiomer is analogous and leads to swapped bonding and anti-bonding modes.

In contrast to naturally occurring molecules, the plasmonic Born-Kuhn system has the advantage that one can tune various parameters at will, specifically the inter-particle distance. This conveniently allows us to tailor the distance such that we realize the effective $\pi/2$ phase difference assumed above. In nature, the distances between chromophores are much smaller than a quarter wavelength, therefore rendering a selective excitation of the described modes impossible. Also, the nanorods do not have to be corner-stacked in order to show optical activity. For example, a geometry where the nanorods are stacked at their center has been theoretically proposed [225]. However, this setup does not allow for particles that have a 90° angle between them to be chiral.

We carried out finite full-field simulations using a self-written code implementing the Fourier Modal Method with adaptive spatial resolution [118] of the plasmonic Born-Kuhn setup using gold nanorods that have length $l = 223$ nm, height $h = 40$ nm and width $w = 40$ nm. The nanorods are arranged in a C_4 -symmetric supercell [169, 226] in order to avoid anisotropy effects that lead to polarization conversion. These supercells serve as unit cells for our simulations that are periodic with period $p = 800$ nm in x - and y - direction. The excitation is implemented via a plane wave source angled at 17° , which corresponds to the average excitation angle we have in our measurement setup. The whole system is embedded in a dielectric environment with refractive index $n = 1.5$ (corresponding to PC403). By varying the vertical inter- particle distance and monitoring the induced currents and transmission spectra for LCP and RCP light, we found that, indeed, a selective excitation of bonding and anti-bonding modes occurs for $d = 120$ nm as shown in Fig. 6.11. ORD has been calculated by evaluating the orientation of the polarization-ellipse upon illumination with linearly polarized light.

Using these optimized parameters, we realized the plasmonic Born-Kuhn system experimentally using a two-step electron beam lithography procedure [227](Fig. 6.11(c)). The spectra for left-and right-handed circularly polarized light passing through a D-enantiomer are plotted in (Fig. 6.11 (b), upper plot). One can clearly see two Lorentzian curves for the circularly polarized transmittance spectra. As expected from our simple qualitative reasoning, the RCP mode lies at lower wavelengths (1290 nm), *i.e.*, higher energies, therefore, corresponding to a bonding mode. Additionally, the LCP mode is located at longer wavelengths (1325 nm), *i.e.*, lower energies and can be identified as the bonding mode. The measured transmittance spectrum of linearly polarized light is equal the average of LCP and RCP transmittance spectra and its peak is located at 1300 nm. The CD spectrum exhibits the characteristic bisignate lineshape that can be associated with pure Born-Kuhn type systems with extrema appearing at 1250 nm and 1350 nm.

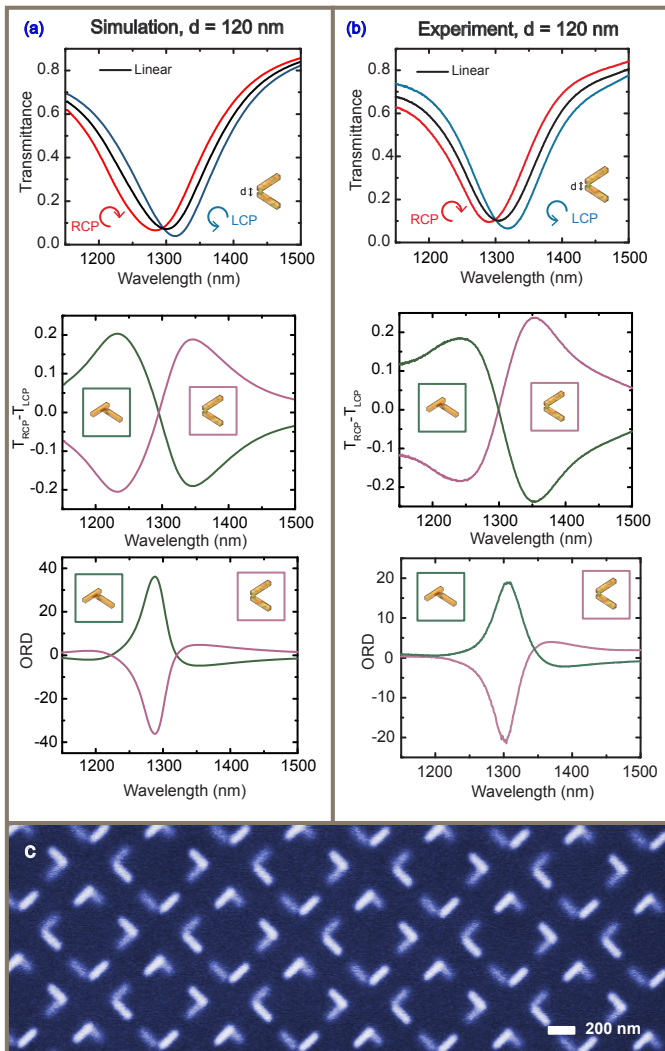


FIGURE 6.11. (a) Full-field simulations of transmittance, circular dichroism (CD) and optical rotatory (ORD) spectra of the C_4 -symmetrically-arranged right-handed enantiomer with 120 nm vertical separation. (b) Measured transmittance, CD and ORD spectra of fabricated structures (c) SEM micrograph of fabricated left-handed enantiomer.

The CD spectra for D- and L-enantiomer are exactly mirror symmetric to each other. It is clear, how the signs of the CD peaks are determined: Evaluating the expression $\Delta T = T_R - T_L$ for the D-enantiomer, one obtains a negative sign of the CD peak at 1250 nm and a positive sign for the peak at 1350 nm with a zero crossing at 1300 nm. Similarly, the L-enantiomer exhibits the opposite behavior due to its switched modes. These properties can be directly predicted by our chiral hybridization model. The fabricated structures show no detectable polarization conversion (S2 in Supporting Information). Additionally, the spectra remain identical when being recorded from the reverse, which is the hallmark of truly bi-isotropic, *i.e.*, chiral systems because it means that the structures are time reversal symmetric (Fig. 6.12). The ORD curves for D- and L-enantiomers follow the lineshape of the Kramers-Kronig-related curve of the CD spectrum with a maximum rotation angle of 20° at 1300 nm.

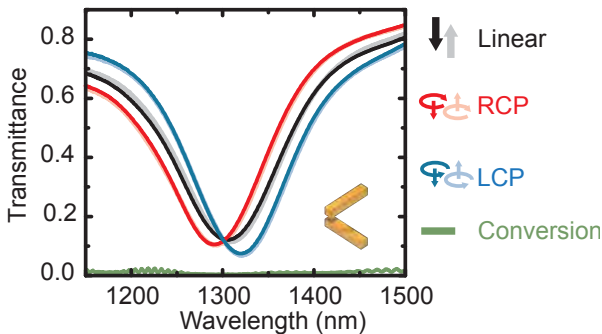


FIGURE 6.12. The recorded transmission spectra for linearly, right-handed circularly and left-handed circularly polarized light are identical regardless of propagation direction. This implies that the structure is time reversal symmetric. Furthermore, the conversion between different circular polarizations is negligible, meaning there's no superimposed linear dichroism stemming from anisotropies. Therefore, the corner-stacked rods in C_4 -symmetry are a truly bi-isotropic, *i.e.*, a truly chiral system.

We simulated and prepared a second sample with an interlayer distance of $d = 60$ nm, whose spectra can be seen in (Fig. 6.13). Here,

the transmittance spectra for RCP and LCP do not follow a single Lorentzian lineshape anymore. Moreover, one can see that RCP light not only excites the higher energy anti-bonding mode but also the lower energy bonding mode. However, the anti-bonding mode is still excited with much greater efficiency due to its preferred symmetry for RCP light. Likewise, the anti-bonding mode is also excited with small efficiency by LCP light. This behavior, again, can be explained with our simple qualitative model. At distances d shorter than an effective quarter wavelength between the two nanorods, the polarization vector of the light does not fully align with the lower nanorod. Therefore, it also possesses a component of its electric field vector that can drive the mode of opposite symmetry to the preferred one. In principle, one could use this effect and tune the distance d to $3\pi/4$ phase difference and flip the sign of the CD and ORD responses. In practice, this cannot be achieved because the near-field coupling vanishes [228]. The anti-bonding and bonding modes are spectrally more separated due to the stronger near-field coupling. At the same time, the amplitude of the CD spectrum doubles in comparison to the wider spaced sample. The maximum value $\Delta \ln(T)_{max} = 1.25$ corresponds to an ellipticity of 41250 mdeg ($\theta \text{ (mdeg)} \approx 33000 \cdot \Delta A$) [185]. This value can become even larger for smaller interlayer separations. Compared to the perfectly-spaced sample, the ORD spectrum in Fig. 6.13 is broader because the two modes that contribute to it are separated further. Interestingly, the linear transmittance spectrum shows around 40% transmission in the region between 1250 nm and 1400 nm. Thus, the thin layer containing the stacked nanoparticles operates as a broadband waveplate in this region. This is a property that one can easily play with by changing the structure parameters, thereby, conveniently achieving high rotation angles. Note that while we chose an inductively-coupled system for our demonstration, the same reasoning holds when the two nanorods are conductively coupled to each other via a gold connection. In this case, the bonding mode would red-shift further.

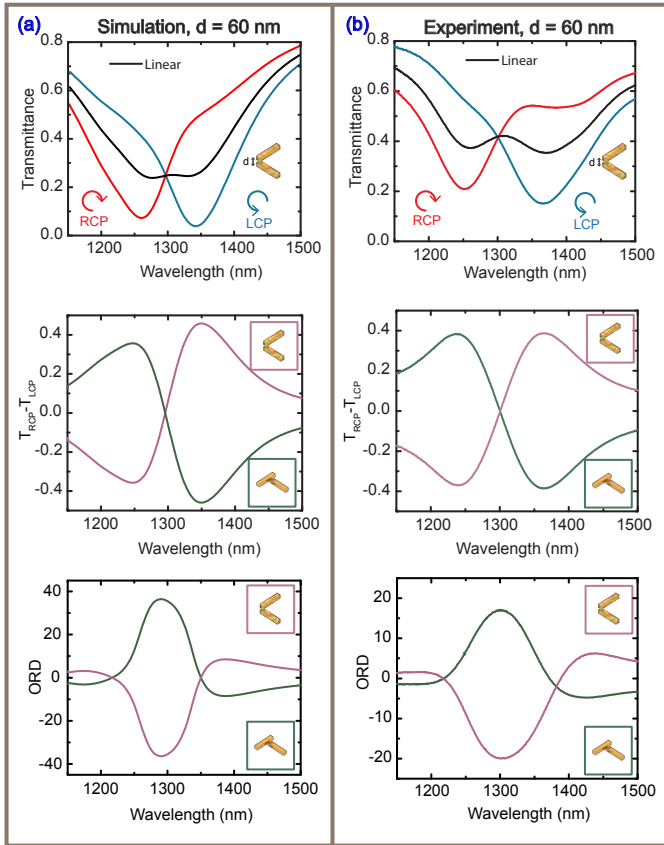


FIGURE 6.13. (a) Full-field simulations of transmittance, CD and ORD spectra of the C_4 -symmetrically-arranged right-handed enantiomer with 60 nm vertical separation. (b) Measured transmittance, CD and ORD spectra of fabricated structures.

To demonstrate the accuracy with which the coupled-oscillator model describes the plasmonic Born-Kuhn model, we carried out a

fit of the CD-spectrum of the left-handed enantiomer with 60 nm vertical spacing (Fig. 6.14(a)) using the analytic fitting formula:

$$\ln(T_R) - \ln(T_L) = \frac{1}{\omega^2} \Im m \left(\frac{A\xi\omega^2}{(\omega_0^2 - i\gamma\omega - \omega^2)^2 - \xi^2} \right), \quad (6.10)$$

where the amplitude coefficient A , ω_0 , γ and ξ were fitting parameters. A phenomenological Drude factor of $1/\omega^2$ was included to account for the bulk gold material properties. The extracted parameters were $\omega_0 = 1450$ THz, $\gamma = 100$ THz and $\xi = 1.84 \times 10^{29} \text{ s}^{-2}$. Inserting the obtained fit parameters into

$$\theta = \frac{1}{\omega^2} \Re e \left(\frac{B\xi\omega}{(\omega_0^2 - i\gamma\omega - \omega^2)^2 - \xi^2} \right), \quad (6.11)$$

where B is an amplitude factor, reproduces the measured ORD spectrum (Fig. 6.14(b)). The discrepancy between analytic fit and measured spectrum is larger for the ORD spectrum than for the CD spectrum because the ORD spectrum depends on the incident angle and we measured under a broad range of angles centered around 17° .

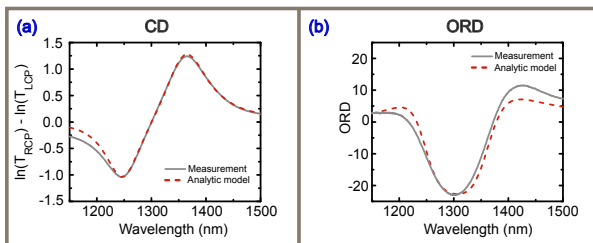


FIGURE 6.14. (a) Measured CD-spectrum (grey) and fit (dashed red) using the analytic Born-Kuhn expression for a left-handed enantiomer with 60 nm vertical separation. (b) Measured ORD-spectrum (grey) and plotted ORD-curve with parameters extracted from fitting of the CD-spectrum (dashed red).

Conclusion

Chirality as a field of study at the intersection of chemistry, life-sciences and physics is truly multidisciplinary. With recent progress in DNA-assisted self-assembly, *e.g.*, and since the amplitude of the CD-signal depends on the angle between the two nanorods [229], one can envision an angle sensitive version of the plasmon ruler concept [61, 226, 230]: a plasmonic angle ruler made of nanorods that are attached to two nanoscopic objects whose relative angle would be encoded in the far-field CD-spectrum of the compound system. In summary, we have shown that a C_4 -symmetric corner-stacked metallic nanorod system acts as the exact plasmonic analog of the Born-Kuhn model of chiral media. Since arbitrarily complex chiral plasmonic systems can often be decomposed into non-parallel rod-type segments, the results of this section provide the required insight to predict their chiroptical spectra. Therefore, our study of the plasmonic Born-Kuhn model will open the door to novel plasmonic designs in a wide range of applications, allowing researchers to specifically tune response, bandwidth, spectral position and size of the chiroptical effect, by intuitively understanding how to couple the basic chiral building blocks together.

6.3 SPIRAL-RAMP STRUCTURES RE-INTERPRETED

Introduction

Using the insight from the Born-Kuhn model, we will apply similar reasoning to explain the mode structure that arises in a plasmonic ramp structure as introduced in Section 5.1.2. While the Rosenfeld formula from Eq. (5.9) predicts the occurrence of optical activity in this structure, it does not directly explain the sign and spectral position of the occurring CD peaks. We use a combination of hole-mask lithography and subsequent tilted angle evaporation to fabricate the chiral gold nanostructures over square centimeters. Hole-mask lithography has already been introduced by the work of Fredriksson [231] and refined by our group. [232, 233] It is a quite flexible and easy method for the fabrication of metallic nanostructures. For structure evaporation, we use our tilted-angle rotation setup, [234–237] which is a modified thermal evaporation machine with flexible sample holder where the hole-mask substrate is mounted. This sample holder can be rotated in θ and ϕ -direction, as indicated in Fig. 6.15(a), utilizing a stepper motor construction. Our home-made stepper motor control software enables precise regulation of the sample movement and position, which is why the evaporation of complex structures is possible.

Experiment

Here, we describe the deposition of left- and right-handed 270° 3D chiral gold structures as sketched in Fig. 6.15. The rotation direction of the sample holder is responsible for the handedness of the structure. It is defined by the sign of rotation velocity, i.e., by the sign of periodic change of the polar angle ϕ . We define a negative sign of the rotation velocity as left-handed rotation and therefore left-handed structures are produced. Throughout this section, we indicate the handedness of our structures by colors, where blue means left-handed and red represents right-handed structures. Due to our geometrical model, we chose a fixed azimuthal angle θ of 22.5° . In order to obtain spiral-like chiral structures, the structure height has to be inhomogeneous.

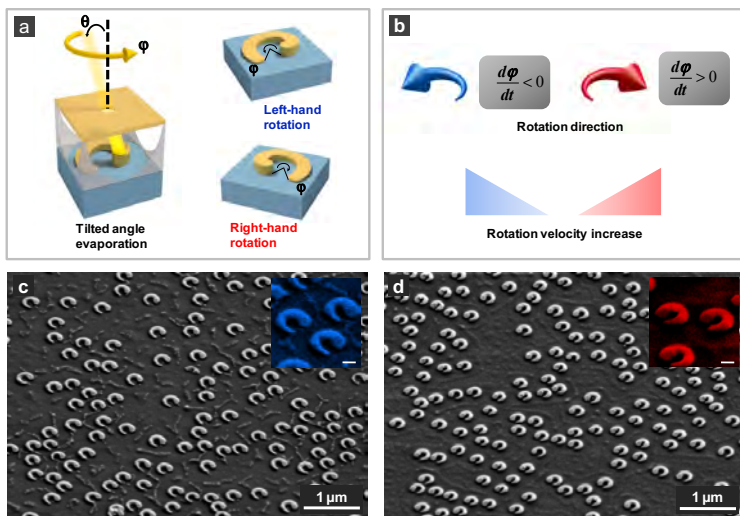


FIGURE 6.15. a) Hole-mask lithography and tilted angle rotation evaporation create 270° left- and right-handed 3D chiral structures over a large area of 1 square centimeter. Blue indicates left-hand rotation, red represents right-hand rotation. b) Rotation parameters during evaporation. The variation of angle φ in the negative direction represents left-handed rotation while the variation in positive direction leads to right-handed rotation of the sample. In order to obtain inhomogeneous structures, rotation velocity has to be accelerated. c) SEM micrograph of left-handed structures. The inset shows a high magnification cutout. d) Image of a right-handed enantiomer sample with high magnification inset. The inset scale-bar is 100 nm.

Therefore, we have to accelerate the rotation speed during metal deposition. In the beginning, the sample holder is rotating quite slowly so that a large amount of material passes through the hole and is deposited on the glass substrate. Subsequently, we slowly increase the rotation velocity, which causes less material to reach the glass substrate and the structure height becomes thinner. With proceeding evaporation, more material is deposited around the hole in the hole-mask, and, therefore, its diameter shrinks. This affects the evaporated structure width. In Fig. 6.15(b), we describe the sample movement

graphically for the evaporation of chiral structures. A final scotch-tape lift-off process removes the poly(methyl methacrylate) (PMMA) mask from the glass substrate. Subsequent immersion into NEP solution for several minutes and oxygen plasma cleaning remove remaining PMMA. scanning electron microscope (SEM) studies illustrate the created chiral gold structures, arbitrarily arranged according to the initial polystyrene (PS)-sphere pattern over a large area of one square centimeter. Figure 6.15 (c) and (d) show typical overview images. The insets illustrate corresponding high magnification cut-outs. In order to determine structure dimensions we estimate the outer diameter and the structure width from averaged measurements over several representative areas taken from different spots on the sample. Our outer structure diameters average to 260 nm and the structure widths shrink from about 90 nm down to roughly 20 nm.

To determine the height profile, we performed AFM-measurements. Figure 6.16 shows a 3D plot of our structures extracted from AFM raw data, depicted in the inset. This confirms the inhomogeneous structure dimensions, which render our structures 3D chiral.

In the following, we discuss the optical spectra of left-handed structures. However, the physical reasoning for right-handed structures is analogous and exactly mirror symmetric. Experimental spectra are depicted in the left column of Fig. 6.17. The right column shows the results of a simple numerical model.

First, we show spectra measured with linearly polarized light in x - and y -direction, plotted in black and grey, respectively. The polarization directions are illustrated in the insets of Fig. 6.17. The transmittance spectra are similar for left- and right-handed structures. To understand the mode pattern, it is helpful to compare our data with the plasmonic resonances of planar SRR structures.^[234] For x -polarized light, two resonances are excited - one at 150 THz the other one at roughly 320 THz. In y -polarization, there is mainly one resonance dip in the transmittance spectrum located at 250 THz. The arrow diagrams in the simulated spectrum (indicating the current distribution for the different modes) of Fig. 6.17 (a) illustrate the character of the resonances. For x -polarized light, the first- and third-order resonances are excited while the second-order resonance mode is excited for the electric field vector polarized in y -direction. Due to a slight asymmetry of the chiral SRR, the third order resonance is only weakly

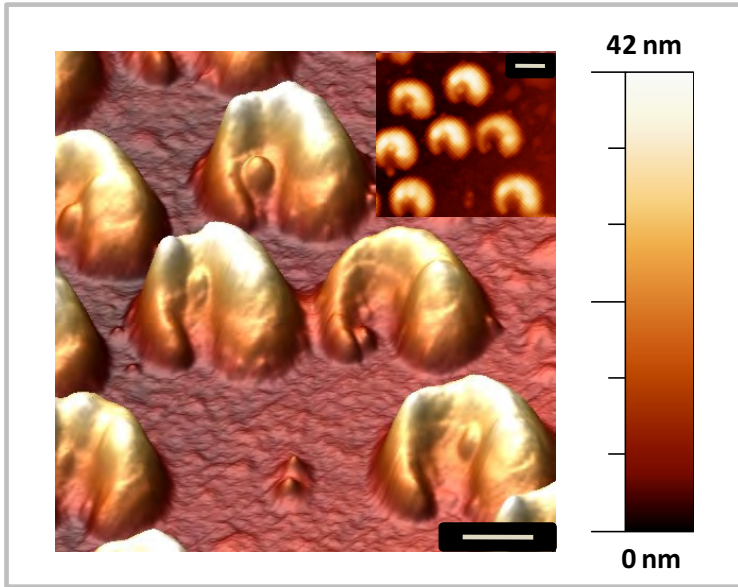


FIGURE 6.16. Shows an overview AFM image, containing a 3D plot and AFM raw data. The irregular structure width and the inhomogeneous structure height make clear that our structures are 3D chiral. The scale bars in the image and in the inset are 200 nm respectively.

excited in experiment and simulation for both x - and y -polarized light. In order to determine the chiroptical properties of the fabricated structures, we study transmittance using circularly polarized light. For these measurements, we insert an infrared quarter wave plate into the light path between polarizer and sample. In Fig. 6.17(b) the light green curve describes the transmission spectrum of our left-handed structure for LCP light and the dark green curve for RCP light. Here we measure in *forward configuration*, which means that the light, which excites the plasmon resonance impinges from the top onto the structures. As expected, there are differences between the spectra measured with LCP- and RCP-light, confirming the chiroptical properties of our structures. All three resonance modes are excited and situated at the same frequency positions for both LCP and RCP, which are the same as for LP incident light. The dashed lines in Fig. 6.17 help to compare

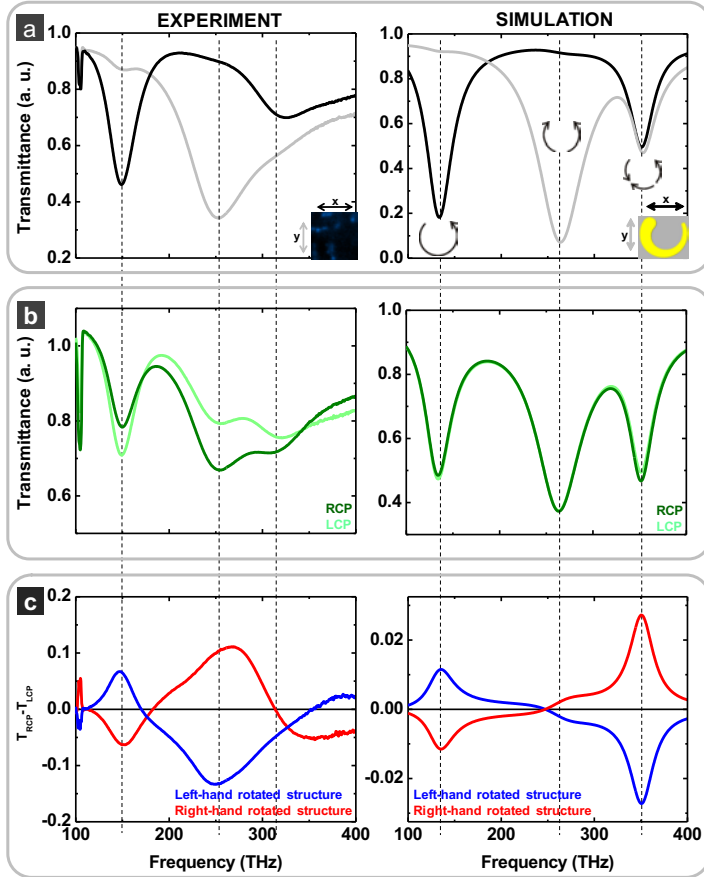


FIGURE 6.17. a) Transmittance spectra for linearly polarized light. For the black curve, the electric field vector is polarized in x-direction, which excites the fundamental and the third order resonance. For polarization in y-direction, the grey curve exhibits the second order resonance. In b) circularly polarized light excites all the three resonances. c) Transmittance differences between left- and right handed circularly polarized light $\Delta T = T_{RCP} - T_{LCP}$ for left- and right-handed structures are shown. There are distinct peaks at the three resonance positions. The second- and third-order-resonance merge to one broader peak for the transmission difference signal.

the resonance positions of all the measured spectra. The resonance at 150 THz is the fundamental mode, and the ones at 250 THz and 320 THz are attributed to the second and third order resonance, respectively. At the fundamental resonance, transmittance for LCP-light is smaller than for RCP-light while for the second- and third-order resonances this behavior is reversed. Our main interest lies in the chiral optical properties of our structures, which manifest as CD. Therefore, we calculate the transmittance difference (ΔT) between RCP- and LCP-light in order to determine the chiral properties of our sample. This is shown in Fig. 6.17(c). Due to our fabrication method, all structures are oriented in the same direction, exhibiting no rotational symmetry of the arrangement. Thus, we expect contributions of polarization conversion to our measured $\Delta T_{RCP-LCP}$ spectra due to elliptic birefringence arising from the bi-axiality of our sample. An overall structure arrangement in C_3 - or C_4 -symmetry would make the sample uniaxial and suitable for CD measurements that are not hampered by polarization conversion. So far we are not able to fabricate structures in a C_4 -symmetric arrangement. However, to obtain the chiral response, we use the calculation introduced in references [238] assuming that the mean value between top and bottom illumination of the transmittance difference between RCP- and LCP-light determines correct chiral ΔT -values. According to this, we have to calculate the $\Delta T_{RCP-LCP}$ spectra using $\Delta T = 0.5 \left(\Delta T_{RCP-LCP}^{top} - \Delta T_{RCP-LCP}^{bottom} \right)$. Therefore, we measure transmittance of our left- and right-handed samples from both illumination directions on the same sample spot in each case. We find qualitative agreement between maximum CD response and the position of the fundamental resonance. At this resonance, the ΔT spectrum exhibits positive values. This changes at roughly 170 THz, so the second- and third order resonances possess a negative sign. The two resonances merge into one broad ΔT resonance, displaying a maximum at 250 THz. We also compare ΔT spectra between left-handed and right-handed chiral structures. The spectrum of right-hand rotated structures is plotted in red in Fig. 6.17 and shows good mirror symmetry when compared with the spectrum of the left-handed structures, which is expected for enantiomers. We also simulate transmittance spectra for LCP- and RCP-light. The right-hand side of Fig. 6.17 shows our model, a circular ramp with increasing

width, which describes the excited mode structure qualitatively and has the same important features as the experiment. The model was optimized to fit the relative positions of the resonances as well as the signs of the respective circular dichroism signals. A more detailed representation of the actual structure geometry and modeling of the non-periodic structure distribution would be necessary to achieve a quantitative description. However, the obtained qualitative agreement is sufficient to gain further insight into the chiral properties of our nanostructures.

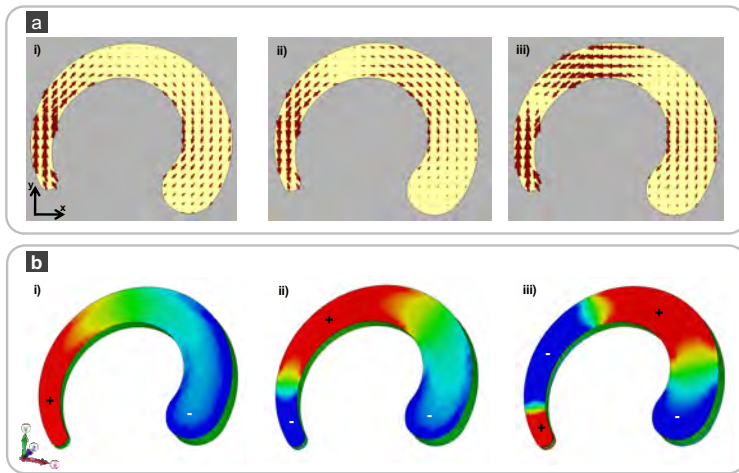


FIGURE 6.18. Resulting a) current and b) z-component of the electric field distributions of the electron oscillations. i) shows the first-order resonance without any node, which results in a dipolar electric field parallel to the structure opening (polarization in x-direction). The second-order resonance with one node in the current oscillation is described in ii). The resulting electric field distribution results in a dipole field perpendicular to the structure gap (polarization in y-direction). In iii) the current-oscillation and the electric field distribution of the third order-resonance are shown, which is also excited for x-polarized light.

6.3.1 *Understanding the Chiral Mode Structure*

In order to describe the origin of the observed resonance modes, we calculate from our simulations the current oscillations and the electric field distributions for each resonance position, as depicted in Fig. 6.18. Here, we only show the modes for excitation with linearly polarized light. Resonances excited by circularly polarized light can be decomposed taking into account $\sigma_{\pm} = x \pm iy$. Due to the asymmetric structure shape, the excited current oscillations and therefore the electric field distributions are asymmetric as well. We show in Fig. 6.18(a) a cross-section through our modeled structure, displaying a snap-shot of the current distributions at each resonance position. In Fig. 6.18 we depict the corresponding z-component of the electric field distribution that arises from the current distribution in Fig. 6.18(a). In column (i), the current flow of the first order resonance at 150 THz is excited by light that is linearly polarized in x-direction and, thus, parallel to the structure gap. Such light excites an electron oscillation within our gold structure that represents the fundamental particle plasmon mode. Fig. 6.18 (b) depicts in image (i) the electric field that arises due to charge separation in the structure. According to the incident polarization, this electric field is oriented in x-direction parallel to the structure gap and forms an oscillating dipole. Column (ii) describes the current oscillation and the electric field distribution for the second order resonance at 250 THz. This resonance is excited by y-polarized light perpendicular to the structure gap. The current oscillation exhibits one node. Hence, a dipolar electric field is oriented in y-direction. In column (iii), the current oscillation and the electric field distribution of the third order resonance at 320 THz are described. The current oscillation of the third order mode has two nodes, corresponding to an electric field with quadrupolar character. In the following, we are going to explain the origin of the chiroptical response of our structures. In Fig. 6.19 we depict the excitation scheme of the above described current oscillations excited by circularly polarized light. The leftmost column illustrates the fundamental mode, the center one the second order mode, and the right column depicts the third order mode.

We use circularly polarized light that propagates towards the structure. In our illustration, we describe the electric field vector by a rotating arrow at several points in time. Circularly polarized light impinges

on the structure and excites the plasmon oscillation, which is denoted as red arrows inside the structure and therefore represents electric dipoles. We discuss this for all resonance positions of our left-handed structures and start with the excitation scheme of the first-order resonance, which is plotted at the left side of Fig. 6.19. Here, LCP-light experiences maximum absorbance, which means that the screw of the circularly polarized light fits the structure's twist. Hence, the light excites the fundamental mode and is absorbed. First, the red arrow marked with number 1 in the light wave starts the electron oscillation at the highest point of the structure. Further propagation of LCP-light along the structure surface up to point 2 leads to progressive excitation of the electron oscillation, and we place another electric dipole parallel to the structure gap. Finally, at point 3 one more electric dipole forms in the structure, which is excited by the electric field vector oscillating in direction 3. In our picture, there are now three electric dipoles aligned in series. For the second- and third-order resonance the opposite polarization, namely RCP-light, is more strongly absorbed. In the center column of Fig. 6.19, the second-order mode is illustrated. The red electric-field vectors marked with 1 and 2 excite electric dipoles 1 and 2 in the structure, while RCP-light circulates along the structure. The dipole arrangement indicates that the second order resonance mode can only be excited due to the round and inhomogeneous shape of our structures. The two dipoles are aligned oppositely. Finally, within the third-order resonance on the right side in Fig. 6.19, there are again three electric dipoles excited, marked by number 1-3. In this case the electric dipoles are facing each other and therefore the oscillation exhibits two nodes. The difference to the fundamental mode is only the orientation of the second dipole. This explains why the third-order mode is excited by light with opposite handedness compared to the fundamental mode. From this, the origin of the circularly polarized transmittance difference in the optical spectra of our 3D chiral structures becomes clear: Excitation of the first order resonance in the left-handed chiral structure with RCP-light leads to less absorbance, because this type of polarized light counter-circulates with respect to the structure's twist. Equivalent reasoning for the second and third order resonances yields a low excitation efficiency for LCP-light, whose handedness does not match with the arrangement of the plasmonic dipoles of the higher order modes in the

twisted structure. Based on this dipole model, we utilize a plasmon hybridization model [48] to clarify the resonance position, which is illustrated at the bottom of Fig. 6.19. The first order resonance possesses the lowest energy configuration because the three dipoles are oriented in series and therefore attract each other. Applying the second order resonance to the hybridization picture, we have to consider opposite dipole alignment. Due to this configuration, the two dipoles repel each other and are therefore settled at a higher energy level. The third order resonance with its two nodes occupies the highest energy level, as the three electric dipoles are antiparallel and therefore repel each other. Note that the fundamental and third order modes can be understood as the bonding and anti-bonding mode of the Born-Kuhn model presented in Section 6.2. Since the currents inside the spiral are conductively rather than inductively coupled as was the case for the chiral dimer, the energy splitting between the two modes is a lot larger.

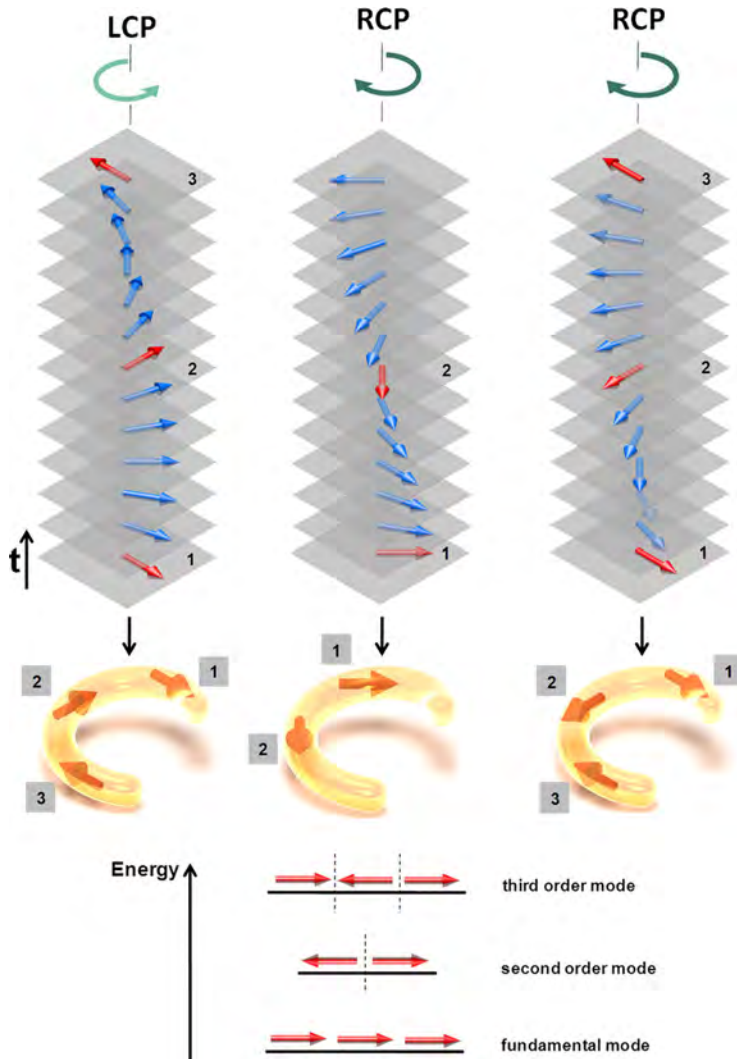


FIGURE 6.19. Formation and character of ΔT peaks in the left-handed chiral plasmonic structure. Circularly polarized light that propagates towards the structure is illustrated by a rotating arrow scheme that represents a dipolar incident electric field vector. This motivates the application of an approximate dipole picture to describe the resonance spectra. The red colored and numbered arrows in the light wave are responsible for plasmon excitation in the fabricated structures. These electron oscillations are also described by arrows in the structure, which result in an electric dipole. Corresponding to the numbers in the structure and in the illustrated light wave, the overall plasmon resonance is excited. This is shown for all the three resonance modes and summarized in a plasmonic hybridization model.

Conclusion

In conclusion, we have demonstrated that colloidal hole-mask lithography in combination with tilted angle rotation evaporation is a quite flexible fabrication method for left- and right-handed 3D chiral plasmonic structures, covering square centimeters of glass substrates. In order to determine their chiral optical response, we have performed FTIR-measurements with circularly polarized light and found significant transmittance differences between RCP- and LCP-light (ΔT). We found ΔT - maxima and - minima at the plasmonic resonance positions, which are mirrored for the two enantiomers. Furthermore, we have applied similar reasoning as introduced in Section 6.2 to explain the interaction between circularly polarized light and the chiral SRR. This clarifies the origin of the positive and negative signs of transmittance mode differences between RCP- and LCP-light and their relation to the geometry of the structure. These structures could find application as substrates for plasmon-enhanced detection schemes of different enantiomers in biomolecular substances with commercial CD-spectrometers.

Methods

Fabrication

First we outline the most important steps of this fabrication technique. We spin-coat a PMMA-layer of approximately 200 nm thickness onto a functionalized glass substrate, which is subsequently covered with a submonolayer of polystyrene (PS) nanospheres of about 100 nm diameter. On top of this system, a gold film of 20 nm is evaporated using an Edwards E 306 thermal evaporator to protect the PMMA from further treatment. After this, the arbitrarily-spread PS particles are removed by a soft ultrasonic bath in water. This yields a gold layer on top of the PMMA substrate including holes of roughly 100 nm diameter. A final isotropic oxygen plasma etching step removes the PMMA through these holes and to some extent underneath the gold layer until the glass substrate is reached. This creates adequate cavities to make space for the evaporation process. The functional principle of our hole masks is the following: in high vacuum, gold is evaporated,

impacts on the mask and passes through the holes. These holes form a gold vapor beam that operates as pencil that writes the sample. A certain tilt angle of the sample in azimuthal direction θ and sample rotation in polar direction ϕ opens the door to the fabrication of a large variety of metal structures in the nanometer size range according to the diameter of the used PS spheres. This is schematically illustrated in Fig. 6.15(a). Due to polydispersity of the PS spheres, the mask is expected to have slightly different hole sizes, and eventually produces slightly inhomogeneous gold structures. AFM measurements are carried out using a Veeco Dimension Icon in combination with NanoAndMore TAP300-AR-G-50 tips for tapping mode in air. AFM analysis is done using the software WSxM.

Simulation parameters

To verify our measurements, we simulate the structure geometry using the frequency domain solver of CST Microwave studio. Due to an inhomogeneous size distribution of our structures, we have to modify the size parameters of our model slightly in order to match the resonance frequency positions. Furthermore, we choose the refractive index of glass $n = 1.5$ and describe the permittivity of bulk gold by a Drude model with plasma frequency $\omega_p = 1.37 \times 10^{16}$ Hz and damping constant $\gamma = 1.2 \times 10^{14}$ Hz.

Active control over the handedness of a chiral metamaterial has the potential to serve as key element for highly integrated polarization engineering approaches, polarization sensitive imaging devices, and stereo display technologies. However, this is hard to achieve as it seemingly involves the reconfiguration of the metamolecule from a left-handed into a right-handed enantiomer and vice versa. This type of mechanical actuation is intricate and usually neither monolithically realizable nor viable for high-speed applications. Here, enabled by the phase change material $\text{Ge}_3\text{Sb}_2\text{Te}_6$ (GST-326), we demonstrate a tunable and switchable mid-infrared plasmonic chiral metamaterial in a proof-of-concept experiment. A large tunability range of the circular dichroism response from $\lambda = 4.15$ to $4.90 \mu\text{m}$ is achieved, and we experimentally demonstrate that the combination of a passive bias-type chiral layer with the active chiral metamaterial allows for switchable chirality, i.e., the reversal of the circular dichroism sign, in a fully planar, layered design without the need for geometrical reconfiguration. Since phase change materials can be electrically and optically switched, our designs may open up a path for highly integrated mid-IR polarization engineering devices that can be modulated on ultrafast time scales.

INTRODUCTION

The most obvious feature one can tune in active plasmonics is the spectral position of the plasmon resonance frequency. However, a less accessible but very important characteristic that lends itself as well to external control is chirality (Section 5.1).

Optically, chirality manifests itself in a circular dichroism (CD) signal (Eq. (5.3)), i.e., a difference in absorption of left-handed and right-handed circularly polarized light, which has opposite signs for mirror image pairs of metamolecules, so called enantiomers.

A large body of work exists on chiral metamaterials in the optical [168, 178, 219, 226, 239, 240], infrared [18, A2, 170, 219, 223, 241, 242], THz [174, 243–246], and GHz [167] regimes. Yet, comparably few demonstrations exist for switchable chiral metamaterials that can change their handedness under the influence of an external stimulus. Generally, reconfiguring the chiral building block such that it geometrically switches between the enantiomers will lead to a symmetric change in the CD signal, which has been demonstrated in the visible spectral region using solution-based DNA-self-assembled chiral structures [247, 248]. In the THz spectral regime, the generation of charge carriers through optical excitation in silicon was utilized to selectively activate certain parts of an overall achiral geometry to obtain an either positive or negative CD signal [220, 249–251]. These approaches are not available in the mid-infrared (MIR), which, however, is a highly interesting spectral region for plasmonics [252], e.g., due to the presence of molecular vibrational fingerprints and the atmospheric transparency window.

7.1 TUNABLE CHIRALITY

Here, we first experimentally demonstrate large spectral tunability of the circular dichroism response. To achieve this, we employ the chalcogenide phase change material $\text{Ge}_3\text{Sb}_2\text{Te}_6$ (GST-326), which is a representative of the chalcogenide compound family that has been successfully commercialized for optical data storage (DVDs), and recently received additional attention due to its exciting electro-optical properties that make it suitable as a new low energy, high contrast display material [109]. Plasmon resonances in metal nanostructures are very sensitive to their immediate dielectric environment, which has been extensively used for sensing purposes [37, 253]. When GST-326 is brought into proximity with a plasmonic nanoantenna, the large difference in the dielectric constant between amorphous ($n_a \approx 3.5 + 0.01i$) and crystalline ($n_c \approx 6.5 + 0.06i$) GST-326 [110] in the studied mid infrared spectral region (4–5 μm) leads to a large spectral shift of the particle plasmon resonance position. Therefore, a suitable combination of GST with a chiral metamaterial leads to a shifted circular dichroism signal upon actuation [254] (Fig. 7.1(b)). We

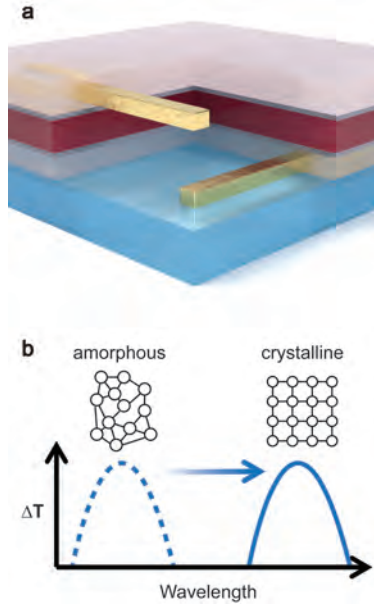


FIGURE 7.1. Tunable chirality concept. a) Active chiral plasmonic dimer stack consisting of 50 nm GST-326 (red) with two protective 10 nm ZnS/SiO₂ layers (grey) sandwiched between vertically-displaced, corner-stacked, orthogonal gold nanorods embedded in PC₄O₃ (light red). For better visibility of the nanorods, a cut-away is included at the edge of the stack. b) Thermal actuation of the phase change layer leads to a CD signal ΔT that is shifted to longer wavelengths.

choose a Born-Kuhn type chiral plasmonic dimer [A₂, 225, 229] as underlying system and modify it by sandwiching a thin layer of GST-326 between the two corner-stacked nanorods (Fig. 7.1(a)).

This has the twofold advantage of ensuring an optimum interaction with the nanorods, because the phase change layer is incorporated at the near-field coupling junction and ease of fabrication, because no additional lithography step is needed. The fabrication steps follow a modified recipe of the stacking procedure from [227] and are outlined in Fig. 7.2: a first electron beam lithography step is carried out to define alignment markers and the first layer of the chiral dimer (Fig. 7.2(a)). The length of the nanorods is $l = 660$ nm, the width $w =$

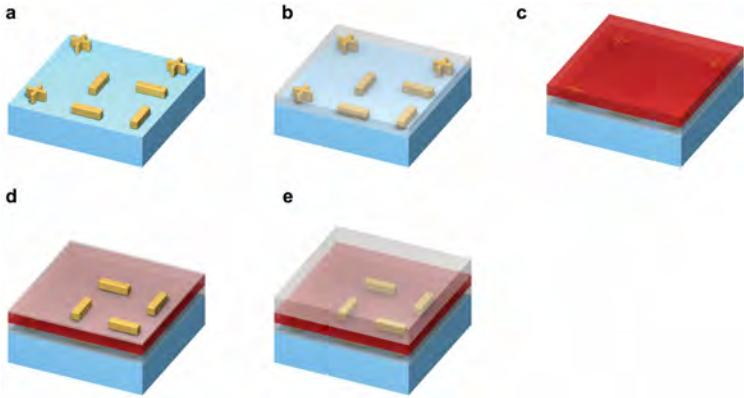


FIGURE 7.2. Fabrication flow chart. a) First electron beam lithography (EBL) step creates markers and the first layer of Au nanorods (50 nm). Spin-coating of a planarization layer consisting of PC₄O₃ (grey, 60 nm) smooths the surface. b) Sputter deposition of GST-326 (red) sandwiched between two thin protective layers of ZnS/SiO₂ (10 nm). c) Spin-coating of PC₄O₃ layer (10 nm) followed by second aligned EBL step defining the upper nanorods. d) Spin-coating of PC₄O₃ planarization layer (140 nm) to symmetrize the dielectric environment. e) SEM micrograph of fabricated right-handed structure (scale bar = 1 μ m). The top layer appears brighter. The irregular lattice spacing is used to avoid Rayleigh anomalies.

40 nm, and the thickness = 50 nm. A C_4 -symmetric supercell of chiral dimers is placed in a disordered arrangement over a 100 μ m x 100 μ m area in order to avoid Rayleigh anomalies in the high-index case. As substrate, we use CaF₂ to ensure mid-IR transparency. The spin-on polymer PC₄O₃ (JSR Inc., Japan) is applied as a 60 nm thick planarization layer and subsequently a 50 nm GST-326 layer sandwiched between 10 nm buffer layers of ZnS/SiO₂ is dc-magnetron sputter deposited. A second step of aligned electron beam lithography is carried out to define the upper nanorods, which are finally covered by 100 nm of PC₄O₃ to symmetrize the dielectric environment. The resulting SEM micrograph for a right-handed active structure is shown in Fig. 7.2 (e)). The lattice spacing is deliberately randomized in order to avoid Rayleigh anomalies in the optical spectra [O₂, 255]. The

structure parameters of the fabricated sample were chosen such that the fundamental plasmon resonance is located in the transparency window [110] of GST-326, i.e., between $2.8\ \mu\text{m}$ and $5.5\ \mu\text{m}$ for both the amorphous and the crystalline phase where absorption losses of such a thin film are negligibly small ($\ll 1\%$). To guide the design and predict the tuning behavior of the active chiral dimer, we carried out electromagnetic full-field simulations for the system described above including all layers with periodic supercells of period $p = 1600\ \text{nm}$ employing an in house-implementation of the Fourier Modal Method [118].

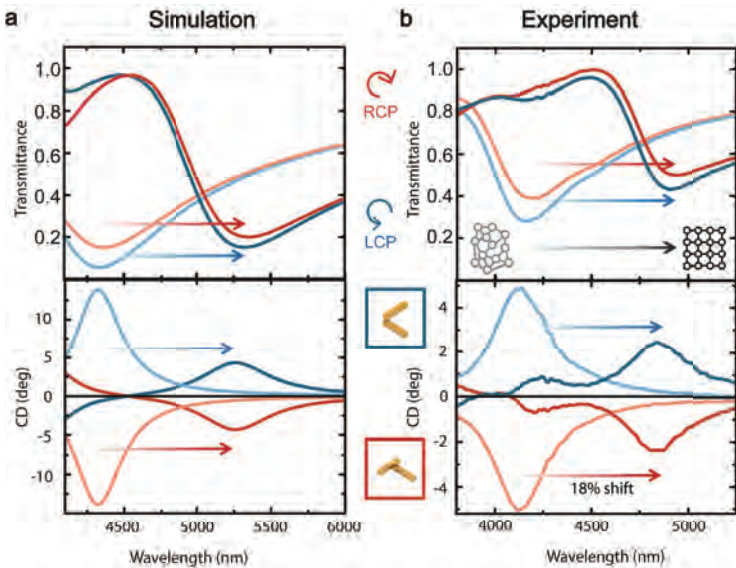


FIGURE 7.3. Tunable chirality experiment and simulation. a) Simulated transmittance (upper panel) and CD (lower panel) spectra through the active chiral dimer of left- and right-handed circularly polarized light for the amorphous (lighter curves) and crystalline (darker curves) state of the phase change material layer. b) Corresponding spectra to a) from FTIR measurements of the fabricated sample.

The results are shown in Fig. 7.3 (a), where lighter colored curves represent spectra for the GST-326 layer in the amorphous phase and

darker colored curves are associated with the crystalline phase. For both states, the transmittance spectra for a right-handed enantiomer under illumination with circularly polarized light are shown in the upper plot. One can clearly see that left- and right- circularly polarized light is transmitted differently, thus confirming the chiroptical nature of the investigated system. Additionally, a giant spectral shift of around 20% is obtained in the simulation when the sandwich layer undergoes a phase change from the amorphous to the crystalline state. The lower plot shows the CD spectra for both right- and left-handed enantiomers in degrees, where the formula was used for the conversion from the transmittance spectra. The experimental optical spectra taken from the fabricated sample are shown in Fig. 7.3(b) and were recorded with a suitably modified Fourier Transform Infrared Spectrometer (FTIR) [256] that was coupled to a microscope. Again, the lighter colored curves correspond to spectra taken with the sandwich layer in the amorphous state. Since as-deposited GST-326 is amorphous, these were taken right after fabrication. Here, for proof-of-concept purposes, we chose to thermally induce a transition to the crystalline state, which occurs for temperatures above the glass transition temperature of about 160°C [112]. To that end, the entire sample was heated for 30 minutes at 180°C under nitrogen atmosphere. The resulting transmittance and circular dichroism spectra of the crystalline state sample are presented as darker plots in Fig. 7.3(b). While the absolute transmittance values differ due to the fabricated sample consisting of disordered supercells leading to lower surface coverage than in the simulated periodic case, it is remarkable that the predicted giant shift of 18% is also experimentally realized. Previous studies [133] pointed out that simulations are typically merely interpreted as upper bounds to the shift. The excellent match of the magnitude of the shift can be possibly attributed to the fact that the GST-326 layer is completely surrounded by protective layers thus preventing degradation, e.g., through oxidation and diffusion of gold during the switching process. Conventionally, such layers are avoided in order to ensure direct contact of the phase change material with the plasmonic nanostructures that are to be actuated [257]. The reasoning is that this maximizes the interaction of the near-fields in the vicinity of the antenna with the change in the refractive index environment. However, we

are able to obtain shifting values that are comparable to literature values of systems that employed direct contact geometry. The reason for this is to be found in the coupled nanorod, i.e., dimer configuration that results in higher field enhancements at the gap than at the ends of individual nanoantennas. Nevertheless, both simulated and experimental cases can be seen as boundaries to the tuning range of the transmittance and CD spectra in the sense that all intermediate states can be continuously achieved through adjusting the amount of heat deposited in the phase change layer [258, 259]. This is due to the fact that crystallization in the material takes place as a nucleation process [260] where evenly distributed small crystallites form that subsequently grow larger and finally merge to one homogeneous film [107]. Any of these nucleation stages is stable in itself and the plasmonic structure responds to an average dielectric constant of its surrounding that could be determined for instance by using Maxwell-Garnett theory [31]. This effect has been experimentally demonstrated for achiral planar plasmonic systems [138].

7.2 SWITCHABLE CHIRALITY

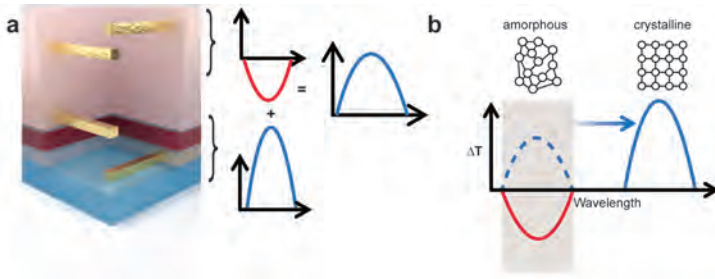


FIGURE 7.4. Switchable chirality concept. a) A right-handed active chiral dimer is cascaded with a left-handed passive chiral dimer of half its CD amplitude. The overall CD response is half that of the right handed chiral dimer. b) Thermal switching of the active chiral dimer shifts its CD signal red and exposes the underlying left-handed bias CD signal. The CD signal at the original wavelength region switches its sign.

Next, we want to emphasize the application potential beyond spectral tunability and demonstrate that, indeed, the wavelength tunability can be utilized to obtain a reversal in the sign of the circular dichroism signal. In the spectral region around 4150 nm where the CD peak is initially located, only very little CD response remains once the phase change material has been actuated, which is only possible due to the giant shift that the chiral dimer system undergoes. A smaller shift would not be able to push the entire CD signal out of the initial spectral range since plasmon resonance peaks and therefore their associated CD spectra are tied together, exhibiting relatively large full-width-half-maximum values. We can utilize this unique situation to construct a scheme that is laid out in Fig. 7.4(a), which employs a bias layer to convert the spectral shift to a switching of the CD signal. Given a right-handed active chiral dimer (lower nanorod pair with sandwich layer) with a positive CD signal, we can design a left-handed passive chiral dimer (upper nanorod pair without sandwich layer) that possesses a negative CD signal of half the amplitude. As long as these two systems are separated by a distance that is sufficiently large (> 200 nm) to avoid near-field coupling, the resulting CD spectra of light passing through both systems will be the sum of the individual CD spectra [221]. In the present case, the compound system possesses a positive CD signal of half the amplitude of the active chiral dimer. When this device is subjected to thermal actuation, the positive CD signal of the right-handed active dimer will shift away to the red, thus completely exposing the underlying negative CD signal. Overall this then appears like a switch in the CD signal at the original spectral position. The compound system can be viewed as an optical device that can switch its CD response. Since it does not matter for applications through which underlying physical mechanism right- or left-circularly polarized light is preferentially transmitted, the effect of a configurational change from a right-handed to a left-handed plasmonic enantiomer can thus be created through precise design of a bias layer that is overlaid with an active chiral metamaterial of high tuning range.

To experimentally demonstrate this concept, we carried out a parameter sweep of various passive chiral dimers in our numerical full-field simulation technique to find a suitable parameter set that has

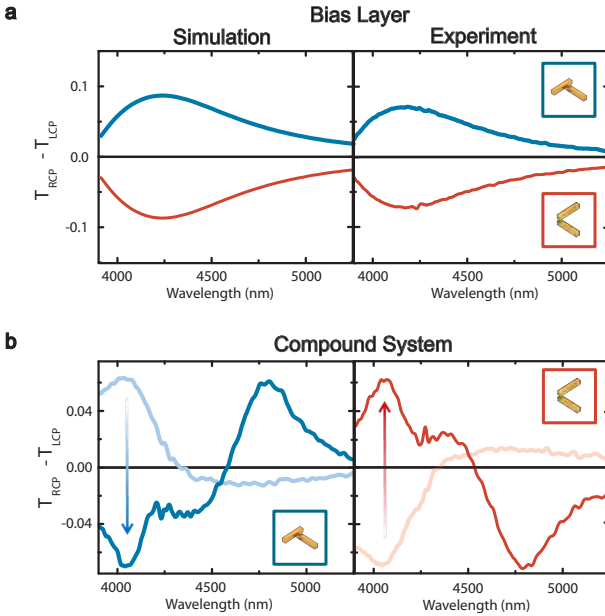


FIGURE 7.5. Switchable chirality. a) Simulated and measured differential transmittance spectra $T_{\text{RCP}} - T_{\text{LCP}}$ of circularly polarized light for both enantiomers. b) Experimental results for the cascaded system consisting of the active chiral dimer and the opposite-handed passive bias dimer. The CD signal switches its sign symmetrically for both opposite-handedness combinations of the active chiral dimer with the passive chiral bias layer.

roughly half the CD signal of the active chiral dimer. We first varied the nanorod length to spectrally match the position of the active chiral metamaterial layer in the amorphous case ($4.15 \mu\text{m}$) and subsequently varied the interlayer separation between the nanorods to tailor the strength of the CD signal [A2]. The best match was obtained for nanorods with length $l = 800 \text{ nm}$, width $w = 40$ and thickness $t = 40 \text{ nm}$ that were vertically separated by $d = 60 \text{ nm}$. The results are shown on the left in Fig. 7.5(a). Subsequently, a corresponding sample with the same parameters was fabricated and the CD spectrum was recorded. Note, that here we used a periodic arrangement of the

supercell with $p = 1800$ nm in both simulation and experiment because the comparably low refractive index of PC403 already prevents the formation of Rayleigh anomalies in the MIR for the chosen periodicity. The remarkable agreement in shape and amplitude of the resulting experimental data with the simulated data stems from the fact that the fabrication process for the passive chiral dimer is highly optimized and very well controlled. Fig. 7.5(b) shows the overall optical response of the bias layer overlaid with the active chiral dimer. As designed, the CD signal at 4200 nm in the amorphous state is exactly opposite to the CD signal in the crystalline state for both fabricated enantiomers.

CONCLUSION

In summary, we have demonstrated, for the first time, a tunable chiral metamaterial that operates in the mid-IR spectral region with a tuning range from 4.15 μm to 4.90 μm . Subsequently, we have shown how to use this feature together with a bias layer to achieve a sign flip in the CD signal. Both functionalities have been achieved through easy-to-fabricate layered geometries without free-standing or moving parts. Here, for proof-of-concept purposes, we only thermally induced a one-directional phase change from the amorphous to the crystalline state. However, it is well-known that GST can be electrically and optically switched on ultrafast time scales [106, 261]. Our design that includes a continuous layer of GST can be modified to only incorporate patches of GST at the ends of the nanorods, which would ensure small enough volumes for electrical switching while retaining the wavelength tuning effect for the plasmon resonance. For optical switching no further modification of the geometry is needed, as large-area fs-switching of GST has been demonstrated already [105]. Therefore, our work opens up a path for high frequency polarization modulation in the mid-infrared spectral region that would be highly beneficial for applications such as thermal imaging, polarization sensitive detection, and stereo display technologies. Most importantly, the phase change material GST-326 need not be restricted to active plasmonics applications where only the resonance wavelength is tuned via the change in the nanostructure dielectric environment. Moreover,

it can be broadly employed as part of functionally complex but structurally simple designs that offer polarization engineering capabilities in the mid-infrared spectral region.

STUDYING ENHANCED CHIROPTICAL
SPECTROSCOPY

Plasmon-enhanced circular dichroism has established itself as a promising candidate to push the limits of molecular handedness detection to the extremes, namely towards a monolayer or even to a single molecule. A multitude of intricate mechanisms, both chemical and physical, have to contribute individually or in unison to an enhancement that is large enough that it may bridge the several orders of magnitude of lacking signal strength when detecting small analyte quantities in a circular dichroism scheme. Here, we assess in isolation the contribution arising from electromagnetic interactions between a homogeneous chiral medium and plasmonic structures. Using a suitably modified full-field electromagnetic simulation environment, we are able to investigate the viability of various canonical achiral and chiral plasmonic configurations for substrate-enhanced chiroptical spectroscopy. A clear hierarchy in enhancement factors is revealed that places achiral plasmonic gap-antennas at the top, thus outperforming its chiral equivalent, the Born-Kuhn type plasmonic dimer. Moreover, the importance of coplanarity of the incident rotating circular polarization field vector with the resonantly enhanced field vector in the plasmonic hot-spot is demonstrated. Taking everything into account, we obtain an enhancement of three orders of magnitude from purely electromagnetic interactions, thereby charting this part of the CD enhancement landscape. In this chapter, we will first discuss the implementation of chiral media in an finite element method (FEM) simulation environment and then the numerical results of the various studied geometries.

8.1 IMPLEMENTATION OF CHIRAL MEDIA IN COMSOL

While it is straightforward to model the linear optical response of plasmonic materials such as gold, the electromagnetic behavior of chiral media, a subset of bi-isotropic media, requires some adaptation of existing commercial Maxwell solvers. For our studies of plasmon-enhanced circular dichroism (PECD) in the next section, we chose to modify a standard Comsol RF simulation environment (Section 2.4.2) by implementing the general bi-isotropic constitutive equations Eqs. (5.12) and (5.13) and setting $\chi = 0$. A number of tests have been carried out to check the viability of the modifications. In this section, we present two sanity checks that compare the numerical results of our FEM-based model with analytical descriptions found elsewhere [158, 196]. Namely, the transmission through a bi-isotropic slab (Fig. 8.1) and light scattering from a spherical gold nanoparticle surrounded by a chiral shell (Fig. 8.2).

8.1.1 *Transmission through a Bi-isotropic Slab*

In the first example, linearly polarized light is normally incident onto a lossless bi-isotropic slab surrounded by air (Fig. 8.1(a)). Following reference [196], we define the impedance $\eta = \sqrt{\mu/\varepsilon}$ and the relative Pasteur and Tellegen parameters as $\kappa_r = \kappa/n$ and $\chi_r = \chi/n$, where n is the refractive index.

Light that passes through the slab exhibits polarization conversion as can be seen in Fig. 8.1(b) (cf. Eq. (3.140) and Fig. 3.21 in [196]). Here the magnitude of the cross-polarized reflection coefficient $|R_{cr}|$ is shown for $\eta_2 = \eta_0$ and different values of χ_{2r} as a function of the normalized thickness k_2L . The subscript 2 denotes here properties of the bi-isotropic medium. In Fig. 8.1(c) and (d), both co- and cross-polarized reflection coefficients R_{co} and R_{cr} , respectively, are shown for varying $\eta_2 = \eta_0$ and fixed $\chi_{2r}=0.9$, cf. Eqs. (3.122) and Fig. (3.22) in [196]. Finally, the co- and cross-polarized transmission magnitudes T_{co} and T_{cr} are presented in Fig. 8.1(e) and (f) for $\chi_{2r}=0.9$, $\eta_2/\eta_0 = 0.6$, and nonvanishing κ_r , see Eqs. (3.98) and (3.124) in [196]. The numerical results obtained by our implementation of the bi-isotropic constitutive

equations are plotted as dotted lines in Fig. 8.1 and exhibit an excellent agreement with the analytical curves (solid lines) over the whole parameter range.

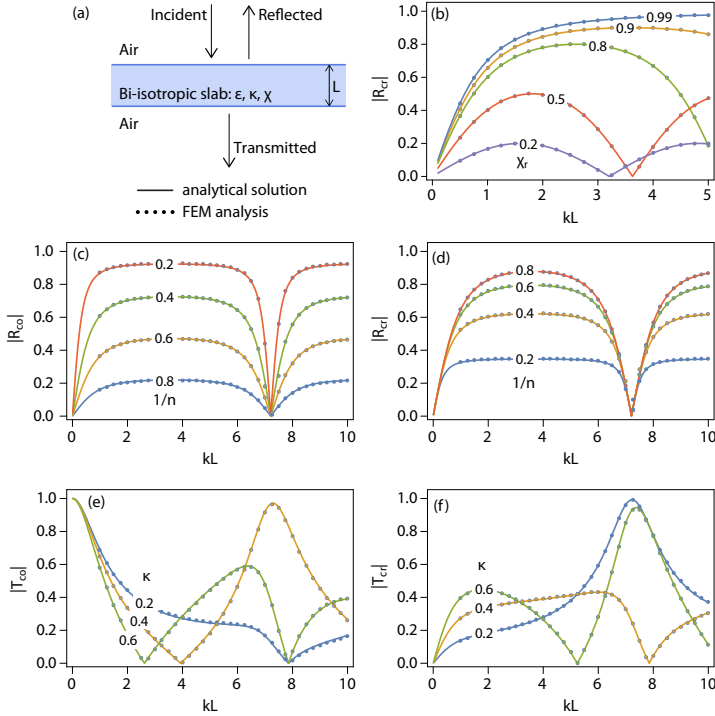


FIGURE 8.1. Transmission through a bi-isotropic slab in air: Comparison of FEM with analytical solution [196]. Solid curves show analytical dependencies, whereas dots represent FEM data. (a) Schematic of the geometry. (b) Cross-polarized reflection coefficient $|R_{cr}|$ as a function of normalized thickness k_2L , for impedance $\eta_2 = \eta_0$ and varying χ_{2r} ($\epsilon = 1, \mu = 1, \kappa = 0$). (c) Co-polarized and (d) cross-polarized reflection coefficients R_{co} and R_{cr} , respectively, as functions of the normalized thickness k_2L , for $\chi_{2r} = 0.9$ and different ratios η_2/η_0 ($\mu = 1, \kappa = 0$). (e) Co-polarized and (f) cross-polarized transmission coefficients T_{co} and T_{cr} , respectively, as functions of the normalized thickness k_2L , for $\chi_{2r} = 0.9, \eta_2/\eta_0 = 0.6$, and varying κ_r ($\mu = 1$).

8.1.2 Metal-Core Chiral-Shell Particle

In the second example, we consider light scattering at a spherical gold nanoparticle surrounded by a chiral shell. The sphere radius is 100 nm, the dielectric function for gold is fitted with a phenomenological Brendel–Bormann model [262], the chiral shell is 20 nm thick, and the chiral material is described by Appendix A.o.1 with the following parameters: $\varepsilon_b = 1$, $\omega_0 = 2\pi c/\lambda_0$, $\lambda_0 = 380$ nm, $\Gamma = -0.41$ eV, $\beta = 4.1 \cdot 10^{-4}$ eV, and $\mu = 1$. The analytical solution of this system has been derived using Mie theory [263] and is shown in Fig. 8.2(a) (reproduced from [158]). The numerically calculated extinction (black), scattering (red), and absorption (blue) cross-section spectra are shown in Fig. 8.2(b) and are in excellent agreement with the analytical results.

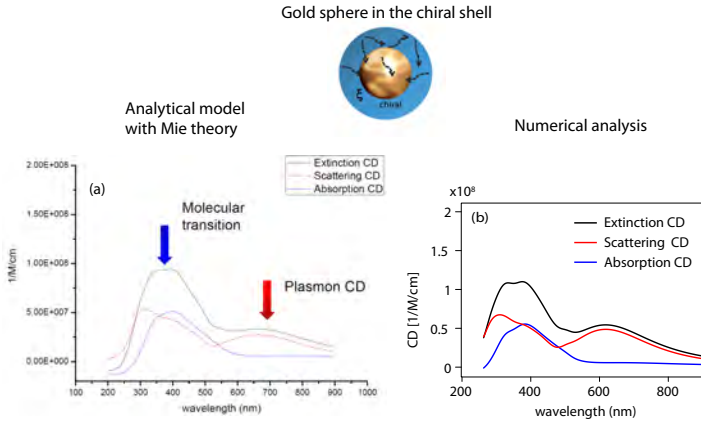


FIGURE 8.2. Spherical gold nanoparticle surrounded by chiral shell: (a) Analytical solution based on Mie theory [158], and (b) Numerically calculated results using the modified Comsol environment.

8.2 RIGOROUS NUMERICAL STUDY OF PLASMON-ENHANCED CD

Introduction

Surface plasmon-based near-field enhancement delivered through specifically designed substrates has proven to be highly successful for ultrasensitive optical biosensor applications such as surface-enhanced Raman spectroscopy (SERS) [264] and surface-enhanced infrared spectroscopy (SEIRA) [265], where it can boost responses down to the monolayer and even to the single molecule regimes [266]. The underlying detection schemes record the changes in intensity of the probing light, regardless of its polarization. However, taking the aspect of polarization into account provides valuable additional information which is precisely the domain of chiroptical spectroscopy techniques that are sensitive to the chirality [147] (handedness) of a molecule. Among these, circular dichroism (CD), i.e., differential absorption of left- and right-handed circularly polarized light, is of particular relevance for the study of biomolecules. Apart from being able to unambiguously distinguish the enantiomers of a chiral molecule, it can precisely determine the macroscopic conformation of large complex molecules [185]. As these molecules are prevalent in pharmaceutical applications [267], it is of great importance to be able to operate chiral analyses at physiological—hence very low—concentrations. Recently, experimental [151, 268] and theoretical [269, 270] work has been carried out on plasmon-enhanced circular dichroism spectroscopy, reporting dissymmetry enhancement factors of up to 105 and attributed to plasmon-generated superchiral near-fields [A5, 150, 152, 154–156, A6, 271] or induced optical activity due to near-fields, both at isolated plasmonic nanostructures and at hot spots between closely spaced structures. [158, 160, 162, 272–276] This substrate-based approach is akin to SERS and SEIRA but fundamentally differs from routes to enhanced circular dichroism that rely on self-assembled chiral plasmonic macrostructures. The latter approach judiciously incorporates the analyte as part of the scaffolding material for the nanoparticles, thus influencing the geometrical configuration of the chiral plasmonic structure and thereby its associated CD spectrum [277–279]. While

previous theoretical work focused on either investigating a fixed number of chiral molecules modeled as point dipoles [160, 276, 280] or analyzing optical chirality in the vicinity of plasmonic nanostructures by using Mie calculations [270] or full-field simulations, so far, comprehensive three-dimensional numerical studies encompassing both the plasmonic structure and chiral molecular material have not been carried out. It has been shown, however, that chiral media can be treated with chiral Mie theory, and full-field simulations [281, 282].

The parameters are modeled as [263]:

$$\varepsilon = \varepsilon_b - \gamma \left(\frac{1}{h\omega - h\omega_0 - i\Gamma} - \frac{1}{h\omega + h\omega_0 + i\Gamma} \right) \quad (8.1)$$

where ε_b denotes the background refractive index, the coefficients γ and β the amplitude of absorptive and chiral properties; $\omega_0 = 2\pi c / \lambda_0$, where λ_0 corresponds to the wavelength of a molecular absorption resonance with broadening determined through damping Γ . Furthermore, the chiral medium is assumed to be nonmagnetic with $\mu = 1$. The values for all other parameters were chosen to represent typical values found in naturally occurring neat, i.e., 100% concentration, chiral materials [185] (cf. Appendix A.o.1).

In this chapter, we present, for the first time, a rigorous finite-element-method based study on the effects of various canonical plasmonic building blocks on the enhancement of molecular CD signals. Full-field simulations that take both the complex plasmonic structure and the chiral medium into account reveal the importance of highly-concentrated near fields. Most importantly, we demonstrate that the relative orientation between incident light and plasmonic modes plays a crucial role. This leads to rather counter-intuitive consequences for the performance of different plasmonic antenna shapes where achiral structures clearly outperform their chiral equivalents. The investigated structures consist of homogeneous and isotropic chiral medium patches placed in the vicinity of plasmonic nanoantennas, with the molecular resonance of the chiral medium patches in the UV range and the plasmonic resonance in the near-IR. Our numerical approach contains all electromagnetic effects that can contribute to an enhancement of the CD signal of the chiral medium patches, while other effects, e.g., of chemical nature such as charge transfer through

bonds formed by chemisorbed analytes to the plasmonic nanostructure are not considered. An extension to oriented chiral molecules by using anisotropic material tensors as well as the investigation of matched molecular and plasmonic resonances is in principle possible, but we focus here on the more common case, in which the molecular and the plasmonic resonance are spectrally separated and the molecules are randomly oriented.

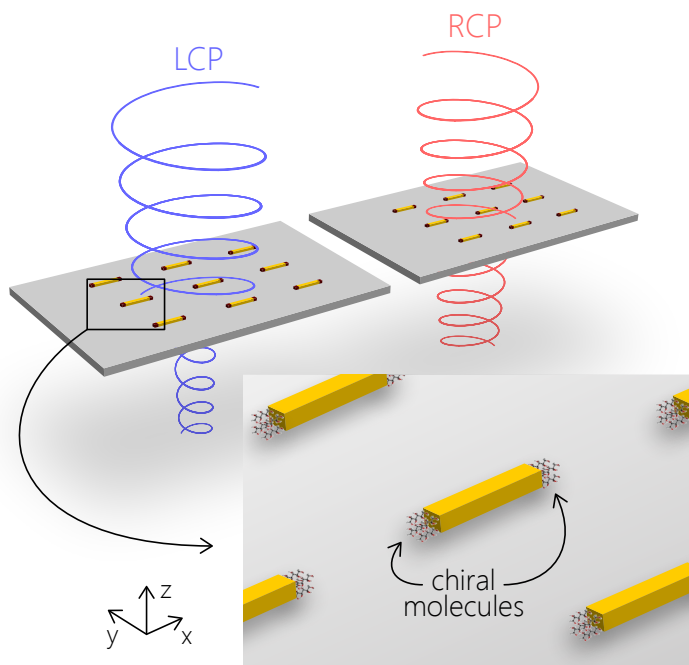


FIGURE 8.3. Schematic of plasmon-enhanced circular dichroism (PECD) detection scheme. The inset shows the chiral material patches that are placed at the hot-spots of the plasmonic antennas.

8.2.1 *Standard PECD Setup with Nanorods*

The general setup for plasmon-enhanced circular dichroism spectroscopy (PECD) employs a standard CD detection scheme in conjunction with arbitrarily shaped plasmonic nano-antennas as a substrate for the chiral material (Fig. 8.3). Ideally, the material under investigation should be placed in the hot-spot regions of the nanoparticles in order to assess the upper limit for the obtainable plasmon-enhancement.

The various optical responses (Fig. 8.4) of the system employing periodically arranged gold rod structures shown in Fig. 8.3 illustrate the key features of PECD spectroscopy. The rods have a length $l = 150$ nm, a width $w = 40$ nm, and a thickness $t = 40$ nm, and they are arranged in an array of period $p = 650$ nm in both directions of the plane. Typically, molecular CD resonances of interest are located around 250 nm, while the utilized plasmonic structures exhibit their fundamental resonance at longer wavelengths, here at 780 nm, such that no spectral overlap of the absorption peaks occurs (Fig. 8.4(a)). The black line in Fig. 8.4(a) shows the absorption spectrum of the compound system, whereas the gray curve corresponds to the absorption from the chiral medium patches by themselves. The spectral features that are visible in the region between the molecular and fundamental plasmonic resonance stem from Rayleigh modes and higher order plasmon modes, which we do not further investigate here. The CD peak for the chiral patches is naturally located at the spectral location of their molecular absorption resonance (Fig. 8.4(b)). Note the weakness of the CD signal of about 10^{-4} mdeg at its maximum, despite assuming neat liquid model parameters. This results from the small analyte quantity involved, i.e., 40 nm sized chiral medium cubes instead of uniform millimeter thick analyte layers that are usually required for unenhanced CD spectroscopy, where the detection limit is typically about 1 mdeg. The achiral plasmonic nanorods inherently do not exhibit a CD signal. However, due to the presence of the chiral material that interacts with the near-fields of the rods, a difference in absorption for LCP and RCP illumination is induced inside the metal nanoparticles. This difference manifests itself as a CD signal at the position of the plasmon resonance (orange plot Fig. 8.4(b)). Generally, CD signals can take positive and negative values depending on the

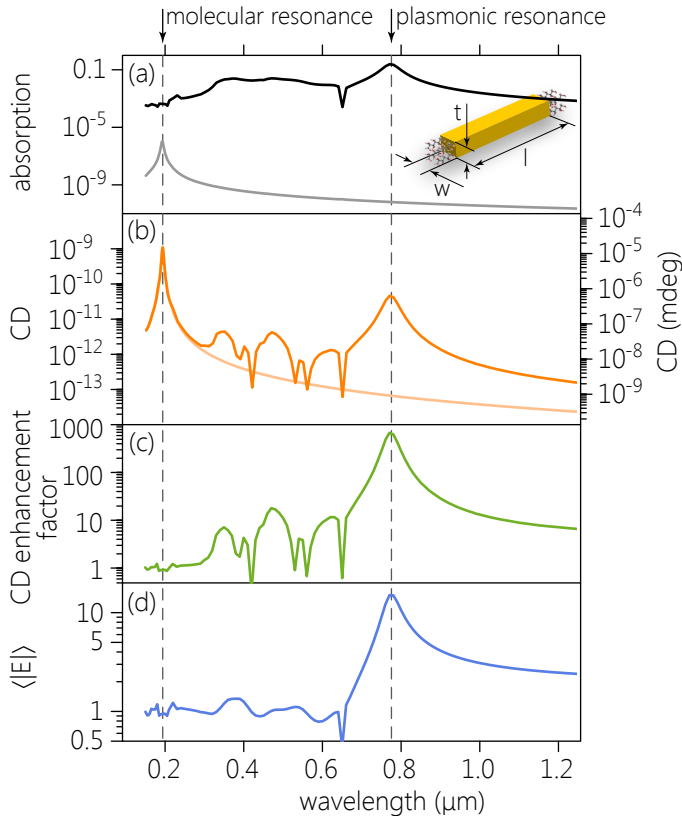


FIGURE 8.4. Optical responses of chiral medium patches located at the hot spots of a plasmonic rod-antenna array. Paler lines indicate the chiral response of the patches without antennas. (a) Absorption for linearly polarized normal incidence. (b) Circular dichroism signal (absolute values). The scale on the right marks CD values as ellipticity in millidegrees. (c) Enhancement factor of the CD signal. (d) Averaged electric field enhancement within the volume occupied by the chiral patches.

handedness of the examined sample; here, we present only the absolute values as we concentrate on determining enhancement effects

that occur symmetrically for opposite enantiomers. In order to quantify such enhancement phenomena, we define the CD enhancement factor f as ratio between the absolute values of the CD signal of the chiral medium patches alone and with plasmonic antennas. Note that this definition only accounts for the enhancement of the CD signal for a fixed size and position of the chiral patches at a certain wavelength. In order to obtain larger total CD signals, it is of course possible to increase the size of the chiral patches. However, investigating chiral patches that extend the region of the plasmonic near fields does not reveal any enhancement effects due to the plasmonic resonances. Plotting the CD enhancement factor for the case of the plasmonic nanorod array with chiral patches provides a maximum enhancement factor of about 750 (Fig. 8.4(c)). It is important to note that this enhancement factor is independent on the magnitude of the Pasteur parameter κ as long as it is small with respect to the dielectric permittivity, which is usually the case for realistic chiral analytes. Therefore, our results reveal fundamental insights independent of the actual properties of the chiral medium. The enhancement effect is clearly tied in with the effect of field enhancement that can be observed at the ends of the metal nanorods. Fig. 8.4(d) shows the electric field enhancement, which has been calculated by averaging the absolute electric field value over the volume occupied by the chiral medium cubes and normalizing to the amplitude of the incident electric field:

$$\langle |E| \rangle = \frac{1}{V} \int_V \frac{|E|}{E_0} dV. \quad (8.2)$$

We additionally analyzed the origin of the enhanced CD signals by distinguishing between energy absorbed in the metallic nanoantenna and in the chiral medium patches (Appendix A.1). We find that the CD signal is dominated by the contribution of the nanoantenna, so that the most relevant mechanism is so-called induced CD [276]. Note however, while the CD enhancement obtained for the present case of plasmonic rod antenna arrays is an undeniably large effect, it still yields an overall CD signal below the detection limit of 1 mdeg for common CD spectrometers.

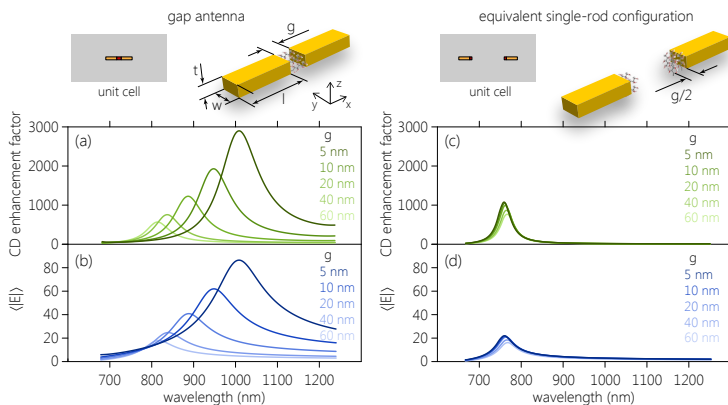


FIGURE 8.5. Gap antenna and rod antenna enhancement factors. (a) CD enhancement factor for gap antennas of different gap sizes. (b) Averaged field enhancement within the volume occupied by the chiral medium in the case of gap antennas. (c) CD enhancement factor of the equivalent single rod antenna configuration for varying chiral medium volumes with sidelength g . (d) Averaged field enhancement within the volume occupied by the chiral medium in the case of rod antennas.

Therefore, we carried out numerical studies of variations of the basic rod antenna geometry to assess whether higher CD enhancement factors can be obtained.

8.2.2 Gap Antenna Enhancement Factors

As near-field concentration plays a crucial role, the next iteration of the rod antenna geometry is the gap antenna, i.e., two rod antennas aligned along their long axes such that they are interacting through the near fields at the junction formed between them. In the gap region, the field enhancement is larger than at the ends of a rod antenna alone [283]. We studied the geometries presented in Fig. 8.5: the gap antenna has dimensions $l = 150$ nm, $w = 40$ nm, and $t = 40$ nm with gap sizes g varying from 5 nm to 60 nm. The gap region is fully occupied by the chiral medium, i.e., its dimensions are 40 nm \times 40 nm \times g .

The antennas are arranged periodically with period $p_x = 650$ nm and $p_y = 650$ nm. In order to directly compare the gap antenna CD enhancement factors to those obtained from a single rod antenna, we used an equivalent geometry that does not exhibit gap hot spots by placing two rod antennas at a distance from one another that is sufficient to avoid near-field coupling. In particular, the end-to-end distance between the two rods was chosen to be 175 nm. The chiral medium volume was cut in half for this geometry compared to that employed for the gap antenna, with one half patch each being placed at the ends of the rod antennas that face each other. As expected, the field enhancement for the gap antenna is higher than for the single rod antenna. For the smallest gap size of $g = 5$ nm, the gap antenna field enhancement is four times higher than for single rod antennas. In this case, the highest CD enhancement factor ratio is achieved between the two systems. The gap antenna exhibits a CD enhancement factor of 3000 and the equivalent single-rod configuration yields only one third of that with a CD enhancement factor of about 1000. The average field and CD enhancement factors show a slight increase for the single-rod geometry as the chiral medium patch size decreases, which happens due to the fact that the near fields are stronger closer to the antenna surface. Consequently, PECD enhancement benefits are more pronounced for small judiciously placed chiral analyte patches and decrease when using continuous analyte layers, because the chiral material outside the near-field regions of the plasmonic antennas does not contribute to an enhanced CD signal. It should be mentioned that the gap antenna with gaps 40 nm and 60 nm provide slightly lower CD enhancement than equivalent single rod configurations. We attribute this to the more efficient excitation of higher diffraction orders by the gap antenna as compared to single rods, which results in a non-trivial redistribution of radiation to the far field. However, a detailed discussion of the influence of higher diffraction orders and other grating effects on the CD enhancement is beyond the scope of the work we carried out.

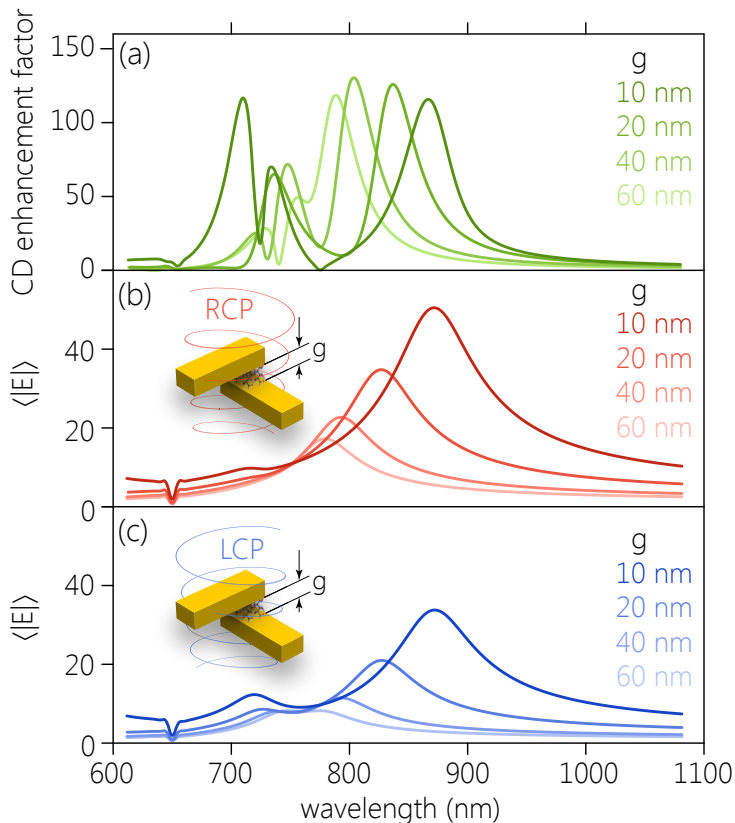


FIGURE 8.6. Chiral plasmonic dimers with chiral medium patches placed in their hot-spot region. (a) CD enhancement factor for different gap sizes. (b) and (c) show the averaged electric field enhancement within the hot-spots of the plasmonic dimers for RCP and LCP incident light, respectively.

8.2.3 Chiral Dimer Enhancement Factors

Furthermore, we tested if the chiral equivalent of the gap antenna dimer, i.e., a Born-Kuhn-type chiral dimer $[A_2]$, yields higher CD enhancement factors Fig. 8.6. We used the same dimensions as before for the rods that constitute the chiral dimer with $l = 150$ nm, $w = 40$ nm,

and $t = 40$ nm, and vertically varying gap sizes g . The chiral dimer itself already possesses a CD signal that would appear as background in the PECD measurement. Therefore, the CD enhancement factors presented in Fig. 8.6(a) were obtained from baseline corrected CD signals (cf. Appendix A.o.2). Due to mode hybridization, a bonding and anti-bonding mode can be excited depending on the handedness of the incident illumination Section 6.2. Here, we present the results for a left-handed dimer for which the field enhancement in the gap region is slightly larger for RCP light (Fig. 8.6(b)) and comparable to that obtained for the achiral gap-antenna. However, the CD enhancement factor is one order of magnitude lower than in the previously considered case of the gap-antenna (Fig. 8.6(a)).

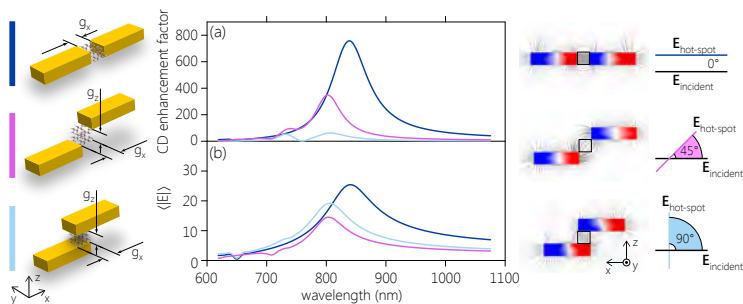


FIGURE 8.7. Enhancement factors for different dimer configurations (geometries are schematically shown on the left). (a) CD enhancement factor. (b) Electric field enhancement factor within the hot-spot regions. On the right, electric field lines and charge distributions are depicted at the resonance wavelength.

8.2.4 The Role of Field Vector Alignment

The significant drop in CD enhancement for the chiral dimer can be explained by considering the intermediate geometrical configurations schematically shown in Fig. 8.7 on the left. The chiral cubic patches have the same dimensions as before with $g_x = g_z = 40$ nm. The planar gap antenna delivers the highest CD enhancement, which drops

to about half its value for the second geometry from the top where one of the rod antennas has been vertically lifted out of the plane. This value further decreases by an order of magnitude when the ends of the nanorods overlap (Fig. 8.7(a)). The average field enhancement, however, drops only roughly by a factor of two. This indicates that the relative orientation of the incident electric field vector and the electric field vector in the hot-spot region is of great importance for plasmon-enhanced CD signals. While the standard gap-antennas possess hot-spot electric field vectors that are parallel to the incident electric field vector, this is not true for the other two cases. In particular, the hot-spot and incident field vectors are mostly orthogonal to each other for the gap-antenna where the ends are overlapping each other (Fig. 8.7 right side), which likely causes the dramatic reduction of the CD enhancement effect.

Conclusion

In summary, we studied the contribution of macroscopic electromagnetic effects to plasmon-enhanced CD spectroscopy. To this end, we implemented chiral constitutive equations in the COMSOL RF simulation environment. The highest enhancement factor is achieved for the standard planar gap-antenna, which both outperforms the single rod antenna and its chiral equivalent, the Born-Kuhn type dimer. Careful analysis of intermediate geometries revealed the pivotal role that the mutual orientation of incident and hot-spot electric field vectors plays. In our findings, CD enhancement is highest for geometries where these field vectors are parallel to one another and when, simultaneously, the average field enhancement value is high. The large CD enhancement of roughly three orders of magnitude constitutes the electromagnetic contribution to plasmon-enhanced CD spectroscopy. The limiting aspect here lies in the small volumes occupied by enhanced near-fields at the hot-spots of plasmonic antennas. Only in these regions, electromagnetic CD enhancement occurs. It should be noted that in the cases without any additional alignment effects or chemical enhancement [284] that may occur for chemisorbed analytes and are strongly analyte dependent, it might be more practical to measure the molecular resonance directly in the ultraviolet spectral region when

employing a substrate-based enhancement scheme, as the molecular CD resonance remains stronger than the induced CD signal at 780 nm in absolute terms. The ratio between the maximum values of induced CD (at the plasmonic resonance) and molecular CD (without plasmonic nanoantenna at the molecular resonance) reaches about 0.04 for the rod antenna, and 0.17 – 0.52 for the gap antenna with gap sizes of 5 – 60 nm, respectively. Only in those cases where one is restricted to typical plasmon resonance wavelengths for detection, a pure electromagnetic plasmon-enhanced CD scheme is advantageous for measuring the CD signal from small patches of chiral media at the hot-spots of the electric fields. The present thorough analysis is an important step towards dissecting the different contributing effects involved in plasmonic substrate-based CD enhancement schemes. As with SERS, large overall enhancement in plasmon-enhanced CD is expected to be composed of both physical and chemical parts. Note that the contribution of the chemical part may be relevant in experiments, but it is beyond the scope of this work to discuss the potentially involved mechanisms as well as to estimate the magnitude of the resulting CD enhancement due to the chemical effects. While the determined electromagnetic enhancement of three orders of magnitude does not strictly represent an upper bound, it is reasonable to assume that for homogeneous and isotropic chiral medium patches, the present numerical results give a good estimate of the maximally experimentally achievable CD enhancement based on electromagnetic effects. This is due to our finding that high field enhancement, which is challenging to achieve in real devices, is the overall limiting factor. Despite assuming the chiral medium patches to be homogeneous and isotropic here, future work will also include molecular orientation effects that can be easily implemented in our numerical method by using tensorial parameters. Such additional detail might very well reveal even higher electromagnetic enhancement factors.

Methods

Simulation Details

To adequately resolve the electromagnetic effects, we chose at least five tetrahedral elements with second-order shape functions per local

wavelength. At least two second order elements were used to resolve the field variations occurring within the skin depth at the surface of the metal. A denser mesh was generated in the near-field regions at the hot-spots to register the weak chiral signals from the chiral medium. Each simulation was checked for convergence.

CD enhancement factors

Circular dichroism is calculated as a difference in absorption of left- and right-handed circularly polarized incident light $CD=A_{RCP} - A_{LCP}$. To obtain the CD enhancement factor, we normalize the CD signal from the combined plasmon-chiral medium system by the CD signal of the chiral medium itself at the same wavelength

$$f = \frac{|CD_{total}|}{|CD_{chiralmedium}|}. \quad (8.3)$$

CONCLUSION AND OUTLOOK

In this thesis, we have demonstrated, for the first time, active complex plasmonic geometries based on a phase-change material (PCM). The large refractive index contrast of $\text{Ge}_3\text{Sb}_2\text{Te}_6$ in its amorphous and crystalline phases coupled with low-losses in the mid-infrared (MIR) spectral region proved to be the key for designs with active functionality. Only through the dramatic change in refractive index, the plasmon peaks associated with the crystalline and amorphous substrate states are ensured minimal overlap Fig. 9.1. This allows for design approaches that interleave nanoantennas with different functionalities onto the same substrate footprint.

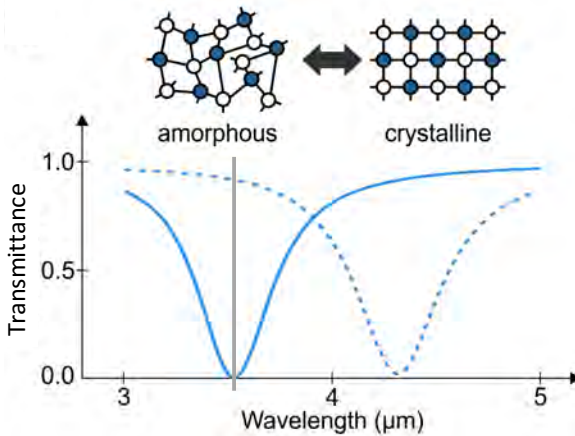


FIGURE 9.1. PCM enabled tunable plasmon peaks.

In particular, we have numerically studied and experimentally realized beam steering (Fig. 9.2a), varifocal lensing (Fig. 9.2b), tunable chirality (Fig. 9.2c) and switchable chirality (Fig. 9.2d).

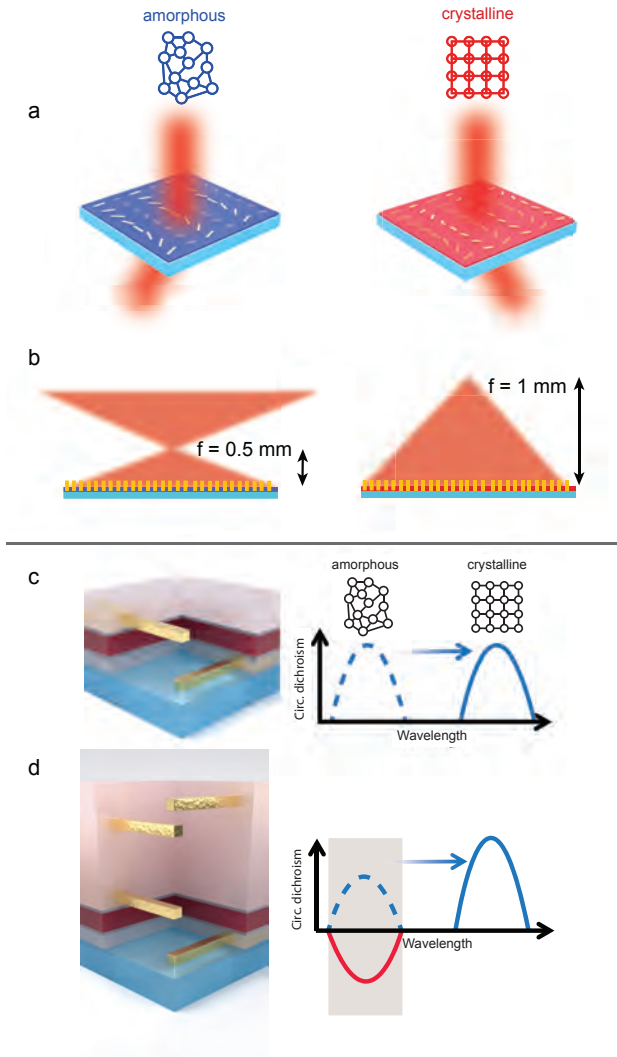


FIGURE 9.2. Various realized active plasmonic systems: (a) beam steering (b) varifocal lensing (c) tunable chirality (d) handedness switchable chirality

While our demonstrations utilized hot-plate induced phase changes, future work will focus on the direct integration of optically or electronically reversibly switchable devices. In the case of electronically switchable devices, it will be necessary to dice the continuous PCM substrate layer into smaller patches, which then can be addressed via a standard cross-bar configuration of preferably transparent (e. g. indium tin oxide) electrodes. Furthermore, all current designs obtain their functionality through the excitation of a localized surface plasmon polariton resonance (LSPR) mode, which is associated with strong absorption. It is envisioned to extend the investigated concepts into the realm of high-efficiency devices, which would possibly be based on high-index dielectric resonances.

In the second part of this thesis, we were able to establish and isolate the direct chiral plasmonic realizations of the electronic theories of optical activity. In particular, we experimentally demonstrated the plasmonic omega structure (Fig. 9.3a), the chiral dimer Born-Kuhn structure (Fig. 9.3b) and the spiral-ramp structure (Fig. 9.3c). Consistent with theory, the omega structure exhibits one single CD peak whereas the chiral dimer shows a typical bi-signate line form with two consecutive peaks of opposing signs. In particular, we could show that the Born-Kuhn model can be thought of in terms of chiral dimer hybridization with preferred selective excitation of modes that match the symmetry of the exciting light. Furthermore, we were able to use the insight from the Born-Kuhn model to interpret the occurrence of chiral modes for the spiral-ramp structure. Therefore, our studies offer clean intuitive images that can be invoked when designing complex chiral structures. Using the two basic components of omegas and vertically-displaced nanorods, arbitrarily complicated CD responses can be tailored at will by mixing and matching different sized constituents. Moreover, these canonical chiral structures are excellent candidates for precise future studies on single particle CD, chiral nonlinear effects and magneto-chirality.

In terms of nonlinear effects both the study of second and third harmonic generation (THG) would be of great interest. The Born-Kuhn model should be easily extendable to include nonlinear potential terms such that chiral THG is correctly modeled. In the case of second harmonic generation (SHG), the effects of chirality are even more

interesting since the occurrence of SHG is conditional on the absence of centrosymmetry.

Furthermore, a simple magnetochiral system can be envisioned as incorporating a magnetic material such as EuS or EuSe as spacer layer between the nanorods of the chiral dimer. This would allow for full mathematical treatment of a difficult higher order problem.

Additionally, it is of great interest to numerically and experimentally study differences between the one- and two-electron models of optical activity. It is predicted that the one-electron model exhibits both CD and ORD responses that scale with the power of the incident light [285]. Therefore, it has been pointed out in literature that macroscopically only the two-electron configuration creates intrinsic optical activity that is a pure property of the structure itself.

Finally, we successfully integrated homogeneous chiral media into a commercial FEM solver. Sanity checks that compared numerically calculated simple geometries involving chiral media with analytic results showed excellent agreement. Using this tool, we studied the canonical achiral and chiral structures that are prime candidates for PECD. We found a purely electromagnetic enhancement of 3 orders of magnitude that mainly stems from chiral media induced chirality in the metallic structures. Furthermore, our calculations revealed that hot-spots at plasmonic structures are the main factor in PECD. Moreover, we saw that the coplanarity of the incident circularly polarized light with the resonantly enhanced field vector plays a crucial role. We hypothesize due to these results that higher experimentally reported values for PECD [151] are due to chemical or alignment effects, which were not accounted for in our study. Here, future work should incorporate anisotropic chiral media, in order to investigate such alignment effects. Additionally, so far we have only studied basic geometries and it is of great interest to carry out the rigorous analysis for more complex structures such as swastikkas and helices.

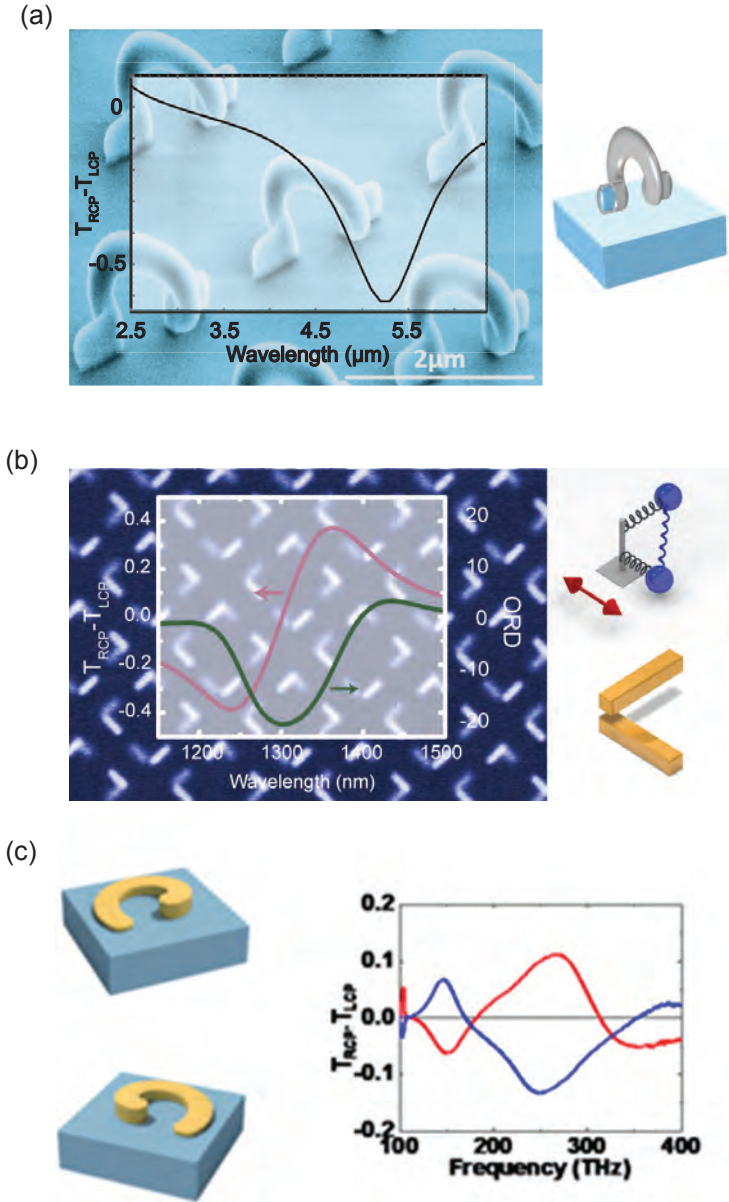


FIGURE 9.3. Various realized chiral plasmonic systems: (a) plasmonic equivalent of the one-electron model (b) plasmonic equivalent of the two-electron model (c) spiral-ramp structure

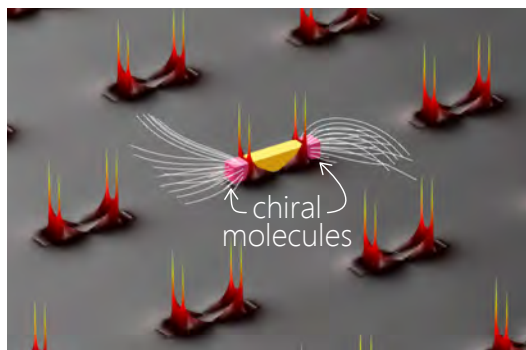


FIGURE 9.4. Plasmon-enhanced CD setup.

DETAILS OF THE NUMERICAL STUDY OF HYBRID PLASMON-CHIRAL MEDIA SYSTEMS

A.0.1 *Determining realistic Simulation Parameters*

The numerical results in Section 8.2 have been calculated using a Lorentzian type model for the permittivity ε and Pasteur parameter κ , while $\mu = 1$ and $\chi = 0$:

$$\varepsilon = \varepsilon_b - \gamma\rho(\omega) , \quad (\text{A.1})$$

$$\kappa = \beta\rho(\omega) , \quad (\text{A.2})$$

$$\rho(\omega) = \frac{1}{h\omega - h\omega_0 - i\Gamma} - \frac{1}{h\omega + h\omega_0 + i\Gamma} , \quad (\text{A.3})$$

where ε_b is the background permittivity.

The coefficients γ and β determine the magnitude of absorptive and chiral properties. The resonance frequency is described by ω_0 , the corresponding wavelength of the molecular resonance can be calculated as $\lambda_0 = 2\pi c/\omega_0$. The damping factor Γ defines the molecular resonance broadening. Exemplarily, Fig. A.1 shows the permittivity ε and Pasteur parameter κ as well as the absorption and CD signal for a 40 nm thin slab in air using realistic chiral medium parameter values. The resonance wavelength is at $\lambda_0 = 190$ nm with a peak value of $\Re e(\kappa) = 3 \times 10^{-8}$, $\Gamma = 0.1$ eV, and peak absorption characterized by $\varepsilon'' = 1.4 \times 10^{-3}$. The background dielectric constant is $\varepsilon_b = 1.33^2$. The resulting amplitudes are $\gamma = 1.4 \cdot 10^{-5}$ eV and $\beta = 3 \cdot 10^{-9}$ eV.

The calculated CD signal for the system of chiral patches with plasmonic particles is at the edge of the numerical accuracy for the parameters specified above with reasonable computational resources. More specifically, since the circular dichroism signal of the chiral medium is weak in the visible and infrared spectral regions, the numerical analysis requires extremely high precision to reduce the numerical noise below the chiral medium signal. Therefore, only the spectra in Fig. 8.4

of the main text are calculated with the above mentioned realistic parameters for the chiral medium, and demonstrate the absolute values of the absorption and CD signals. For the other figures, we have increased the chirality parameter artificially to maintain reasonable computational time. The chirality parameter κ has been scaled up by a factor of $2 \cdot 10^5$, and the dielectric constant has been adjusted accordingly, by increasing the amplitude γ by a factor of $5 \cdot 10^3$, to ensure energy conservation. Careful analysis reveals that the enhancement factor is not affected by these changes, indicating that the CD enhancement does not depend on the magnitude of the Pasteur parameter κ in the investigated parameter range.

A.o.2 *Baseline Corrected CD-Enhancement Factors*

The chiral nanostructures exhibit a CD response by themselves without chiral medium patches in the surrounding. However, we are primarily interested in the enhancement of the CD signal of the chiral medium meaning that the nanostructure CD poses unwanted noise. Therefore, we carry out a baseline correction to remove this part of the signal. The baseline corrected CD spectra then provide the CD signal of the chiral medium in order to calculate enhancement factors. The details of the procedure are described here for a chiral plasmonic dimer array (see inset in Fig. A.2) with gold rods of dimensions $40 \text{ nm} \times 40 \text{ nm} \times 150 \text{ nm}$, a gap distance of 40 nm and a square unit cell of $500 \text{ nm} \times 500 \text{ nm}$. The gold rods are surrounded by air.

The FEM analysis provides absorption spectra for RCP and LCP incident light denoted as A_{RCP} and A_{LCP} (Fig. A.2). The corresponding CD signal of the chiral plasmonic dimer is calculated as $A_{\text{RCP}} - A_{\text{LCP}}$ and shows a bi-signate lineshape (Fig. A.2(b)). The chiral patches in the hot-spots of the electromagnetic fields modify the CD spectra for left- and right-handed media with respect to the racemic mixture, as shown in Fig. A.2(c). Racemic mixtures are solutions with equal amounts of left- and right-handed molecules. Therefore, they exhibit no CD response and serve as reference signals. In other words, Fig. A.2(c) demonstrates the CD spectra for the three configurations: The plasmonic particle with left/right-handed medium is shown by solid/dashed orange lines, and the black line denotes the plasmonic

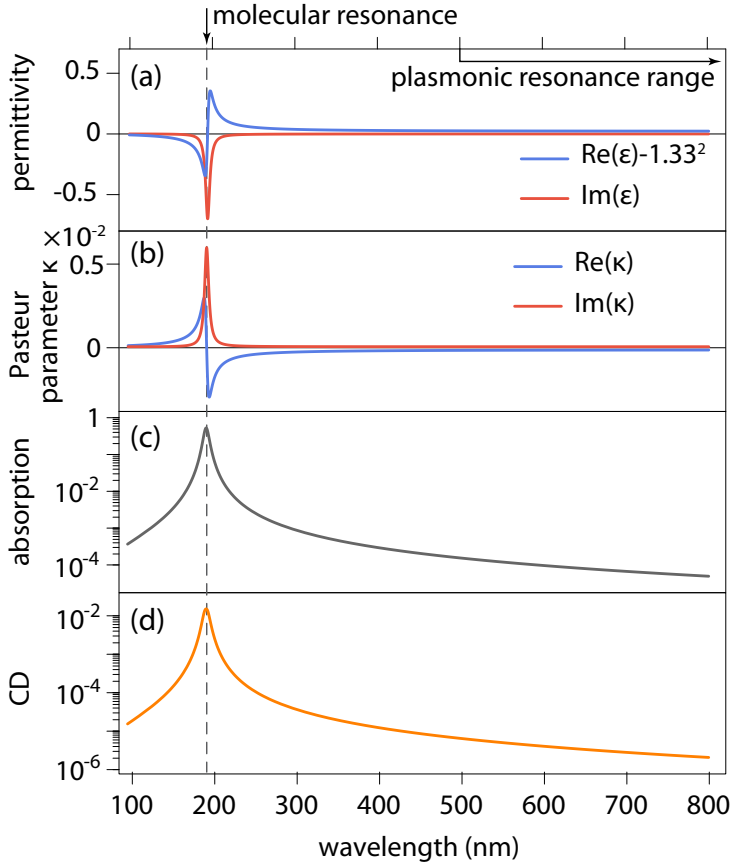


FIGURE A.1. Dispersion of material parameters used for the chiral patches, which have been calculated by Eq. (A.3) for the chiral medium with artificially increased chirality parameter κ , and accordingly adjusted amplitude γ , see supplementary text. (a) Real and imaginary parts of the dielectric permittivity. (b) Real and imaginary parts of the chirality parameter κ . (c) Absorption and (d) CD spectra of a 40 nm layer of chiral medium surrounded by vacuum. The vertical red dashed line shows the molecular resonance position.

particle with racemic mixture in the hot-spots. As we are interested in the response of the chiral patches themselves, we subtract the signal

of the nanoparticle with racemic mixture from the other two curves. In doing so, we obtain the baseline corrected signal, see Fig. A.2(d). In the next step, the CD enhancement factor is calculated as the ratio between the absolute values of the baseline corrected signal and the CD signal of the chiral medium itself without the plasmonic structure Fig. A.2(e). Note that the baseline corrected curves are symmetric, so that the enhancement factor curves are the same for the left- and right-handed chiral medium. The described workflow is applicable to arbitrarily shaped plasmonic nanoparticles.

A.1 LOSS DECOMPOSITION

To obtain a better understanding of the origin of the observed CD enhancement, we provide here the results of the spatial loss decomposition by calculating absorption in the metal and chiral media separately for two different configurations: The rod antenna and the plasmonic chiral dimer (cf. Fig. S3). The rod antenna is geometrically achiral and shows no CD signal without chiral medium patches. As seen in Fig. A.3(c), the compound system with chiral medium patches in the hot spots of the rod antenna generates a CD signal that peaks at the spectral position of the plasmonic resonance of the rod antenna. When evaluating the absorption difference between LCP and RCP incident light only in the region of the chiral medium patches, the resulting values at the plasmonic resonance are two orders of magnitude smaller than the total CD. Hence, the enhanced CD signal at the plasmonic resonance originates mainly from the so-called induced CD [160] in the achiral metal antenna, and not from an increased absorption in the chiral medium patches due to the large field enhancement in the hot-spots.

The plasmonic chiral dimer exhibits similar loss decomposition: The CD signal originating from losses in metal dominates over the CD signal from the losses in the chiral medium patches at the position of the plasmonic resonances, see Fig. A.3 (e,f). Note that the chiral plasmonic dimer provides an intrinsic CD signal without the chiral medium patches, so that we used the baseline correction procedure described in Appendix A.0.2 to extract the influence of the

chiral medium patches on the CD signal. For the near-fields of both structures, we can evaluate the so-called local optical chirality

$$C = -0.5\epsilon_0\omega \Im m(\mathbf{E}^* \cdot \mathbf{B}), \quad (\text{A.4})$$

[155], which is an important quantity to describe the difference in excitation rates of the different enantiomers of chiral molecules. It has been shown that plasmonic nanostructures illuminated with circularly polarized light can exhibit near-fields with enhanced optical chirality compared to the incident light [154]. This effect is expected to contribute to plasmon-enhanced CD in the chiral patches. The local optical chirality (calculated in the absence of the chiral medium patches) of single rod antenna as well as the chiral dimer configuration is depicted in Fig. A.3 (a,d). Note that we plot normalized values $\hat{C} = C/C_{\text{CPL}}$, where C_{CPL} denotes the optical chirality of circularly polarized light at the same frequency. This quantity describes the enhancement of optical chirality compared to the incident circular polarization. One can identify regions with different handedness denoted by red and blue colors, which correspond to positive and negative signs of \hat{C} , respectively. For the achiral rod antenna, parts with positive and negative optical chirality partially cancel each other in the area of the chiral patches due to the symmetry of the structure [A5]. The situation is different in the chiral dimer configuration. However, the absolute values of optical chirality enhancement are rather small. This indicates, together with our finding that induced CD dominates the total signal, that optical chirality has only a minor effect for the enhanced CD signals observed in the systems analyzed in this investigation. A detailed analysis of systems optimized for strong optical chirality enhancement is beyond the scope of our work.

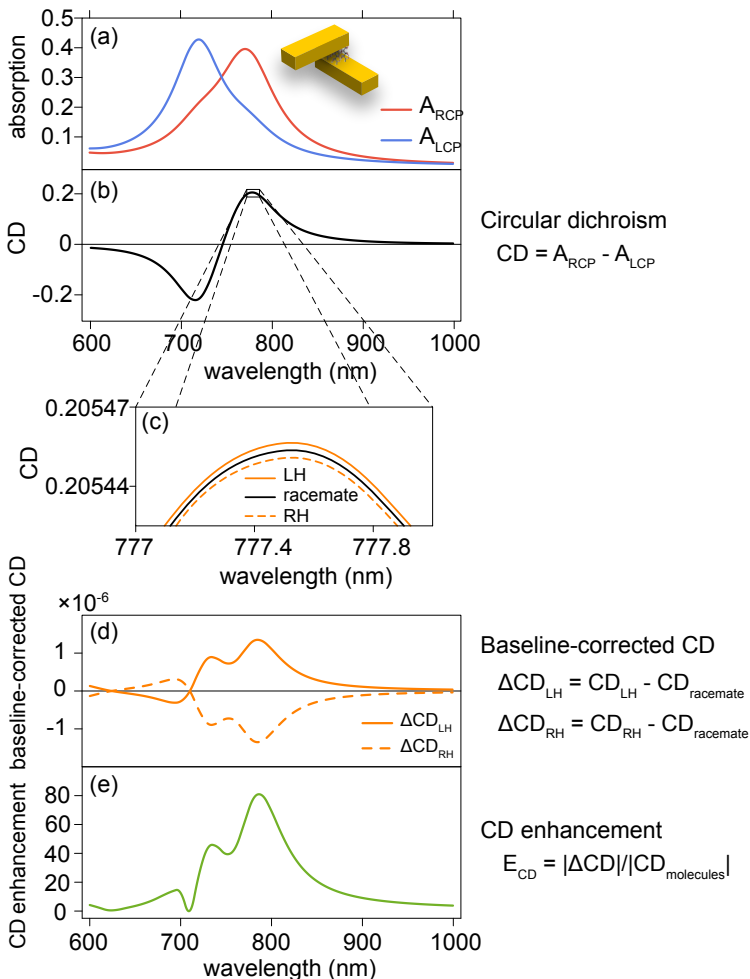


FIGURE A.2. Derivation of the baseline corrected CD signal enhancement factor. (a) Absorption curves of a chiral plasmonic nanoparticle array for right and left circular polarized normally incident light. The inset shows a schematic of the geometry. (b) CD signal of the chiral plasmonic nanoparticle. (c) CD signal of the chiral plasmonic nanoparticle with left-handed medium (solid red line), right-handed medium (dashed red line), and racemic mixture (solid black line in the middle) in the hot-spots. (d) Baseline corrected CD signal of the chiral medium enhanced by the plasmonic nanoparticle. (e) CD signal enhancement factor.

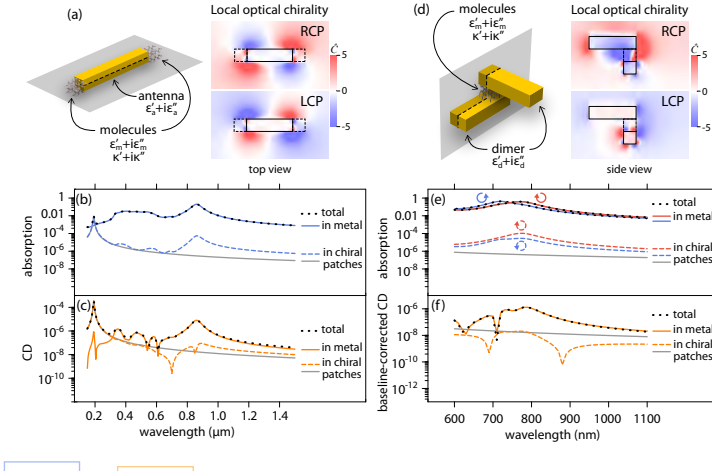


FIGURE A.3. Origin of molecular CD enhancement for achiral rod-antenna (left panels) and chiral plasmonic dimer (right panels). (a/d) Local optical chirality normalized to circularly polarized light. (b/e) Total losses (black dots) as well as losses in metal (solid lines) and chiral patches (dashed lines). In panel (e), red/blue color denotes right/left circularly polarized incident light. (c/f) Total CD (black dots), induced CD (solid orange lines) as well as CD in chiral patches (dashed orange lines). Note that panel (f) shows the baseline corrected CD signal. Gray curves indicate the signals from chiral medium patches without the plasmonic structures.

BIBLIOGRAPHY

- [1] A. Sommerfeld: *Über die Fortpflanzung elektrodynamischer Wellen längs eines Drahtes*. Annalen der Physik **303**, 233–290 (1899).
Cit. on p. 1.
- [2] J. Zenneck: *Über die Fortpflanzung ebener elektromagnetischer Wellen längs einer ebenen Leiterfläche und ihre Beziehung zur drahtlosen Telegraphie*. Annalen der Physik **328**, 846–866 (1907).
Cit. on p. 1.
- [3] R. Wood: *On a remarkable case of uneven distribution of light in a diffraction grating spectrum*. Proceedings of the Physical Society of London (1902).
Cit. on p. 1.
- [4] U. Fano: *The theory of anomalous diffraction gratings and of quasi-stationary waves on metallic surfaces (Sommerfeld's waves)*. Journal Of The Optical Society Of America **31**, 213–222 (1941).
Cit. on p. 1.
- [5] U. Fano: *Atomic Theory of Electromagnetic Interactions in Dense Materials*. Physical Review **103**, 1202–1218 (1956).
Cit. on p. 1.
- [6] R. H. Ritchie, E. T. Arakawa, J. J. Cowan, and R. N. Hamm: *Surface-Plasmon Resonance Effect in Grating Diffraction*. Physical review letters **21**, 1530–1533 (1968).
Cit. on p. 1.
- [7] K. E and H. Raether: *Radiative Decay of Non Radiative Surface Plasmons Excited by Light*. Zeitschrift für Naturforschung Part A-Astrophysik Physik Und Physikalische Chemie **A 23**, 2135 (1968).
Cit. on p. 1.

- [8] A. Otto: *Excitation of nonradiative surface plasma waves in silver by the method of frustrated total reflection*. Zeitschrift Fur Physik **216**, 398–410 (1968).
Cit. on p. 1.
- [9] M. Faraday: *The Bakerian lecture: experimental relations of gold (and other metals) to light*. Philosophical Transactions of the Royal Society **147**, 145–181 (1857).
Cit. on p. 1.
- [10] H. Siedentopf and R. Zsigmondy: *Über Sichtbarmachung und Größenbestimmung ultramikroskopischer Teilchen, mit besonderer Anwendung auf Goldrubingläser*. Annalen der Physik **315**, 1–39 (1902).
Cit. on p. 1.
- [11] J. Garnett: *Colours in metal glasses and in metallic films*. Philosophical Transactions of the Royal Society of London Series a-Containing Papers of a Mathematical or Physical Character **203**, 385–420 (1904).
Cit. on p. 1.
- [12] G. Mie: *Beiträge zur Optik trüber Medien, speziell kolloidaler Metallösungen*. Annalen der Physik **25**, 377–445 (1908).
Cit. on p. 1.
- [13] J. A. Schuller, E. S. Barnard, W. Cai, Y. C. Jun, J. S. White, and M. L. Brongersma: *Plasmonics for extreme light concentration and manipulation*. Nature Materials **9**, 193–204 (2010).
DOI 10.1038/nmat2630, cit. on p. 2.
- [14] J. Valentine, S. Zhang, T. Zentgraf, E. Ulin-Avila, D. A. Genov, G. Bartal, and X. Zhang: *Three-dimensional optical metamaterial with a negative refractive index*. Nature **455**, 376–379 (2008).
DOI 10.1038/nature07247, cit. on p. 2.
- [15] J. Yao, Z. Liu, Y. Liu, Y. Wang, C. Sun, G. Bartal, A. M. Stacy, and X. Zhang: *Optical negative refraction in bulk metamaterials of nanowires*. Science **321**, 930–930 (2008).
DOI 10.1126/science.1157566, cit. on p. 2.

- [16] D. Smith, J. Pendry, and M. Wiltshire: *Metamaterials and negative refractive index*. *Science* **305**, 788–792 (2004).
Cit. on pp. 2, 66.
- [17] N. Liu, M. Mesch, T. Weiss, M. Hentschel, and H. Giessen: *Infrared Perfect Absorber and Its Application As Plasmonic Sensor*. *Nano Letters* **10**, 2342–2348 (2010).
DOI 10.1021/nl9041033, cit. on p. 2.
- [18] J. K. Gansel, M. Thiel, M. S. Rill, M. Decker, K. Bade, V. Saile, G. Von Freymann, S. Linden, and M. Wegener: *Gold Helix Photonic Metamaterial as Broadband Circular Polarizer*. *Science* **325**, 1513–1515 (2009).
DOI 10.1126/science.1177031, cit. on pp. 2, 57, 71, 110.
- [19] M. Kauranen and A. V. Zayats: *Nonlinear plasmonics*. *Nature Photonics* **6**, 737–748 (2012).
DOI 10.1038/nphoton.2012.244, cit. on p. 2.
- [20] E. C. Le Ru and P. G. Etchegoin: *Single-Molecule Surface-Enhanced Raman Spectroscopy*. dx.doi.org **63**, 65–87 (2012).
DOI 10.1146/annurev-physchem-032511-143757, cit. on p. 2.
- [21] M. Hentschel, M. Saliba, R. Vogelgesang, H. Giessen, A. P. Alivisatos, and N. Liu: *Transition from Isolated to Collective Modes in Plasmonic Oligomers*. *Nano Letters* **10**, 2721–2726 (2010).
Cit. on pp. 2, 24.
- [22] A. Radke, T. Gissibl, T. Klotzbücher, P. V. Braun, and H. Giessen: *Three-Dimensional Bichiral Plasmonic Crystals Fabricated by Direct Laser Writing and Electroless Silver Plating*. *Adv. Mater.* **23**, 3018–3021 (2011).
DOI 10.1002/adma.201100543, cit. on pp. 2, 57.
- [23] H. Lezec, A. Degiron, E. Devaux, R. Linke, L. Martin-Moreno, F. Garcia-Vidal, and T. W. Ebbesen: *Beaming light from a subwavelength aperture*. *Science* **297**, 820–822 (2002).
DOI 10.1126/science.1071895, cit. on p. 2.

- [24] J. A. Fan, C. Wu, K. Bao, J. Bao, R. Bardhan, N. J. Halas, V. N. Manoharan, P. Nordlander, G. Shvets, and F. Capasso: *Self-Assembled Plasmonic Nanoparticle Clusters*. *Science* **328**, 1135–1138 (2010).
Cit. on pp. 2, 24.
- [25] S. Lal, S. Link, and N. J. Halas: *Nano-optics from sensing to waveguiding*. *Nature Photonics* **1**, 641–648 (2007).
DOI 10.1038/nphoton.2007.223, cit. on p. 2.
- [26] J. D. Jackson: *Classical Electrodynamics Third Edition*, 3 edition, Wiley, 1998.
Cit. on pp. 5, 6, 8, 24.
- [27] M. Besbes, B. Ionesco, Z. Ren, and A. Razek: *Study of Magnetoelastic Problems by Strong Coupling Model*. In: *Electric and Magnetic Fields*, Springer US (Boston, MA), 1995.
Cit. on p. 5.
- [28] G. Russakoff: *A derivation of the macroscopic Maxwell equations*. *American Journal Of Physics* (1970).
Cit. on p. 5.
- [29] D. J. Griffiths: *Introduction to Electrodynamics (3rd Edition)*, 3rd edition, Benjamin Cummings, 1999.
Cit. on p. 10.
- [30] M. Born and E. Wolf: *Principles of Optics*, 7 edition, Cambridge University Press, 1999.
Cit. on pp. 11, 37.
- [31] S. A. Maier: *Plasmonics: Fundamentals and Applications*, 1 edition, Springer, 2007.
Cit. on pp. 12, 84, 115.
- [32] A. M. Fox: *Optical Properties of Solids*, Oxford University Press, USA, 2001.
Cit. on pp. 12, 19.
- [33] L. Novotny and B. Hecht: *Principles of Nano-Optics*, Cambridge University Press, 2012.
Cit. on p. 12.

- [34] M. Dressel and G. Grüner: *Electrodynamics of Solids*. Optical Properties of Electrons in Matter, Cambridge University Press, 2002.
Cit. on p. 12.
- [35] E. D. Palik: *Handbook of Optical Constants of Solids*, Academic Press, 2012.
Cit. on pp. 13, 14.
- [36] R. H. Ritchie: *Plasma Losses by Fast Electrons in Thin Films*. Physical Review **106**, 874–881 (1957).
Cit. on p. 15.
- [37] J. Homola and M. Piliarik: *Surface Plasmon Resonance (SPR) Sensors*. Springer Series on Chemical Sensors and Biosensors, 1 edition, Springer, 2006.
Cit. on pp. 17, 110.
- [38] C. Bohren and D. Huffmann: *Absorption and Scattering of Light by Small Particles*, 1st edition, Wiley-VCH, 1983.
Cit. on pp. 20, 21.
- [39] U. Kreibig and M. Vollmer: *Optical properties of metal clusters*, Springer, 1995.
Cit. on p. 20.
- [40] C. A. Balanis: *Antenna Theory. Analysis and Design*, John Wiley & Sons, 2015.
Cit. on p. 22.
- [41] L. Novotny: *Effective Wavelength Scaling for Optical Antennas*. Physical Review Letters **98**, 266802 (2007).
Cit. on p. 22.
- [42] E. S. Barnard, J. S. White, A. Chandran, and M. L. Brongersma: *Spectral properties of plasmonic resonator antennas*. Optics Express **16**, 16529–16537 (2008).
Cit. on p. 22.
- [43] J. Dorfmueller, R. Vogelgesang, R. T. Weitz, C. Rockstuhl, C. Etrich, T. Pertsch, F. Lederer, and K. Kern: *Fabry-Perot Resonances in One-Dimensional Plasmonic Nanostructures*. Nano Letters **9**, 2372–2377 (2009).
Cit. on p. 22.

- [44] R. Gordon: *Light in a subwavelength slit in a metal: Propagation and reflection*. Physical Review B **73**, 153405 (2006).
Cit. on p. 22.
- [45] K. B. Crozier, A. Sundaramurthy, G. Kino, and C. Quate: *Optical antennas: Resonators for local field enhancement*. Journal of Applied Physics **94**, 4632–4642 (2003).
Cit. on p. 22.
- [46] E. Prodan and P. Nordlander: *Structural Tunability of the Plasmon Resonances in Metallic Nanoshells*. Nano Letters **3**, 543–547 (2003).
Cit. on p. 24.
- [47] E. Prodan, P. Nordlander, and N. J. Halas: *Electronic Structure and Optical Properties of Gold Nanoshells*. Nano Letters (2003).
DOI 10.1021/nl1034594q, cit. on p. 24.
- [48] E. Prodan, C. Radloff, N. Halas, and P. Nordlander: *A hybridization model for the plasmon response of complex nanostructures*. Science **302**, 419–422 (2003).
Cit. on pp. 24, 85, 104.
- [49] S. S. Acimovic, M. P. Kreuzer, M. U. Gonzalez, and R. Quidant: *Plasmon Near-Field Coupling in Metal Dimers as a Step toward Single-Molecule Sensing*. ACS nano **3**, 1231–1237 (2009).
Cit. on p. 24.
- [50] D. N. Chigrin, C. Kremers, and S. V. Zhukovsky: *Plasmonic nanoparticle monomers and dimers: from nanoantennas to chiral metamaterials*. Applied Physics B-Lasers And Optics **105**, 81–97 (2011).
Cit. on p. 24.
- [51] P. Nordlander, C. Oubre, E. Prodan, K. Li, and M. I. Stockman: *Plasmon Hybridization in Nanoparticle Dimers*. Nano Letters **4**, 899–903 (2004).
Cit. on pp. 24, 85.

- [52] A. M. Funston, C. Novo, T. J. Davis, and P. Mulvaney: *Plasmon Coupling of Gold Nanorods at Short Distances and in Different Geometries*. *Nano Letters* **9**, 1651–1658 (2009).
Cit. on p. 24.
- [53] F. J. Garcia de Abajo: *Nonlocal Effects in the Plasmons of Strongly Interacting Nanoparticles, Dimers, and Waveguides*. *Journal Of Physical Chemistry C* **112**, 17983–17987 (2008).
Cit. on p. 24.
- [54] S. M. Hein and H. Giessen: *Retardation-induced phase singularities in coupled plasmonic oscillators*. *Physical Review B* **91**, 205402 (2015).
Cit. on p. 24.
- [55] N. Liu, H. Liu, S. Zhu, and H. Giessen: *Stereometamaterials*. *Nature Photonics* **3**, 157–162 (2009).
Cit. on p. 24.
- [56] A. Mikhailovsky, M. Petruska, K. Li, M. I. Stockmann, and V. Klimov: *Phase-sensitive spectroscopy of surface plasmons in individual metal nanostructures*. *Physical Review B* **69**, 085401 (2004).
Cit. on p. 24.
- [57] O. L. Muskens, V. Giannini, J. A. Sanchez-Gil, and J. G. Rivas: *Optical scattering resonances of single and coupled dimer plasmonic nanoantennas*. *Optics Express* **15**, 17736–17746 (2007).
Cit. on p. 24.
- [58] P. K. Jain, S. Eustis, El-Sayed, and M. A.: *Plasmon Coupling in Nanorod Assemblies: Optical Absorption, Discrete Dipole Approximation Simulation, and Exciton-Coupling Model*, American Chemical Society, 2006.
Cit. on p. 24.
- [59] B. Willingham, D. W. Brandl, and P. Nordlander: *Plasmon hybridization in nanorod dimers*. *Applied Physics B* **93**, 209–216 (2008).
Cit. on p. 24.

- [60] S.-C. Yang, H. Kobori, C.-L. He, M.-H. Lin, H.-Y. Chen, C. Li, M. Kanehara, T. Teranishi, and S. Gwo: *Plasmon Hybridization in individual Gold Nanocrystal Dimers: Direct Observation of Bright and Dark Modes*. *Nano Letters* **10**, 632–637 (2010).
Cit. on p. 24.
- [61] C. Sönnichsen, B. M. Reinhard, J. Liphardt, and A. P. Alivisatos: *A molecular ruler based on plasmon coupling of single gold and silver nanoparticles*. *Nature Biotechnology* **23**, 741–745 (2005).
DOI 10.1038/nbt1100, cit. on pp. 24, 93.
- [62] L. Chuntonov and G. Haran: *Effect of Symmetry Breaking on the Mode Structure of Trimeric Plasmonic Molecules*. *Journal Of Physical Chemistry C* **115**, 19488–19495 (2011).
Cit. on p. 24.
- [63] A. M. Funston, T. J. Davis, C. Novo, and P. Mulvaney: *Coupling modes of gold trimer superstructures*. *Philosophical Transactions of the Royal Society a-Mathematical Physical and Engineering Sciences* **369**, 3472–3482 (2011).
Cit. on p. 24.
- [64] V. Giannini and J. A. Sanchez-Gil: *Excitation and emission enhancement of single molecule fluorescence through multiple surface-plasmon resonances on metal trimer nanoantennas*. *Optics Letters* **33**, 899–901 (2008).
Cit. on p. 24.
- [65] H. Lee, G.-H. Kim, J.-H. Lee, N. H. Kim, J.-M. Nam, and Y. D. Suh: *Quantitative Plasmon Mode and Surface-Enhanced Raman Scattering Analyses of Strongly Coupled Plasmonic Nanotrimers with Diverse Geometries*. *Nano Letters* **15**, 4628–4636 (2015).
Cit. on p. 24.
- [66] T. Shegai, Z. Li, T. Dadoosh, Z. Zhang, H. Xu, and G. Haran: *Managing light polarization via plasmon-molecule interactions within an asymmetric metal nanoparticle trimer*. *Proceedings of the National Academy of Sciences* **105**, 16448–16453 (2008).
Cit. on p. 24.

- [67] S. N. Sheikholeslami, A. Garcia-Etxarri, and J. A. Dionne: *Controlling the Interplay of Electric and Magnetic Modes via Fano-like Plasmon Resonances*. *Nano Letters* **11**, 3927–3934 (2011).
Cit. on p. 24.
- [68] Y. Tao, L. Shao, Q. Ruan, and J. Wang: *Magnetic plasmon modes in Au nanorod trimer arrays*. Abstracts of Papers of the American Chemical Society **247** (2014).
Cit. on p. 24.
- [69] H. Wang, Z. Li, H. Zhang, P. Wang, and S. Wen: *Giant local circular dichroism within an asymmetric plasmonic nanoparticle trimer*. *Scientific Reports* **5**, 8207–6 (2015).
Cit. on p. 24.
- [70] R. Watanabe-Tamaki, A. Ishikawa, T. Tanaka, T. Zako, and M. Maeda: *DNA-Templating Mass Production of Gold Trimer Rings for Optical Metamaterials*. *Journal Of Physical Chemistry C* **116**, 15028–15033 (2012).
Cit. on p. 24.
- [71] D. W. Brandl, N. A. Mirin, and P. Nordlander: *Plasmon Modes of Nanosphere Trimers and Quadrumers*, American Chemical Society, 2006.
Cit. on p. 24.
- [72] J. A. Fan, K. Bao, C. Wu, J. Bao, R. Bardhan, N. J. Halas, V. N. Manoharan, G. Shvets, P. Nordlander, and F. Capasso: *Fano-like Interference in Self-Assembled Plasmonic Oquadramer Clusters*. *Nano Letters* **10**, 4680–4685 (2010).
Cit. on p. 24.
- [73] F. Shafiei, F. Monticone, K. Q. Le, X.-X. Liu, T. Hartsfield, Al \bar{A} [†], and X. Li: *A subwavelength plasmonic metamolecule exhibiting magnetic-based optical Fano resonance*. *Nature Nanotechnology* **8**, 95–99 (2013).
Cit. on p. 24.
- [74] Y. Zhan, D. Y. Lei, X. Li, and S. A. Maier: *Plasmonic Fano resonances in nanohole quadrumers for ultra-sensitive refractive index sensing*. *Nanoscale* **6**, 4705–4715 (2014).
Cit. on p. 24.

- [75] D. Dregely, M. Hentschel, and H. Giessen: *Excitation and Tuning of Higher-Order Fano Resonances in Plasmonic Oligomer Clusters*. ACS nano **5**, 8202–8211 (2011).
Cit. on p. 24.
- [76] M. Hentschel, D. Dregely, R. Vogelgesang, H. Giessen, and N. Liu: *Plasmonic Oligomers: The Role of Individual Particles in Collective Behavior*. ACS nano **5**, 2042–2050 (2011).
Cit. on p. 24.
- [77] R. Ogier, Y. Fang, M. Svedendahl, P. Johansson, and M. Kall: *Macroscopic Layers of Chiral Plasmonic Nanoparticle Oligomers from Colloidal Lithography*. ACS Photonics **1**, 1074–1081 (2014).
Cit. on p. 24.
- [78] M. Rahmani, B. Lukiyanchuk, T. T. V. Nguyen, T. Tahmasebi, Y. Lin, T. Y. F. Liew, and M. H. Hong: *Influence of symmetry breaking in pentamers on Fano resonance and near-field energy localization*. Optical Materials Express **1**, 1409–1415 (2011).
Cit. on p. 24.
- [79] M. Rahmani, B. Lukiyanchuk, T. Tahmasebi, Y. Lin, T. Y. F. Liew, and M. H. Hong: *Polarization-controlled spatial localization of near-field energy in planar symmetric coupled oligomers*. Applied Physics A **107**, 23–30 (2011).
Cit. on p. 24.
- [80] N. Liu and H. Giessen: *Coupling Effects in Optical Metamaterials*. Angewandte Chemie-International Edition **49**, 9838–9852 (2010).
Cit. on pp. 24, 84.
- [81] B. Metzger: *Ultrafast nonlinear plasmonics : from dipole nanoantennas to hybrid complex plasmonic structures*, 2014.
Cit. on p. 25.
- [82] W. Demtröder: *Experimentalphysik 3*, 2005, 4 edition, Springer, 2010.
Cit. on p. 25.

- [83] V. Myroshnychenko, J. Rodriguez-Fernandez, I. Pastoriza-Santos, A. M. Funston, C. Novo, P. Mulvaney, L. M. Liz Marzan, and F. J. Garcia de Abajo: *Modelling the optical response of gold nanoparticles*. Chemical Society Reviews **37**, 1792 (2008).
Cit. on p. 26.
- [84] D. Morin: *Introduction to Classical Mechanics. With Problems and Solutions*, Cambridge University Press, 2008.
Cit. on p. 26.
- [85] D. J. Morin: *Problems and Solutions in Introductory Mechanics*, CreateSpace, 2014.
Cit. on pp. 26, 27.
- [86] N. I. Zheludev and Y. S. Kivshar: *From metamaterials to metadevices*. Nature Materials **11**, 917–924 (2012).
DOI 10.1038/NMAT3431, cit. on p. 27.
- [87] I. M. Pryce, K. Aydin, Y. A. Kelaita, R. M. Briggs, and H. A. Atwater: *Highly Strained Compliant Optical Metamaterials with Large Frequency Tunability*. Nano Letters **10**, 4222–4227 (2010).
DOI 10.1021/n1102684x, cit. on p. 27.
- [88] J. Y. Ou, E. Plum, L. Jiang, and N. I. Zheludev: *Reconfigurable Photonic Metamaterials*. Nano Letters **11**, 2142–2144 (2011).
DOI 10.1021/n1200791r, cit. on p. 27.
- [89] Y. Yao, M. A. Kats, P. Genevet, N. Yu, Y. Song, J. Kong, and F. Capasso: *Broad Electrical Tuning of Graphene-Loaded Plasmonic Antennas*. Nano Letters **13**, 1257–1264 (2013).
DOI 10.1021/n13047943, cit. on p. 27.
- [90] Y. Yao, M. A. Kats, R. Shankar, Y. Song, J. Kong, M. Loncar, and F. Capasso: *Wide Wavelength Tuning of Optical Antennas on Graphene with Nanosecond Response Time*. Nano Letters **14**, 214–219 (2014).
DOI 10.1021/n1403751p, cit. on p. 27.

- [91] Z. Fang, Y. Wang, A. E. Schlather, Z. Liu, P. M. Ajayan, F. J. G. de Abajo, P. Nordlander, X. Zhu, and N. J. Halas: *Active tunable absorption enhancement with graphene nanodisk arrays*. *Nano Letters* **14**, 299–304 (2014). DOI 10.1021/nl404042h, cit. on p. 27.
- [92] N. Papisimakis, Z. Luo, Z. X. Shen, F. De Angelis, E. Di Fabrizio, A. E. Nikolaenko, and N. I. Zheludev: *Graphene in a photonic metamaterial*. *Optics Express* **18**, 8353–8359 (2010). DOI 10.1364/OE.18.008353, cit. on p. 27.
- [93] H.-T. Chen, W. J. Padilla, J. M. O. Zide, A. C. Gossard, A. J. Taylor, and R. D. Averitt: *Active terahertz metamaterial devices*. *Nature* **444**, 597–600 (2006). DOI 10.1038/nature05343, cit. on p. 27.
- [94] W. J. Padilla, A. J. Taylor, C. Highstrete, M. Lee, and R. D. Averitt: *Dynamical electric and magnetic metamaterial response at terahertz frequencies*. **96**, 107401–107401 (2006). DOI 10.1103/physrevlett.96.107401, cit. on p. 27.
- [95] H.-T. Chen, J. F. O’Hara, A. K. Azad, A. J. Taylor, R. D. Averitt, D. B. Shrekenhamer, and W. J. Padilla: *Experimental demonstration of frequency-agile terahertz metamaterials*. *Nature Photonics* **2**, 295–298 (2008). DOI 10.1038/nphoton.2008.52, cit. on p. 27.
- [96] H. Tao, A. C. Strikwerda, K. Fan, W. J. Padilla, X. Zhang, and R. D. Averitt: *Reconfigurable terahertz metamaterials*. **103**, 147401–147401 (2009). DOI 10.1103/PhysRevLett.103.147401, cit. on p. 27.
- [97] J. M. Luther, P. K. Jain, T. Ewers, and A. P. Alivisatos: *Localized surface plasmon resonances arising from free carriers in doped quantum dots*. *Nature Materials* **10**, 361–366 (2011). DOI 10.1038/nmat3004, cit. on p. 27.

- [98] M. A. Kats, R. Blanchard, P. Genevet, Z. Yang, M. M. Qazilbash, D. N. Basov, S. Ramanathan, and F. Capasso: *Thermal tuning of mid-infrared plasmonic antenna arrays using a phase change material*. *Optics Letters* **38**, 368–370 (2013).
Cit. on p. 27.
- [99] M. A. Kats, D. Sharma, J. Lin, P. Genevet, R. Blanchard, Z. Yang, M. M. Qazilbash, D. N. Basov, S. Ramanathan, and F. Capasso: *Ultra-thin perfect absorber employing a tunable phase change material*. *Applied Physics Letters* **101**, 221101 (2012).
DOI 10.1063/1.4767646, cit. on p. 27.
- [100] M. J. Dicken, K. Aydin, I. M. Pryce, L. A. Sweatlock, E. M. Boyd, S. Walavalkar, J. Ma, and H. A. Atwater: *Frequency tunable near-infrared metamaterials based on VO₂ phase transition*. *Optics Express* **17**, 18330–18339 (2009).
Cit. on p. 27.
- [101] S. R. C. Vivekchand, C. J. Engel, S. M. Lubin, M. G. Blaber, W. Zhou, J. Y. Suh, G. C. Schatz, and T. W. Odom: *Liquid Plasmonics: Manipulating Surface Plasmon Polaritons via Phase Transitions*. *Nano Letters* **12**, 4324–4328 (2012).
DOI 10.1021/nl302053g, cit. on p. 27.
- [102] B. Soares, F. Jonsson, and N. Zheludev: *All-Optical Phase-Change Memory in a Single Gallium Nanoparticle*. **98**, 153905–153905 (2007).
DOI 10.1103/PhysRevLett.98.153905, cit. on p. 27.
- [103] N. Strohfeldt, A. Tittl, M. Schäferling, F. Neubrech, U. Kreibig, R. Griessen, and H. Giessen: *Yttrium Hydride Nanoantennas for Active Plasmonics*. *Nano Letters* **14**, 1140–1147 (2014).
DOI 10.1021/nl403643v, cit. on p. 27.
- [104] F. Sterl, N. Strohfeldt, R. Walter, R. Griessen, A. Tittl, and H. Giessen: *Magnesium as Novel Material for Active Plasmonics in the Visible Wavelength Range*. *Nano Letters* **15**, 7949–7955 (2015).
DOI 10.1021/acs.nanolett.5b03029, cit. on p. 27.

- [105] A.-K. U. Michel, P. Zalden, D. N. Chigrin, M. Wuttig, A. M. Lindenberg, and T. Taubner: *Reversible Optical Switching of Infrared Antenna Resonances with Ultrathin Phase-Change Layers Using Femtosecond Laser Pulses*. *ACS Photonics* **1**, 833–839 (2014).
DOI 10.1021/ph500121d, cit. on pp. 28, 50, 118.
- [106] G. Bruns, P. Merkelbach, C. Schlockermann, M. Salinga, M. Wuttig, T. D. Happ, J. B. Philipp, and M. Kund: *Nanosecond switching in GeTe phase change memory cells*. *Applied Physics Letters* **95**, 043108–043108 (2009).
DOI <http://dx.doi.org/10.1063/1.3191670>, cit. on pp. 28, 50, 118.
- [107] S. Raoux and M. Wuttig: *Phase Change Materials*. Science and Applications, Springer Science & Business Media, 2010. ISBN 0387848746, cit. on pp. 28, 115.
- [108] T. Tuma, A. Pantazi, M. Le Gallo, A. Sebastian, and E. Eleftheriou: *Stochastic phase-change neurons*. *Nature Nanotechnology* **11**, 693–699 (2016).
DOI 10.1038/nnano.2016.70, cit. on p. 28.
- [109] P. Hosseini, C. D. Wright, and H. Bhaskaran: *An optoelectronic framework enabled by low-dimensional phase-change films*. *Nature* **511**, 206–211 (2014).
DOI 10.1038/nature13487, cit. on pp. 28, 50, 110.
- [110] A.-K. U. Michel, D. N. Chigrin, T. W. W. Maß, K. Schönauer, M. Salinga, M. Wuttig, and T. Taubner: *Using Low-Loss Phase-Change Materials for Mid-Infrared Antenna Resonance Tuning*. *Nano Letters* **13**, 3470–3475 (2013).
DOI 10.1021/nl4006194, cit. on pp. 29, 38, 51, 110, 113.
- [111] D. Lencer, M. Salinga, B. Grabowski, T. Hickel, J. Neugebauer, and M. Wuttig: *A map for phase-change materials*. *Nature Materials* **7**, 972–977 (2008).
DOI 10.1038/nmat2330, cit. on p. 29.
- [112] K. Shportko, S. Kremers, M. Woda, D. Lencer, J. Robertson, and M. Wuttig: *Resonant bonding in crystalline phase-change materials*. *Nature Materials* **7**, 653–658 (2008).
DOI 10.1038/nmat2226, cit. on pp. 29, 50, 114.

- [113] A. Taflove and S. C. Hagness: *Computational Electrodynamics: the FDTD method*, Artech House Boston, 2000.
Cit. on p. 32.
- [114] K. S. Yee: *Numerical Solution of Initial Boundary Value Problems Involving Maxwells Equations in Isotropic Media*. Antennas and Propagation, IEEE Transactions on **AP14**, 302 (1966).
Cit. on p. 32.
- [115] J. Berenger: *A perfectly matched layer for the absorption of electromagnetic waves*. Journal Of Computational Physics **114**, 185–200 (1994).
Cit. on p. 32.
- [116] L. Li: *Fourier modal method for crossed anisotropic gratings with arbitrary permittivity and permeability tensors*. Journal Of Optics A-Pure And Applied Optics **5**, 345–355 (2003).
Cit. on p. 33.
- [117] G. Granet: *Reformulation of the lamellar grating problem through the concept of adaptive spatial resolution*. Journal of the Optical Society of America. A, Optics, image science, and vision **16**, 2510–2516 (1999).
Cit. on p. 33.
- [118] T. Weiss, G. Granet, N. A. Gippius, S. G. Tikhodeev, and H. Giessen: *Matched coordinates and adaptive spatial resolution in the Fourier modal method*. Optics Express **17**, 8051–8061 (2009).
DOI 10.1364/OE.17.008051, cit. on pp. 33, 87, 113.
- [119] O. C. Zeinkiewicz, R. L. Taylor, and J. Z. Zhu: *The finite element method: its basis and fundamentals*, Butterworth-Heinemann, 2005.
Cit. on p. 34.
- [120] L. H. Sullivan: *The tall office building artistically considered*. Lippincott's Magazine (1896).
Cit. on p. 37.

- [121] C. Velzel: *A Course in Lens Design*. Springer Series in Optical Sciences, Springer, 2014.
Cit. on p. 37.
- [122] N. Yu, P. Genevet, M. A. Kats, F. Aieta, J.-P. Tetienne, F. Capasso, and Z. Gaburro: *Light Propagation with Phase Discontinuities: Generalized Laws of Reflection and Refraction*. *Science* **334**, 333–337 (2011).
DOI 10.1126/science.1210713, cit. on pp. 37, 40.
- [123] A. V. Kildishev, A. Boltasseva, and V. M. Shalaev: *Planar Photonics with Metasurfaces*. *Science* **339**, 1232009–1232009 (2013).
DOI 10.1126/science.1232009, cit. on p. 37.
- [124] F. Aieta, P. Genevet, M. A. Kats, N. Yu, R. Blanchard, Z. Gaburro, and F. Capasso: *Aberration-free ultrathin flat lenses and axicons at telecom wavelengths based on plasmonic metasurfaces*. *Nano Letters* **12**, 4932–4936 (2012).
DOI 10.1021/nl302516v, cit. on p. 37.
- [125] N. Yu and F. Capasso: *Flat optics with designer metasurfaces*. *Nature Materials* **13**, 139–150 (2014).
DOI 10.1038/nmat3839, cit. on p. 37.
- [126] W. Lu and S. Sridhar: *Flat lens without optical axis: Theory of imaging*. *Optics Express* **13**, 10673–10680 (2005).
DOI 10.1364/opex.13.010673, cit. on p. 37.
- [127] N. Yu, P. Genevet, F. Aieta, M. A. Kats, R. Blanchard, G. Aoust, J.-P. Tetienne, Z. Gaburro, and F. Capasso: *Flat Optics: Controlling Wavefronts With Optical Antenna Metasurfaces*. *Ieee Journal Of Selected Topics In Quantum Electronics* **19**, 4700423 (2013).
DOI 10.1109/JSTQE.2013.2241399, cit. on p. 37.
- [128] D. Lin, P. Fan, E. Hasman, and M. L. Brongersma: *Dielectric gradient metasurface optical elements*. *Science* **345**, 298–302 (2014).
DOI 10.1126/science.1253213, cit. on p. 37.

- [129] X. Chen, L. Huang, H. M.ühlenbernd, G. Li, B. Bai, Q. Tan, G. Jin, C.-W. Qiu, S. Zhang, and T. Zentgraf: *Dual-polarity plasmonic metalens for visible light*. *Nature Communications* **3**, 1198–6 (2012).
DOI 10.1038/ncomms2207, cit. on pp. 37, 47.
- [130] P. R. West, J. L. Stewart, A. V. Kildishev, V. M. Shalaev, V. V. Shkunov, F. Strohendl, Y. A. Zakharenkov, R. K. Dodds, and R. Byren: *All-dielectric subwavelength metasurface focusing lens*. *Optics Express* **22**, 26212–26221 (2014).
DOI 10.1364/OE.22.026212, cit. on p. 37.
- [131] J. P. B. Müller, K. Leosson, and F. Capasso: *Ultracompact metasurface in-line polarimeter*. *Optica* **3**, 42–47 (2016).
DOI 10.1364/OPTICA.3.000042, cit. on p. 38.
- [132] A. Pors, M. G. Nielsen, and S. I. Bozhevolnyi: *Plasmonic metagratings for simultaneous determination of Stokes parameters*. *Optica* **2**, 716–723 (2015).
DOI 10.1364/OPTICA.2.000716, cit. on p. 38.
- [133] B. Gholipour, J. Zhang, K. F. MacDonald, D. W. Hewak, and N. I. Zheludev: *An All-Optical, Non-volatile, Bidirectional, Phase-Change Meta-Switch*. *Advanced Materials* **25**, 3050–3054 (2013).
DOI 10.1002/adma.201300588, cit. on pp. 38, 114.
- [134] Q. Wang, E. T. F. Rogers, B. Gholipour, C.-M. Wang, G. Yuan, J. Teng, and N. I. Zheludev: *Optically reconfigurable metasurfaces and photonic devices based on phase change materials*. *Nature Photonics* **10**, 60–U75 (2016).
DOI 10.1038/nphoton.2015.247, cit. on p. 38.
- [135] L. Huang, X. Chen, H. Mühlenbernd, G. Li, B. Bai, Q. Tan, G. Jin, T. Zentgraf, and S. Zhang: *Dispersionless Phase Discontinuities for Controlling Light Propagation*. *Nano Letters* **12**, 5750–5755 (2012).
DOI 10.1021/nl303031j, cit. on pp. 40, 45.
- [136] F. Mörz, T. Steinle, A. Steinmann, and H. Giessen: *Multi-Watt femtosecond optical parametric master oscillator power amplifier at 43 MHz*. *Optics Express* **23**, 23960–23967 (2015).
DOI 10.1364/OE.23.023960, cit. on p. 44.

- [137] K. Hirayama, D. W. Wilson, E. N. Glytsis, and T. K. Gaylord: *Rigorous electromagnetic analysis of diffractive cylindrical lenses*. JOSA A **13**, 2219–2231 (1996).
DOI 10.1364/JOSAA.13.002219, cit. on p. 47.
- [138] Y. G. Chen, T. S. Kao, B. Ng, X. Li, X. G. Luo, B. Luk'yanchuk, S. A. Maier, and M. H. Hong: *Hybrid phase-change plasmonic crystals for active tuning of lattice resonances*. Optics Express **21**, 13691–13698 (2013).
DOI 10.1364/OE.21.013691, cit. on pp. 49, 115.
- [139] D. F. Arago: *Mémoire sur une modification remarquable qu'éprouvent les rayons lumineux dans leur passage à travers certains corps diaphanes, et sur quelques autres nouveaux phénomènes d'optique*, Mém Inst, 1811.
Cit. on p. 55.
- [140] J. B. Biot: *Mémoire sur un nouveau genre d'oscillation que les molécules de la lumière éprouvent en traversant certains cristaux*. Mém Inst **1**, 1–372 (1812).
Cit. on p. 55.
- [141] J. B. Biot: *Mémoires sur les rotations que certaines substances impriment aux axes de polarisation des rayons lumineux*. Mém. Acad. Sci **2**, 41–136 (1817).
Cit. on p. 55.
- [142] J. B. Biot: *Mémoire sur la polarisation cirulaire et sur ses application al la chimie organique*. Mém. Acad. Sci **13**, 39–175 (1833).
Cit. on p. 55.
- [143] J. B. Biot: *Memoire sur plusieurs point fondamentaux de mecanique chimique*. Mém Inst **16**, 229–396 (1838).
Cit. on p. 55.
- [144] J. B. Biot: *Méthodes mathématiques et expérimentales pour discerner les mélanges et les combinaisons chimiques*. Mém. Acad. Sci **15**, 93–279 (1838).
Cit. on p. 55.

- [145] A. J. Fresnel: *Mémoire sur la loi des modifications que la réflexion imprime à la lumière polarisée*. Oeuvres **1**, 441–485 (1817).
Cit. on p. 55.
- [146] A. Fresnel: *Memoire sur la double refraction que les rayons lumineux eprouvent en traversant les aiguilles de cristal de roche suivant des directions paralleles a l'axe*. Oeuvres **1**, 731–751 (1822).
Cit. on p. 55.
- [147] B. W. T. Kelvin: *Baltimore lectures on molecular dynamics and the wave theory of light*, CJ Clay and Sons, 1904.
Cit. on pp. 55, 126.
- [148] N. Berova, P. L. Polavarapu, K. Nakanishi, and R. W. Woody: *Comprehensive Chiroptical Spectroscopy, 2 Volume Set*. Comprehensive Chiroptical Spectroscopy, Wiley, 2012. ISBN 9780470641354, cit. on p. 56.
- [149] L. D. Barron: *Molecular Light Scattering and Optical Activity*, 2 edition, Cambridge University Press, 2009. ISBN 052112137X, cit. on pp. 56, 69, 81.
- [150] T. J. Davis and E. Hendry: *Superchiral electromagnetic fields created by surface plasmons in nonchiral metallic nanostructures*. Phys Rev B **87**, 085405 (2013). DOI 10.1103/PhysRevB.87.085405, cit. on pp. 56, 126.
- [151] E. Hendry, T. Carpy, J. Johnston, M. Popland, R. V. Mikhaylovskiy, A. J. Laphorn, S. M. Kelly, L. D. Barron, N. Gadegaard, and M. Kadodwala: *Ultrasensitive detection and characterization of biomolecules using superchiral fields*. Nature Nanotech **5**, 783–787 (2010). DOI doi:10.1038/nnano.2010.209, cit. on pp. 56, 126, 142.
- [152] E. Hendry, R. V. Mikhaylovskiy, L. D. Barron, M. Kadodwala, and T. J. Davis: *Chiral Electromagnetic Fields Generated by Arrays of Nanoslits*. Nano Letters **12**, 3640–3644 (2012). DOI 10.1021/nl3012787, cit. on pp. 56, 126.

- [153] A. Garcia-Etxarri and J. A. Dionne: *Surface-enhanced circular dichroism spectroscopy mediated by nonchiral nanoantennas*. *Phys. Rev. B* **87**, 235409 (2013).
DOI 10.1103/PhysRevB.87.235409, cit. on p. 56.
- [154] M. Schäferling, D. Dregely, M. Hentschel, and H. Giessen: *Tailoring Enhanced Optical Chirality: Design Principles for Chiral Plasmonic Nanostructures*. *Phys. Rev. X* **2**, 031010 (2012).
DOI 10.1103/PhysRevX.2.031010, cit. on pp. 56, 126, 149.
- [155] Y. Tang and A. E. Cohen: *Optical chirality and its interaction with matter*. *Phys Rev Lett* **104**, 163901–163901 (2010).
DOI 10.1103/PhysRevLett.104.163901, cit. on pp. 56, 126, 149.
- [156] Y. Tang and A. E. Cohen: *Enhanced Enantioselectivity in Excitation of Chiral Molecules by Superchiral Light*. *Science* **332**, 333–336 (2011).
DOI 10.1126/science.1202817, cit. on pp. 56, 126.
- [157] Y. Tang, L. Sun, and A. E. Cohen: *Chiroptical hot spots in twisted nanowire plasmonic oscillators*. *Appl Phys Lett* **102**, 043103 (2013).
DOI 10.1063/1.4789529, cit. on p. 56.
- [158] N. A. Abdulrahman, Z. Fan, T. Tonooka, S. M. Kelly, N. Gadegaard, E. Hendry, A. O. Govorov, and M. Kadodwala: *Induced Chirality through Electromagnetic Coupling between Chiral Molecular Layers and Plasmonic Nanostructures*. *Nano Letters* **12**, 977–983 (2012).
DOI 10.1021/nl204055r, cit. on pp. 56, 122, 125, 126.
- [159] V. A. Gerard, Y. K. Gun'ko, E. Defrancq, and A. O. Govorov: *Plasmon-induced CD response of oligonucleotide-conjugated metal nanoparticles*. *Chem Commun* **47**, 7383–7385 (2011).
DOI 10.1039/c1cc11083g, cit. on p. 56.
- [160] A. O. Govorov, Z. Fan, P. Hernandez, J. M. Slocik, and R. R. Naik: *Theory of Circular Dichroism of Nanomaterials Comprising Chiral Molecules and Nanocrystals: Plasmon Enhancement, Dipole Interactions, and Dielectric Effects*. *Nano Letters* **10**, 1374–1382 (2010).
DOI 10.1021/nl100010v, cit. on pp. 56, 126, 127, 148.

- [161] J. M. Slocik, A. O. Govorov, and R. R. Naik: *Plasmonic Circular Dichroism of Peptide-Functionalized Gold Nanoparticles*. *Nano Letters* **11**, 701–705 (2011).
DOI 10.1021/nl1038242, cit. on p. 56.
- [162] B. M. Maoz, Y. Chaikin, A. B. Tesler, O. Bar Elli, Z. Fan, A. O. Govorov, and G. Markovich: *Amplification of Chiroptical Activity of Chiral Biomolecules by Surface Plasmons*. *Nano Letters* **13**, 1203–1209 (2013).
DOI 10.1021/nl304638a, cit. on pp. 56, 126.
- [163] I. Ament, J. Prasad, A. Henkel, S. Schmachtel, and C. Sönnichsen: *Single Unlabeled Protein Detection on Individual Plasmonic Nanoparticles*. *Nano Letters* **12**, 1092–1095 (2012).
DOI 10.1021/nl204496g, cit. on p. 56.
- [164] V. G. Kravets, F. Schedin, R. Jalil, L. Britnell, R. V. Gorbachev, D. Ansell, B. Thackray, K. S. Novoselov, A. K. Geim, A. V. Kabashin, and A. N. Grigorenko: *Singular phase nano-optics in plasmonic metamaterials for label-free single-molecule detection*. *Nat Mater* **12**, 304–309 (2013).
DOI doi:10.1038/nmat3537, cit. on p. 56.
- [165] F. Neubrech, A. Pucci, T. W. Cornelius, S. Karim, A. Garcia-Etxarri, and J. Aizpurua: *Resonant Plasmonic and Vibrational Coupling in a Tailored Nanoantenna for Infrared Detection*. *Phys. Rev. Lett.* **101**, 157403 (2008).
DOI 10.1103/PhysRevLett.101.157403, cit. on p. 56.
- [166] P. Zijlstra, P. M. R. Paulo, and M. Orrit: *Optical detection of single non-absorbing molecules using the surface plasmon resonance of a gold nanorod*. *Nature Nanotech* **7**, 379–382 (2012).
DOI 10.1038/nnano.2012.51, cit. on p. 56.
- [167] A. V. Rogacheva, V. A. Fedotov, A. S. Schwanecke, and N. I. Zheludev: *Giant Gyrotropy due to Electromagnetic-Field Coupling in a Bilayered Chiral Structure*. **97**, 177401–177401 (2006).
DOI 10.1103/PhysRevLett.97.177401, cit. on pp. 57, 110.

- [168] E. Plum, V. A. Fedotov, A. S. Schwanecke, N. I. Zheludev, and Y. Chen: *Giant optical gyrotropy due to electromagnetic coupling*. Applied Physics Letters **90**, 223113–223113 (2007). DOI 10.1063/1.2745203, cit. on pp. 57, 110.
- [169] M. Decker, R. Zhao, C. M. Soukoulis, S. Linden, and M. Wegener: *Twisted split-ring-resonator photonic metamaterial with huge optical activity*. Opt Lett **35**, 1593–1595 (2010). DOI 10.1364/OL.35.001593, cit. on pp. 57, 87.
- [170] C. Helgert, E. Pshenay-Severin, M. Falkner, C. Menzel, C. Rockstuhl, E.-B. Kley, A. Tünnermann, F. Lederer, and T. Pertsch: *Chiral metamaterial composed of three-dimensional plasmonic nanostructures*. Nano Letters **11**, 4400–4404 (2011). DOI 10.1021/nl202565e, cit. on pp. 57, 71, 110.
- [171] C. Menzel, C. Helgert, C. Rockstuhl, E. B. Kley, A. Tünnermann, T. Pertsch, and F. Lederer: *Asymmetric Transmission of Linearly Polarized Light at Optical Metamaterials*. Phys Rev Lett **104**, 253902 (2010). DOI 10.1103/PhysRevLett.104.253902, cit. on p. 57.
- [172] C. Rockstuhl, C. Menzel, T. Paul, and F. Lederer: *Optical activity in chiral media composed of three-dimensional metallic meta-atoms*. Phys. Rev. B **79**, 035321 (2009). DOI 10.1103/PhysRevB.79.035321, cit. on p. 57.
- [173] Y. Zhao, M. A. Belkin, and A. Alù: *Twisted optical metamaterials for planarized ultrathin broadband circular polarizers*. Nature Communications **3**, 870–877 (2012). DOI 10.1038/ncomms1877, cit. on pp. 57, 84.
- [174] S. Zhang, Y.-S. Park, J. Li, X. Lu, W. Zhang, and X. Zhang: *Negative refractive index in chiral metamaterials*. **102**, 023901–023901 (2009). DOI 10.1103/PhysRevLett.102.023901, cit. on pp. 57, 110.
- [175] J. Pendry: *A chiral route to negative refraction*. Science **306**, 1353–1355 (2004). DOI 10.1126/science.1104467, cit. on p. 57.

- [176] J. Zhou, J. Dong, B. Wang, T. Koschny, M. Kafesaki, and C. M. Soukoulis: *Metamaterial with negative index due to chirality*. *Phys Rev B* **79** (2009).
DOI 10.1103/PhysRevB.79.121104, cit. on p. 57.
- [177] A. Christofi, N. Stefanou, G. Gantzounis, and N. Papanikolaou: *Giant Optical Activity of Helical Architectures of Plasmonic Nanorods*. *Journal Of Physical Chemistry C*, 120710155231005 (2012).
DOI 10.1021/jp304907s, cit. on p. 57.
- [178] A. Kuzyk, R. Schreiber, Z. Fan, G. Pardatscher, E.-M. Roller, A. Hoegele, F. C. Simmel, A. O. Govorov, and T. Liedl: *DNA-based self-assembly of chiral plasmonic nanostructures with tailored optical response*. *Nature* **483**, 311–314 (2012).
DOI 10.1038/nature10889, cit. on p. 57, 110.
- [179] A. J. Mastroianni, S. A. Claridge, and A. P. Alivisatos: *Pyramidal and Chiral Groupings of Gold Nanocrystals Assembled Using DNA Scaffolds*. *J Am Chem Soc* **131**, 8455–8459 (2009).
DOI 10.1021/ja808570g, cit. on p. 57.
- [180] X. Shen, C. Song, J. Wang, D. Shi, Z. Wang, N. Liu, and B. Ding: *Rolling up gold nanoparticle-dressed DNA origami into three-dimensional plasmonic chiral nanostructures*. *J Am Chem Soc* **134**, 146–149 (2012).
DOI 10.1021/ja209861x, cit. on p. 57.
- [181] X. Shen, A. Asenjo-Garcia, Q. Liu, Q. Jiang, F. J. Garcia de Abajo, N. Liu, and B. Ding: *Three-Dimensional Plasmonic Chiral Tetramers Assembled by DNA Origami*. *Nano Letters* **13**, 2128–2133 (2013).
DOI 10.1021/nl400538y, cit. on p. 57.
- [182] D. Patterson, M. Schnell, and J. M. Doyle: *Enantiomer-specific detection of chiral molecules via microwave spectroscopy*. *Nature* **497**, 475–477 (2013).
Cit. on p. 59.

- [183] H. Rhee, Y.-G. June, J.-S. Lee, K.-K. Lee, J.-H. Ha, Z. H. Kim, S.-J. Jeon, and M. Cho: *Femtosecond characterization of vibrational optical activity of chiral molecules*. *Nature* **458**, 310–313 (2009).
Cit. on p. 59.
- [184] M. H. M. Janssen and I. Powis: *Detecting chirality in molecules by imaging photoelectron circular dichroism*. *Physical Chemistry Chemical Physics* **16**, 856–871 (2014).
Cit. on p. 59.
- [185] G. D. Fasman: *Circular Dichroism and the Conformational Analysis of Biomolecules*, Softcover reprint of hardcover 1st ed. 1996 edition, Springer, 2010.
ISBN 1441932496, cit. on pp. 59, 65, 90, 126, 127.
- [186] L. A. Nafie: *Vibrational Optical Activity: Principles and Applications*, 1 edition, Wiley, 2011.
Cit. on p. 59.
- [187] I. Tinoco Jr, W. Mickols, and M. F. Maestre: *Absorption, scattering, and imaging of biomolecular structures with polarized light*. *Annual review of Physics* **16**, 319–349 (1987).
Cit. on p. 59.
- [188] H. Dekkers: *Circularly polarized luminescence: a probe for chirality in the excited state*. In: *Circular Dichroism: Principles and Applications*, ed. by K. Nakanishi, N. Berova, and R. W. Woody, ChemInform (New York), 1994.
Cit. on p. 59.
- [189] G. Berden, R. Peeters, and G. Meijer: *Cavity ring-down spectroscopy: Experimental schemes and applications*. *International Reviews in Physical Chemistry* **19**, 565–607 (2010).
Cit. on p. 59.
- [190] A. Moscovitz: *Theoretical Aspects of Optical Activity Part One: Small Molecules*. *Advances in Chemical Physics*, John Wiley & Sons, Inc., 1962.
Cit. on p. 60.

- [191] D. A. B. Miller: *Quantum Mechanics for Scientists and Engineers*, 1 edition, Cambridge University Press, 2008.
Cit. on p. 65.
- [192] L. Rosenfeld: *Quantum-mechanical theory of the natural optical activity of liquids and gases*. *Zeitschrift für Physik*, 1928.
Cit. on p. 65.
- [193] H. Eyring, J. Walter, and G. E. Kimball: *Quantum chemistry*, 1964.
Cit. on p. 65.
- [194] V. M. Shalaev: *Optical negative-index metamaterials*. *Nature Publishing Group* **1**, 41–48 (2007).
Cit. on p. 66.
- [195] C. M. Soukoulis, S. Linden, and M. Wegener: *Negative Refractive Index at Optical Wavelengths*. *Science* **315**, 47–49 (2007).
Cit. on p. 66.
- [196] I. V. Lindell, A. H. Sihvola, S. A. Tretyakov, and A. J. Viitanen: *Electromagnetic waves in chiral and bi-isotropic media*, Artech House, 1994.
Cit. on pp. 67, 122, 123.
- [197] M. Schäferling: *Chiral plasmonic near-field sources : control of chiral electromagnetic fields for chiroptical spectroscopies*, PhD Thesis, 2016.
ISBN 455754896, cit. on p. 68.
- [198] N. Engheta and D. L. Jaggard: *Electromagnetic chirality and its applications*. *IEEE Antennas and Propagation Society Newsletter* **30**, 6–12 (1988).
DOI 10.1109/MAP.1988.6086107, cit. on p. 68.
- [199] E. Condon, W. Altar, and H. Eyring: *One-electron rotatory power*. *Journal Of Chemical Physics* **5**, 753–775 (1937).
Cit. on p. 69.
- [200] M. Born: *Über die natürliche optische Aktivität von Flüssigkeiten und Gasen*. *Physikalische Zeitschrift* **16**, 251–258 (1915).
Cit. on pp. 69, 80.

- [201] C. W. Oseen: *The alternating effect between two electrical dipoles and the rotation of the polarisation layer in crystals and liquids*. *Annalen der Physik* **48**, 1–56 (1915).
Cit. on p. 69.
- [202] W. Kuhn: *The physical significance of optical rotatory power*. *Transactions of the Faraday Society* **26**, 0293–0307 (1930).
Cit. on p. 69.
- [203] J. Kirkwood: *On the Theory of Optical Rotatory Power | Browse - Journal of Chemical Physics*. *The Journal of chemical physics* (1937).
Cit. on p. 69.
- [204] P. Drude: *Lehrbuch der Optik*, Hirzel, 1900.
Cit. on p. 71.
- [205] M. Born: *Elektronentheorie des natürlichen optischen Drehungsvermögens isotroper und anisotroper Flüssigkeiten*. *Annalen der Physik* **360**, 177–240 (1918).
DOI 10.1002/andp.19183600302, cit. on p. 71.
- [206] W. Kuhn: *Über die Drudesche Theorie der optischen Aktivität*. *Z. physikal. Chem. B* **20**, 325–332 (1933).
Cit. on p. 71.
- [207] D. L. Jaggard, A. R. Mickelson, and C. H. Papas: *On electromagnetic waves in chiral media*. *Applied Physics Letters* **18**, 211–216 (1979).
DOI 10.1007/BF00934418, cit. on p. 71.
- [208] S. A. Tretyakov, F. Mariotte, C. R. Simovski, T. G. Kharina, and J. P. Heliot: *Analytical antenna model for chiral scatterers: Comparison with numerical and experimental data*. *Antennas and Propagation, IEEE Transactions on* **44**, 1006–1014 (1996).
Cit. on p. 71.
- [209] C. Rockstuhl, C. Menzel, T. Paul, and F. Lederer: *Optical activity in chiral media composed of three-dimensional metallic meta-atoms*. *Physical Review B* **79**, 035321 (2009).
DOI 10.1103/PhysRevB.79.035321, cit. on p. 71.

- [210] J. G. Gibbs, A. G. Mark, S. Eslami, and P. Fischer: *Plasmonic nanohelix metamaterials with tailorable giant circular dichroism*. *Applied Physics Letters* **103**, 213101-1–213101-4 (2013).
DOI 10.1063/1.4829740, cit. on p. 71.
- [211] G. Kenanakis, A. Xomalis, A. Selimis, M. Vamvakaki, M. Farsari, M. Kafesaki, C. M. Soukoulis, and E. N. Economou: *Three-Dimensional Infrared Metamaterial with Asymmetric Transmission*. *ACS Photonics* **2**, 287–294 (2015).
DOI 10.1021/ph5003818, cit. on p. 72.
- [212] W. Kuhn: *Quantitative Verhältnisse und Beziehungen bei der natürlichen optischen Aktivität*. *Zeitschrift für physikalische Chemie B* **4**, 14–36 (1929).
Cit. on p. 80.
- [213] Y. P. Svirko and N. I. Zheludev: *Polarization of Light in Nonlinear Optics*, John Wiley & Sons, 1998.
ISBN 9780471976400, cit. on p. 81.
- [214] A. Sihvola and I. V. Lindell: *Bi-Isotropic Constitutive Relations*. *Microwave and Optical Technology Letters* **4**, 295–297 (1991).
DOI 10.1002/mop.4650040805, cit. on p. 82.
- [215] L. D. Landau and E. M. Lifshitz: *Electrodynamics of Continuous Media*, Pergamon, 1984.
Cit. on p. 82.
- [216] A. Yariv and P. Yeh: *Optical Waves in Crystals: Propagation and Control of Laser Radiation*. *Wiley Series in Pure and Applied Optics*, Wiley, 2002.
ISBN 9780471430810, cit. on p. 82.
- [217] P. Wang, J. Yang, J. Liu, L. Zhang, and Q. Yang: *Chiral mesoporous organosilicas with R-(+)-Binol integrated in the framework*. *Microporous and Mesoporous Materials* **117**, 91–97 (2009).
Cit. on p. 83.

- [218] A. Guerrero-Martínez, J. L. Alonso-Gómez, B. Auguié, M. M. Cid, and L. M. Liz-Marzén: *From individual to collective chirality in metal nanoparticles*. *Nano Today* **6**, 381–400 (2011).
DOI 10.1016/j.nantod.2011.06.003, cit. on p. 84.
- [219] A. Guerrero-Martínez A.nez, B. Auguié B., J. L. L. Alonso-Gómez J. L.mez, Z. Dzolic Z.olic, S. Gómez-Graña Gómez-Graña, M. Zinic M., M. M. Cid, and L. M. Liz-Marzán: *Intense Optical Activity from Three-Dimensional Chiral Ordering of Plasmonic Nanoantennas*. *Angew Chem Int Edit* **50**, 5499–5503 (2011).
DOI 10.1002/anie.201007536, cit. on pp. 84, 110.
- [220] S. Zhang, J. Zhou, Y.-S. Park, J. Rho, R. Singh, S. Nam, A. K. Azad, H.-T. Chen, **X. Yin**, A. J. Taylor, and X. Zhang: *Photoinduced handedness switching in terahertz chiral metamolecules*. *Nature Communications* **3**, 942–942 (2012).
DOI 10.1038/ncomms1908, cit. on pp. 84, 110.
- [221] M. Hentschel, M. Schäferling, B. Metzger, and H. Giessen: *Plasmonic Diastereomers: Adding up Chiral Centers*. *Nano Letters* **13**, 600–606 (2013).
DOI 10.1021/nl3041355, cit. on pp. 84, 116.
- [222] M. Hentschel, L. Wu, M. Schäferling, P. Bai, E. P. Li, and H. Giessen: *Optical Properties of Chiral Three-Dimensional Plasmonic Oligomers at the Onset of Charge-Transfer Plasmons*. *ACS nano* **6**, 10355–10365 (2012).
DOI 10.1021/nn304283y, cit. on p. 84.
- [223] B. Frank, **X. Yin**, M. Schäferling, J. Zhao, S. M. Hein, P. V. Braun, and H. Giessen: *Large-Area 3D Chiral Plasmonic Structures*. *ACS nano* **7**, 6321–6329 (2013).
DOI 10.1021/nn402370x, cit. on pp. 84, 110.
- [224] N. J. Halas, S. Lal, W.-S. Chang, S. Link, and P. Nordlander: *Plasmons in Strongly Coupled Metallic Nanostructures*. *Chem. Rev.* **111**, 3913–3961 (2011).
DOI 10.1021/cr200061k, cit. on p. 85.

- [225] B. Auguie B., J. Lorenzo Alonso-Gomez, A. Guerrero-Martinez, and L. M. Liz-Marzàn: *Fingers Crossed: Optical Activity of a Chiral Dimer of Plasmonic Nanorods*. *J Phys Chem Lett* **2**, 846–851 (2011). DOI 10.1021/jz200279x, cit. on pp. 86, 111.
- [226] M. Hentschel, M. Schäferling, T. Weiss, N. Liu, and H. Giessen: *Three-Dimensional Chiral Plasmonic Oligomers*. *Nano Letters* **12**, 2542–2547 (2012). DOI 10.1021/nl300769x, cit. on pp. 87, 93, 110.
- [227] N. Liu, H. Guo, L. Fu, S. Kaiser, H. Schweizer, and H. Giessen: *Three-dimensional photonic metamaterials at optical frequencies*. *Nature* **7**, 31–37 (2007). Cit. on pp. 87, 111.
- [228] R. Taubert, R. Ameling, T. Weiss, A. Christ, and H. Giessen: *From near-field to far-field coupling in the third dimension: retarded interaction of particle plasmons*. *Nano Letters* **11**, 4421–4424 (2011). Cit. on p. 90.
- [229] Y. Svirko, N. Zheludev, and M. Osipov: *Layered chiral metallic microstructures with inductive coupling*. *Applied Physics Letters* **78**, 498–498 (2001). DOI 10.1063/1.1342210, cit. on pp. 93, 111.
- [230] N. Liu, M. Hentschel, T. Weiss, P. Alivisatos, and H. Giessen: *Three-dimensional plasmon rulers*. *Science* **332**, 1407–1410 (2011). DOI 10.1126/science.1199958, cit. on p. 93.
- [231] H. Fredriksson, Y. Alaverdyan, A. Dmitriev, C. Langhammer, D. S. Sutherland, M. Zsch, and B. Kasemo: *Hole-Mask Colloidal Lithography*. *Advanced Materials* **19**, 4297–4302 (2007). DOI 10.1002/adma.200700680, cit. on p. 95.
- [232] S. Cataldo, J. Zhao, F. Neubrech, B. Frank, C. Zhang, P. V. Braun, and H. Giessen: *Hole-Mask Colloidal Nanolithography for Large-Area Low-Cost Metamaterials and Antenna-Assisted Surface-Enhanced Infrared Absorption Substrates*. *ACS nano* **6**, 979–985 (2012). DOI 10.1021/nn2047982, cit. on p. 95.

- [233] J. Zhao, C. Zhang, P. V. Braun, and H. Giessen: *Large-Area Low-Cost Plasmonic Nanostructures in the NIR for Fano Resonant Sensing*. *Advanced Materials* **24**, OP247–OP252 (2012).
DOI 10.1002/adma.201202109, cit. on p. 95.
- [234] M. C. Gwinner, E. Koroknay, L. Fu, P. Patoka, W. Kandulski, M. Giersig, and H. Giessen: *Periodic Large-Area Metallic Split-Ring Resonator Metamaterial Fabrication Based on Shadow Nanosphere Lithography*. *Small* **5**, 400–406 (2009).
DOI 10.1002/smll.200800923, cit. on pp. 95, 97.
- [235] A. Kosiorek, W. Kandulski, H. Glaczynska, and M. Giersig: *Fabrication of Nanoscale Rings, Dots, and Rods by Combining Shadow Nanosphere Lithography and Annealed Polystyrene Nanosphere Masks*. *Small* **1**, 439–444 (2005).
DOI 10.1002/smll.200400099, cit. on p. 95.
- [236] J. Zhao, B. Frank, S. Burger, and H. Giessen: *Large-Area High-Quality Plasmonic Oligomers Fabricated by Angle-Controlled Colloidal Nanolithography*. *ACS nano* **5**, 9009–9016 (2011).
DOI 10.1021/nn203177s, cit. on p. 95.
- [237] A Kosiorek, W Kandulski, P Chudzinski, K Kempa, and M Giersig: *Shadow Nanosphere Lithography: Simulation and Experiment*. *Nano Letters* **4**, 1359–1363 (2004).
DOI 10.1021/nl049361t, cit. on p. 95.
- [238] R. Kuroda, T. Harada, and Y. Shindo: *A solid-state dedicated circular dichroism spectrophotometer: Development and application*. *Review of Scientific Instruments* **72**, 3802–3810 (2001).
DOI 10.1063/1.1400157, cit. on p. 100.
- [239] M. Kuwata-Gonokami, N. Saito, Y. Ino, M. Kauranen, K. Jefimovs, T. Vallius, J. Turunen, and Y. Svirko: *Giant optical activity in quasi-two-dimensional planar nanostructures*. **95**, 227401–227401 (2005).
DOI 10.1103/PhysRevLett.95.227401, cit. on p. 110.

- [240] A. Papakostas, A. Potts, D. Bagnall, S. Prosvirnin, H. Coles, and N. Zheludev: *Optical Manifestations of Planar Chirality*. **90**, 107404–107404 (2003).
DOI 10.1103/physrevlett.90.107404, cit. on p. 110.
- [241] M. Decker, M. Ruther, C. E. Kriegler, J. Zhou, C. M. Soukoulis, S. Linden, and M. Wegener: *Strong optical activity from twisted-cross photonic metamaterials*. *Optics Letters* **34**, 2501–2503 (2009).
DOI 10.1364/OL.34.002501, cit. on p. 110.
- [242] M. Decker, M. W. Klein, M. Wegener, and S. Linden: *Circular dichroism of planar chiral magnetic metamaterials*. *Optics Letters* **32**, 856–858 (2007).
DOI 10.1364/OL.32.000856, cit. on p. 110.
- [243] H.-T. Chen, W. J. Padilla, J. M. O. Zide, A. C. Gossard, A. J. Taylor, and R. D. Averitt: *Active terahertz metamaterial devices*. *Nature* **444**, 597–600 (2006).
DOI 10.1038/nature05343, cit. on p. 110.
- [244] D. J. Aschaffenburg, M. R. C. Williams, D. Talbayev, D. F. Santavicca, D. E. Prober, and C. A. Schmuttenmaer: *Efficient measurement of broadband terahertz optical activity*. *Applied Physics Letters* **100**, 241114–241114 (2012).
DOI 10.1063/1.4729148, cit. on p. 110.
- [245] R. Zhao, T. Koschny, and C. M. Soukoulis: *Chiral metamaterials: retrieval of the effective parameters with and without substrate*. *Optics Express* **18**, 14553–14567 (2010).
DOI 10.1364/OE.18.014553, cit. on p. 110.
- [246] N. Kanda, K. Konishi, and M. Kuwata-Gonokami: *Light-induced terahertz optical activity*. *Optics Letters* **34**, 3000–3002 (2009).
DOI 10.1364/OL.34.003000, cit. on p. 110.
- [247] A. Kuzyk, R. Schreiber, H. Zhang, A. O. Govorov, T. Liedl, and N. Liu: *Reconfigurable 3D plasmonic metamolecules*. *Nature Materials* **13**, 862–866 (2014).
DOI 10.1038/nmat4031, cit. on p. 110.

- [248] R. Schreiber, N. Luong, Z. Fan, A. Kuzyk, P. C. Nickels, T. Zhang, D. M. Smith, B. Yurke, W. Kuang, A. O. Govorov, and T. Liedl: *Chiral plasmonic DNA nanostructures with switchable circular dichroism*. *Nature Communications* **4** (2013).
DOI 10.1038/ncomms3948, cit. on p. 110.
- [249] T. T. Lv, Z. Zhu, J. H. Shi, C. Y. Guan, Z. P. Wang, and T. J. Cui: *Optically controlled background-free terahertz switching in chiral metamaterial*. **39**, 3066–3069 (2014).
DOI 10.1364/OL.39.003066, cit. on p. 110.
- [250] G. Kenanakis, R. Zhao, N. Katsarakis, M. Kafesaki, C. M. Soukoulis, and E. N. Economou: *Optically controllable THz chiral metamaterials*. *Optical Society of America* **22** (2014).
DOI 10.1364/OE.22.012149, cit. on p. 110.
- [251] N. Kanda, K. Konishi, and M. Kuwata-Gonokami: *All-photoinduced terahertz optical activity*. *Optics Letters* **39**, 3274–3277 (2014).
DOI 10.1364/OL.39.003274, cit. on p. 110.
- [252] R. Stanley: *Plasmonics in the mid-infrared*. *Nature Photonics* **6**, 409–411 (2012).
DOI 10.1038/nphoton.2012.161, cit. on p. 110.
- [253] J. N. Anker, W. P. Hall, O. Lyandres, N. C. Shah, J. Zhao, and R. P. Van Duyne: *Biosensing with plasmonic nanosensors*. *Nature Materials* **7**, 442–453 (2008).
DOI 10.1038/nmat2162, cit. on p. 110.
- [254] T. Cao, L. Zhang, R. E. Simpson, C. Wei, and M. J. Cryan: *Strongly tunable circular dichroism in gammadion chiral phase-change metamaterials*. *Optics Express* **21**, 27841–27851 (2013).
DOI 10.1364/OE.21.027841, cit. on p. 110.
- [255] D. Nau, A. Schönhardt, C. Bauer, A. Christ, T. Zentgraf, J. Kuhl, M. Klein, and H. Giessen: *Correlation Effects in Disordered Metallic Photonic Crystal Slabs*. **98**, 133902 (2007).
DOI 10.1103/PhysRevLett.98.133902, cit. on p. 112.

- [256] E. H. Korte: *Discrimination of Enantiomers at Microgram Level Using Liquid-Crystalline Solutions*. Applied Spectroscopy **32**, 568–572 (1978).
Cit. on p. 114.
- [257] T. Cao, C. Wei, R. E. Simpson, L. Zhang, and M. J. Cryan. Fast tuning of double Fano resonance using a phase-change metamaterial under low power intensity. **4**, 4463–4463 (2013).
DOI 10.1038/srep04463, cit. on p. 114.
- [258] R. Wang, J. Wei, and Y. Fan: *Chalcogenide phase-change thin films used as grayscale photolithography materials*. Optics Express **22**, 4973–4984 (2014).
DOI 10.1364/OE.22.004973, cit. on p. 115.
- [259] Q. Wang, J. Maddock, E. T. F. Rogers, T. Roy, C. Craig, K. F. MacDonald, D. W. Hewak, and N. I. Zheludev: *1.7 Gbit/in.² gray-scale continuous-phase-change femtosecond image storage*. Applied Physics Letters **104**, 121105–121105 (2014).
DOI 10.1063/1.4869575, cit. on p. 115.
- [260] J. Hegedüs and S. R. Elliott: *Microscopic origin of the fast crystallization ability of Ge-Sb-Te phase-change memory materials*. Nature Materials **7**, 399–405 (2008).
DOI 10.1038/nmat2157, cit. on p. 115.
- [261] D. Loke, T. H. Lee, W. J. Wang, Shi, L. P., R. Zhao, Y. C. Yeo, T. C. Chong, and S. R. Elliott: *Breaking the Speed Limits of Phase-Change Memory*. Science **336**, 1566–1569 (2012).
DOI 10.1126/science.1221561, cit. on p. 118.
- [262] R. Brendel and D. Bormann: *An infrared dielectric function model for amorphous solids*. **71**, 1–6 (1992).
DOI 10.1063/1.350737, cit. on p. 125.
- [263] A. O. Govorov and Z. Fan: *Theory of Chiral Plasmonic Nanostructures Comprising Metal Nanocrystals and Chiral Molecular Media*. ChemPhysChem **13**, 2551–2560 (2012).
DOI 10.1002/cphc.201100958, cit. on pp. 125, 127.

- [264] P. L. Stiles, J. A. Dieringer, N. C. Shah, and R. R. Van Duyne: *Surface-Enhanced Raman Spectroscopy*. *Annual Review of Analytical Chemistry* **1**, 601–626 (2008).
DOI 10.1146/annurev.anchem.1.031207.112814, cit. on p. 126.
- [265] F. Neubrech, A. Pucci, T. W. Cornelius, S. Karim, A. Garcia-Etxarri, and J. Aizpurua: *Resonant Plasmonic and Vibrational Coupling in a Tailored Nanoantenna for Infrared Detection*. **101**, 157403 (2008).
DOI 10.1103/PhysRevLett.101.157403, cit. on p. 126.
- [266] M. Li, S. K. Cushing, and N. Wu: *Plasmon-enhanced optical sensors: a review*. *Analyst* **140**, 386–406 (2014).
DOI 10.1039/C4AN01079E, cit. on p. 126.
- [267] L. A. Nguyen, H. He, and C. Pham-Huy: *Chiral drugs: an overview*. *International Journal of Biomedical Science : IJBS* **2**, 85–100 (2006).
Cit. on p. 126.
- [268] R. Tullius, A. S. Karimullah, M. Rodier, B. Fitzpatrick, N. Gadegaard, L. D. Barron, V. M. Rotello, G. Cooke, A. Laphorn, and M. Kadodwala: *“Superchiral” Spectroscopy: Detection of Protein Higher Order Hierarchical Structure with Chiral Plasmonic Nanostructures*. *Journal of the American Chemical Society* **137**, 8380–8383 (2015).
DOI 10.1021/jacs.5b04806, cit. on p. 126.
- [269] T. J. Davis and D. E. Gomez: *Interaction of localized surface plasmons with chiral molecules*. *Physical Review B* **90** (2014).
DOI 10.1103/PhysRevB.90.235424, cit. on p. 126.
- [270] A. Garcia-Etxarri and J. A. Dionne: *Surface-enhanced circular dichroism spectroscopy mediated by nonchiral nanoantennas*. *Physical Review B* **87**, 235409 (2013).
DOI 10.1103/PhysRevB.87.235409, cit. on pp. 126, 127.
- [271] N. Meinzer, E. Hendry, and W. L. Barnes: *Probing the chiral nature of electromagnetic fields surrounding plasmonic nanostructures*. *Physical Review B* **88** (2013).
DOI 10.1103/PhysRevB.88.041407, cit. on p. 126.

- [272] R.-Y. Wang, P. Wang, Y. Liu, W. Zhao, D. Zhai, X. Hong, Y. Ji, X. Wu, F. Wang, D. Zhang, W. Zhang, R. Liu, and X. Zhang: *Experimental Observation of Giant Chiroptical Amplification of Small Chiral Molecules by Gold Nanosphere Clusters*. *Journal Of Physical Chemistry C* **118**, 9690–9695 (2014). DOI 10.1021/jp5025813, cit. on p. 126.
- [273] B. M. Maoz, R. van der Weegen, Z. Fan, A. O. Govorov, G. Ellestad, N. Berova, E. W. Meijer, and G. Markovich: *Plasmonic Chiroptical Response of Silver Nanoparticles Interacting with Chiral Supramolecular Assemblies*. *Journal of the American Chemical Society* **134**, 17807–17813 (2012). DOI 10.1021/ja309016k, cit. on p. 126.
- [274] A. O. Govorov, Y. K. Gun'ko, J. M. Slocik, V. A. Gerard, Z. Fan, and R. R. Naik: *Chiral nanoparticle assemblies: circular dichroism, plasmonic interactions, and exciton effects*. *J Mater Chem* **21**, 16806–16818 (2011). DOI 10.1039/c1jm12345a, cit. on p. 126.
- [275] F. Lu, Y. Tian, M. Liu, D. Su, H. Zhang, A. O. Govorov, and O. Gang: *Discrete Nanocubes as Plasmonic Reporters of Molecular Chirality*. *Nano Letters* **13**, 3145–3151 (2013). DOI 10.1021/nl401107g, cit. on p. 126.
- [276] A. O. Govorov: *Plasmon-Induced Circular Dichroism of a Chiral Molecule in the Vicinity of Metal Nanocrystals. Application to Various Geometries*. *Journal Of Physical Chemistry C* **115**, 7914–7923 (2011). DOI 10.1021/jp1121432, cit. on pp. 126, 127, 131.
- [277] Y. Zhao, L. Xu, W. Ma, L. Wang, H. Kuang, C. Xu, and N. A. Kotov: *Shell-Engineered Chiroplasmonic Assemblies of Nanoparticles for Zeptomolar DNA Detection*. *Nano Letters*, 140523101115003 (2014). DOI 10.1021/nl501166m, cit. on p. 126.
- [278] W. Ma, H. Kuang, L. Xu, L. Ding, C. Xu, L. Wang, and N. A. Kotov: *Attomolar DNA detection with chiral nanorod assemblies*. *Nature Communications* **4** (2013). DOI 10.1038/ncomms3689, cit. on p. 126.

- [279] Z. Xu, L. Xu, L. M. Liz Marzàn, W. Ma, N. A. Kotov, L. Wang, H. Kuang, and C. Xu: *Chiral Sensors: Sensitive Detection of Silver Ions Based on Chiroplasmonic Assemblies of Nanoparticles*. *Advanced Optical Materials* **1**, 603–603 (2013). DOI 10.1002/adom.201370053, cit. on p. 126.
- [280] T. Wu, J. Ren, R. Wang, and X. Zhang: *Competition of Chiroptical Effect Caused by Nanostructure and Chiral Molecules*. *Journal Of Physical Chemistry C* **118**, 20529–20537 (2014). DOI 10.1021/jp505290v, cit. on p. 127.
- [281] M. Onishi, K. Crabtree, and R. A. Chipman: *Formulation of rigorous coupled-wave theory for gratings in bianisotropic media*. *JOSA A* **28**, 1747–1758 (2011). DOI 10.1364/JOSAA.28.001747, cit. on p. 127.
- [282] V. V. Klimov, I. V. Zabkov, A. A. Pavlov, and D. V. Guzotov: *Eigen oscillations of a chiral sphere and their influence on radiation of chiral molecules*. *Optics Express* **22**, 18564–18578 (2014). DOI 10.1364/OE.22.018564, cit. on p. 127.
- [283] D. Dregely, F. Neubrech, H. Duan, R. Vogelgesang, and H. Giessen: *Vibrational near-field mapping of planar and buried three-dimensional plasmonic nanostructures*. *Nature Communications* **4** (2013). DOI 10.1038/ncomms3237, cit. on p. 132.
- [284] E. C. Le Ru and P. G. Etchegoin: *Quantifying SERS enhancements*. *MRS Bulletin* **38**, 631–640 (2013). DOI 10.1557/mrs.2013.158, cit. on p. 136.
- [285] G. E. Desobry and P. K. Kabir: *Optical-Rotatory Power in a Classical One-Electron Model*. *American Journal Of Physics* **41**, 1350–1357 (1973). Cit. on p. 142.

ACKNOWLEDGMENTS

Many people have directly or indirectly impacted this thesis and led to its realization. I wish to thank them here for their support and contributions.

Firstly, I'd like to thank *Prof. Dr. Harald Giessen* for engaging me in a vivid hourlong conversation at SPP6 in Korea at the end of which he offered me the great opportunity to carry out my PhD studies in his group. He captured my intellectual curiosity by asking a series of very engaging questions relating to the role light could play in uncovering structural (a-)symmetries. Subsequently, he managed to continuously fuel this curiosity and turn it into finished research projects through his relentlessly enthusiastic and demanding supervision style.

Furthermore, I'd like to thank *Prof. Dr. Thomas Zentgraf* for a very fruitful and pleasant collaboration on tunable metasurfaces and for agreeing to be on my examination committee.

Also, I'd like to thank *Prof. Dr. Günter Wunner* for chairing the examination committee.

Experimental physics is a highly collaborative undertaking and I have enjoyed working with many wonderful collaborators both from PI4 and other institutions.

In particular, I'd like to thank the "chiral guys" - Martin Schäferling, Bettina Frank, Mario Hentschel, Ioanna Sakellari, Na Liu, Thomas Weiss and Maxim Nesterov - for great discussions, collaborations and shared frustration about widely spread misconceptions in the young field of enhanced chiroptical spectroscopies.

Furthermore, I'd like to thank Prof. Dr. Matthias Wuttig and Prof. Dr. Thomas Taubner for introducing me to phase change materials from which a whole host of interesting projects resulted. In this context, I

also want to thank Ann-Katrin Michel, Lingling Huang and the "laser guys" (Tobias Steinle, Florian Mörz, Stefan Kedenburg) for their help with the active plasmonics research.

There are many other scientists who I have enjoyed discussing with during my PhD: Nikolai Strohfeldt, Andreas Tittel, Florian Sterl, Frank Neubrech, Bernd Metzger, Dominik Floess, Ksenia Weber, Moritz Floess, Shahin Bagheri, Rostyslav Semenyshyn, Sven Hein, Monika Ubl, Prof. Nader Engheta, Prof. Tim Davis, Daniel Gomez, Klaus Jöns and my office mates Christina Bauer, Joachim Krauth and Ioanna Sakellari.

As most of my projects involved some sort of nanofabrication, I greatly benefitted from being affiliated with the Max-Planck-Institute for Solid State Research. In particular, I'd like to thank Jürgen Weis for making cleanroom access possible, and Thomas Reindl and Ulrike Waizmann for technical assistance. Also, I had the chance to engage in interesting discussions and collaborations with scientists there: Klas Lindfors, Stefan Kaiser, Sahand Eslami, Eren Suyolcu, Nathan Chejanovsky and Pascal Wittlich.

I was lucky that I got to attend numerous international conferences and meet great people from all over the world that include amongst others Balthasar Müller, Jonathan Fan, Stephan Kress, Charles Al-tuzarra, Frerik van Beijnum, Philip Chimento and Benjamin Gallinet.

I would also like to thank the people I have known way before I started my PhD and who have inspired me to do research and given me great advice early on: Norbert Huelsbusch, Peter Minnema, Prof. Carl M. Bender, Prof. Gero von Plessen, Benoit Vicedo and Prof. Peter Loosen.

Throughout my PhD years, I lived in bustling multicultural flat shares that were the backdrop to all my scientific pursuits. I thank my numerous flat mates for making my time in Stuttgart special: Ludovic Mezzana, Grigoriy Khazaridi, Darío Blanco Iturriaga, Romain Cordaro, Margarida Gama, Ksenia Lebedeva, Kurt Goerendt and Clemens Buss.

Then there are of course countless friends who have been there with me all these years, many of them pursuing very similar life paths up to this point, with whom I shared and debated our respective experiences. Among them Daojing Guo, Ruth Hoffmann, Kanali Togawa, Marc-André Schulz and Johannes Jung stand out in particular.

Lastly, I'd like to thank my parents and my sister Laiyin for their continued support throughout my life. I am greatly indebted to my parents for taking a big leap when they were my age and thus providing me with many opportunities that I wouldn't have had otherwise.

COLOPHON

This document was typeset using the typographical look-and-feel `classicthesis` developed by André Miede. The style was inspired by Robert Bringhurst’s seminal book on typography “*The Elements of Typographic Style*”. `classicthesis` is available for both \LaTeX and \LyX :

<https://bitbucket.org/amiede/classicthesis/>

Final Version as of September 6, 2017 (`classicthesis o`).